# *Radio Occultation Science Plan*

## *EUMETSAT Polar System (EPS-SG) / Meteorological Operational Second Generation (MetOp-SG)*

## *prepared by the Radio Occultation Science Advisory Group and external experts*

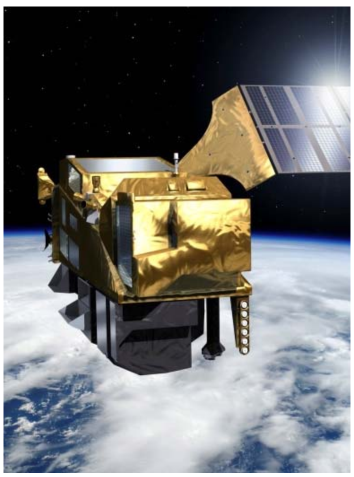

GNSS Radio Occultation
mission on MetOp-SG Satellite A

GNSS Radio Occultation
mission on MetOp-SG Satellite B


Issue : v2C

Date : 28 November 2018

# *Document Change Record*

| *Issue / Revision* | *Date* | *DCN. No* | *Changed Pages / Paragraphs* |
|---|---|---|---|
| 1 | | | Initial version |
| 1B | 21 December 2016 | | All contributor input provided, version for G. Kirchengast Review. |
| 1C | 11 January 2017 | | Added further ionosphere information (section 8.1) and executive summary. |
| 1D | 02 February 2017 | | Section 5.1, 7, 8.4, 8.5 updates |
| 1E | 14 March 2017 | | Section 4.3, 8.2.2 and 8.2.3, added 4.4, complete re-write of 10 |
| 1F | 19 May 2017 | | Reviewed v1E document (by G. Kirchengast) |
| 2 | 13 December 2017 | | Updated after RO SAG 04 meeting, including:<br>• general EPS-SG info added (orbit, mass, lifetime)<br>• references moved to the end<br>• acronym appendix place holder added<br>• several of 1F points included, some clean up of editorial updates<br>• Sub-sections, figures added to “Instrument and RO performance monitoring” chapter<br>• “RO related data processing and products” chapter moved to second to last, with “RO research & development and Outreach Need” now last chapter |
| 2A | 18 January 2018 | | Author update of Section 5, 9, RO SAG co-chair review, preparation for publication, removal of review comments |
| 2B | 11 October 2018 | | Cleaned up version for EUMETSAT website publication. |
| 2C | 28 November 2018 | | Updated Science Plan contributor, resend to RO SAG for re-check. Included RO hardware plot in Section 4. |

# *Table of Contents*

# 1 EXECUTIVE SUMMARY

EUMETSAT Polar System (EPS-SG) / Meteorological Operational Second Generation (MetOp-SG) is a collaborative programme between ESA and EUMETSAT. EPS-SG / MetOp-SG is a follow-on system to the first generation series of MetOp satellites, which currently provide operational meteorological observations from polar Low Earth Orbit.

The main objective of the GNSS Radio Occultation (RO) mission on EPS-SG / MetOp-SG is to support operational meteorology and climate monitoring by providing measurements of bending angle profiles in the troposphere and the stratosphere with a high vertical resolution and accuracy. From bending angles, refractivity profiles can be retrieved. From these, atmospheric temperature and humidity profiles as well as information on surface pressure can be retrieved. A secondary application to be supported by the RO mission is the space weather monitoring by provision of information on the Total Electron Content and on the atmospheric electron density.

The RO instrument will provide continuous operation during the EPS-SG mission life, for more than 21 years, and will be installed on both MetOp-SG satellites A and B. Innovative features of this new RO instrument are the possibility to observe, acquire and track signals from the modernized GPS constellation, from the Galileo, and potentially GLONASS and the Compass/BeiDou navigation systems.

The RO Science Plan (SP) details the scientific work needed to meet the RO mission objectives and provides a framework for the required scientific research and development activities. It follows the *EPS-SP* [1998], which was written by the GRAS Science Advisory Group for the EPS programme, and reviews the status and on-going activities in the areas of:

- Precise Orbit Determination for the RO instrument and future signals;
- RO applications and gaps;
- RO data processing and products;
- ionosphere RO data processing and products;
- climate use of RO data;
- instrument and RO performance monitoring;
- RO research and development needs/Outreach;
- RO related data processing and products.

The SP identifies necessary research and three types of new products in the area of Numerical Weather Prediction, Climatology monitoring, Atmospheric modelling: products where new signal processing is used to improve on existing product, products arising from mature understanding of scientific needs, and products which emerge from latest research.

The SP was written and compiled by the RO Science Advisory Group, external experts and EUMETSAT/ESA.

# 2 INTRODUCTION

## 2.1 The Role of RO SAG

For the scientific preparation of the Radio Occultation (RO) mission, ESA and EUMETSAT have established the RO Science Advisory Group (RO SAG), whose members are listed in Appendix A, along with other participants to the RO SAG meetings who have also contributed to this document. Some of the objectives of this advisory group are: to advice ESA/EUMETAT on the scientific requirements of the RO mission, system, instrument, and ground processing, and especially on requirements related to the EPS-SG ground segment; to review the progress of projects initiated in support of the RO mission and to give recommendations to ESA/EUMETSAT on the direction of future work; to participate in the coordination with external groups.

## 2.2 Purpose of the Science Plan

The Science Plan details the scientific work needed to meet the RO mission objectives and provides a framework for required scientific research and development activities, it follows the EPS Science Plan [*EPS-SP*, 1998], which was written by the GRAS SAG for the EPS programme. By reviewing on-going activities in the areas of retrievals, software and databases, the level of compliance with the user needs can be established and the need for additional study and development identified.

# 3 MISSION OBJECTIVES

## 3.1 EUMSATSAT Polar System–Second Generation (EPS-SG)

According to the EUMETSAT Convention [*Convention*, 1991] "*The primary objective of EUMETSAT is to establish, maintain and exploit European systems of operational meteorological satellites, taking into account as far as possible the recommendations of the World Meteorological Organisation. A further objective of EUMETSAT is to contribute to the operational monitoring of the climate and the detection of global climatic changes.*"

The Convention further stipulates that the EUMETSAT mandatory programmes include "the basic programmes required to continue the provision of observations from geostationary and polar orbits".

Therefore, in accordance with the terms of the Convention, the EPS-SG Programme will be a mandatory EUMETSAT programme addressing the need of continuity with EPS and mission requirements in the areas of operational meteorology and climate monitoring.

The EUMETSAT Strategy 2030 [Strategy, 2006] gives additional focus in stating "*A primary objective for EUMETSAT is to be a key component of the future global Low Earth system, initially with a focus on an advanced sounding capability in the mid-morning orbit.", and further opens the perspective of additional services by stating: "Whilst maintaining the priority of operational meteorological and climate services, the development of new services in the environment should cover the oceans, atmosphere, land and biosphere, and natural disasters to the extent that they interact with, drive or are driven by meteorology and climate. New satellite services are foreseen particularly in the context of the European Global Monitoring for Environment and Security initiative (GMES).*"

In line with the above, the high level objectives of the EPS-SG programme are, in order of priority:

1. To support **operational meteorology**, continuing and enhancing the core relevant services provided by EPS, with a focus on advanced sounding capability in the mid-morning orbit and in accordance with agreed user needs and priorities, and taking into account WMO requirements as far as possible;
2. To provide operational services in support of **climate monitoring** and detection of global climatic changes in the frame of relevant international initiatives, through cooperation and partnership, and taking into account GCOS requirements as far as possible;
3. To develop new **environmental services** covering the oceans, atmosphere, land and biosphere and natural disasters to the extent that they interact with, drive or are driven by meteorology and climate.

The candidate EPS-SG missions were identified by the Post-EPS Mission Experts Team (PMET) in the *MRD* [2011], and narrowed down after industrial Phase 0 studies in the Post-EPS Mission Definition Review.

The mission of the EPS-SG System is to provide global observations from which information on variables of the atmosphere and the ocean and land surfaces can be derived, using satellite based sensors from the Low-Earth Orbit (LEO). To fulfil its mission it is required to deploy sustained capabilities to acquire, process, and distribute to down-stream application users and second tier processing centres environmental data on a broad spectral range (from UV to MW), covering extensive areas (global and regional), and within a variety of different time scales to continue and enhance the services offered by the EPS.

The EPS-SG will consist of 2 satellites (called A and B), they will fly in the "same" orbit as EPS, for more information please see Table 1.

***Table 1 Concept of the MetOp-SG program with candidate sensor complement and leading agency.***

| | **Metop-SG A** | **Metop-SG B** |
|---|---|---|
| First Launch | Currently mid-2021 | Currently end of 2022 |
| Orbit and Altitude | LEO, 817km, Sun-synchronous, local time of the descending equator crossing of 09:30 | LEO, 817km, Sun-synchronous, local time of the descending equator crossing of 09:30 |
| Mass | ~4200kg | ~4000kg |
| Design Lifetime | 7.5 years | 7.5 years |
| **Instruments** | | |
| | METimage (DLR) | MWI (Microwave Imaging Radiometer), (ESA) |
| | MWS (Microwave Sounder), (ESA) | ICI (Ice Cloud Imager), (ESA) |
| | IASI-NG (Infrared Atmospheric Sounder Interferometer-Next Generation), (CNES) | SCA (Scatterometer), (ESA) |
| | RO (Radio Occultation), (ESA) | RO (Radio Occultation), (ESA) |
| | 3MI (Multi-view Multi-channel Multi-polarization Imager), (ESA) | Argos-4 (Data Collection Service) (NOAA/CNES) |
| | Radiation Energy Radiometer (NOAA) | Search and Rescue (COSPAS-SARSAT) |
| | UVNS/Sentinel-5 (ESA/Copernicus) | Space Environment Monitor (NOAA) |
| | Low Light Imager (NOAA) | |

The EPS-SG observation missions/instruments are:

- the Infra-red Atmospheric Sounding mission (IAS), covering a wide swath of hyper-spectral infra-red soundings in four spectral bands, covering the spectral domain from 3.62 to 15.5 µm at a spatial sampling of about 25 km;

- the Microwave Sounding Mission (MWS), allowing for all-weather soundings over a wide swath in the spectral region between 23 and 229 GHz, at a spatial sampling of about 30 km;
- the Scatterometry Mission (SCA), providing back-scattered signals in the 5.355 GHz band at a spatial resolution of 25 km;
- the Visible/Infra-red Imaging mission (VII), providing cross-purpose, moderate-resolution optical imaging in ≥20 spectral channels ranging from 0.443 to 13.345 µm with a spatial sampling of 500 m;
- the Microwave Imaging Mission (MWI), providing precipitation and cloud imaging in the spectral range from 18.7 to 183 GHz at a spatial sampling of about 8 km (highest frequency) to 12 km (lowest frequency);
- the Ice Cloud Imaging Mission (ICI), providing ice-cloud and water-vapour imaging in the spectral range from 183 to 664 GHz at a spatial sampling of < 15 km.
- the Radio Occultation Mission (RO), providing high vertical resolution, all-weather soundings by tracking GPS (Global Positioning System) and Galileo satellites;
- the Nadir-viewing Ultraviolet, Visible, Near-infra-red, Short-wave-infra-red sounding mission (UVNS), providing hyper-spectral sounding with a spectral resolution from 0.05 to 1 nm within the spectral range from 0.27 to 2.4 µm at a spatial sampling of 7 km;
- the Multi-viewing Multi-channel Multi-polarisation Imaging mission (3MI), providing moderate resolution aerosol imaging in the spectral region ranging from ultra-violet (0.342 µm) to short-wave infra-red (2.13 µm), at a spatial sampling of 4 km.

The space segment of the EPS-SG system will consist of a dual satellite configuration with three sounding and imaging satellites and three microwave satellites to span an operational lifetime of the programme over 21 years.

This distribution of the payload complement between the two parallel satellites gives regard to the priority of the mid-morning sounding and imaging missions (IAS, MWS, RO,VII) and the need for co-registration of missions (IAS-VII, UVNS-VII, 3MI-VII, MWI-ICI).

Complementary to the direct observation missions summarised above and yet essential to satisfy key user needs, the following objectives have also to be fulfilled by EPS-SG:

- product generation;
- Near Real Time Data Dissemination & Relay services to users;
- Non-NRT dissemination services;
- long term archiving in the EUMETSAT Data Centre;
- archived dataset retrieval services continue to be provided as part of the multi-mission EUMETSAT Data Centre services;
- user support services.

The Near Real Time (NRT) dissemination service is available for registered Users equipped with dedicated reception software licensed by EUMETSAT. The RO datasets to be delivered by this service are listed in Table 2.

***Table 2 Operational timeliness (availability in brackets) for NRT dissemination of RO products.***

| Disseminated Dataset | Threshold | | Breakthrough | |
|---|---|---|---|---|
| Global Level 1 Products 1st Priority | 110 min (50%) | 120 min (90%) | 60 min (50%) | 70 min (95%) |
| Regional Level 1 Products (Europe, N.- Atlantic) | 30 min (50%) | 110 min (90%) | 20 min (50%) | 30 min (95%) |
| SAF NRT Products | | 150 min (90%) | | 80 min (95%) |

Notes:

- the numbers in brackets give the amount of data to be available with the given timeliness.
- the regional service covers Europe and North Atlantic Ocean, the regions bound by 65°W, 30°N and 50°E, 80°N. For RO, profiles outside of this area are also provided when they are acquired by a ground station covering the regional service.

## 3.2 Radio Occultation (RO)

The Radio Occultation (RO) receiver has a direct heritage from instruments such as GRAS, flying on Metop [GNSS (Global Navigation Satellite System) Receiver for Atmospheric Sounding, see e.g. *EPS-SP* [1998], *Loiselet et al.* [2000], *Luntama et al.* [2008]], COSMIC, Champ, and the precursor GPS/MET (for an overview of these missions, see e.g. *Anthes et al.* [2011]).

The main objective of the GNSS RO mission is to support NWP and climate monitoring by providing measurements of bending angle profiles in the troposphere and the stratosphere with a high vertical resolution and accuracy in Near Real Time. From bending angles refractivity profiles can be retrieved. From these, atmospheric temperature and humidity profiles as well as information on surface pressure can be retrieved. A secondary application to be supported by the RO mission is the space weather monitoring by provision of information on e.g. the Total Electron Content and on the atmospheric electron density.

In summary, the RO mission will provide information on the following atmospheric variables in the global and regional service (either from EUMETSAT or the ROM SAF, indicating also the expected NRT product availability where Day-1 refers to available after commissioning):

- bending angle profile (Day-1 product);
- refractivity profile (Day-1 product);
- temperature and dry temperature profile (Day-1 product);
- pressure profile (Day-1 product);
- surface pressure (Day-1 product);
- water vapour profile (Day-1 product);
- tropopause height (Day-1 product);
- height of the planetary boundary layer (Day-1 product);

- total electron content (supporting space weather, Day-1 or Day-2 product);
- electron density profile (supporting space weather, Day-1 or Day-2 product);
- amplitude and phase scintillations (supporting space weather, Day-1 or Day-2 product).

# 4 EPS-SG RO INSTRUMENT

## 4.1 Heritage

The RO instrument on EPS-SG (RO-SG in what follows) has a direct heritage from GRAS, the RO instrument flying within the EPS program [*EPS-SP*, 1998; *Loiselet et al.* 2000; *Luntama et al.* 2008]. The measurement concept was developed and proven within the GPS/MET proof-of-concept mission, and later used for RO missions such as CHAMP, Grace, COSMIC, etc. For an overview of missions, please refer to the **[***IROWG-GOS*, 2013**]**.

## 4.2 Instrument Hardware

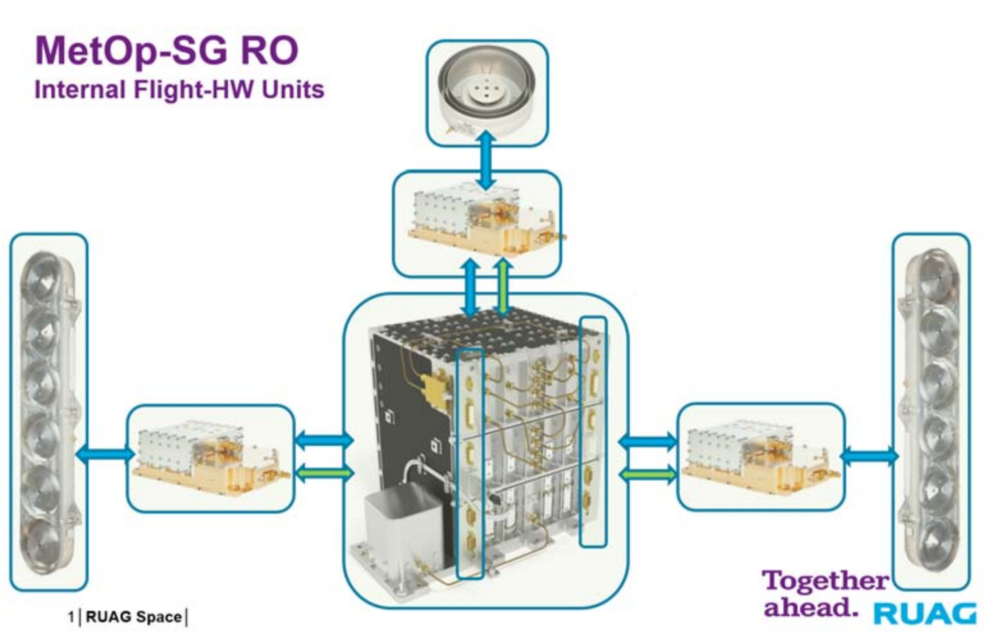


***Figure 1 EPS-SG RO Hardware Components. Provided by RUAG, Sweden.***

The RO-SG instrument will provide continuous operation during the EPS-SG mission life, for more than 21 years, and will be installed on both MetOp-SG satellites A and B. The hardware components are shown in Figure 1.

Innovative features of this new RO-SG instrument are the possibility to observe, acquire and track signals from the modernized GPS constellation, from the Galileo, and maybe from the future, CDMA based, GLONASS and the Compass/BeiDou navigation systems, handling the combinations of the dual-frequency signals listed in Table 3 from the same GNSS satellite.

The RO-SG instrument will provide more than 1100 occultation measurements per day, thanks to simultaneous tracking of Galileo and GPS satellites (baseline). This coverage may possibly double with the Compass-BeiDou and GLONASS constellations.

GNSS signals on L1/E1 and L5/E5a frequencies are tracked by means of both Closed loop and Open loop tracking. Both data and pilot signal components can be tracked simultaneously. The RO-SG will try to acquire as fast as possible all the signals exploiting a new full open-loop tracking strategy, aiding both the code phase and the carrier phase tracking through the use of a range/Doppler model. The standard closed-loop tracking is also implemented.

The signals from the occulting satellites are received through two antennas, one dedicated to rising occultations and the other dedicated to setting occultations, both focused on the Earth's limb. The instrument also acquires and tracks GNSS signals via a third, zenith pointing antenna with a wide conical coverage. It provides the associated observables for Precise Orbit Determination (POD) purposes.

GNSS signals received by the three antennas are amplified by Low Noise Amplifiers and splitted into the different signal bands, down-converted to baseband and digitalized. Either in closed-loop tracking or in open-loop tracking, the RO-SG receiver will make available very low level GNSS signal components, basically:

- I and Q components at the output of each correlator. In the new RO-SG instrument a bank of 10 correlators is used to implement the full open-loop tracking (this is referred to as wide mode tracking). Depending on the geometry, when the signal is expected to have sufficient SNR, the number of correlators used for the open-loop tracking is reduced to 5 (narrow mode tracking). Once the closed-loop tracking is reached, data coming from one correlator only are provided;
- Numerically Controlled Oscillator (NCO) carrier and code phases;
- Noise power.

These are the low level observables that will be processed later, on ground, into more standard GNSS observables like carrier phases, pseudoranges, signal amplitudes and Signal-to-Noise Ratio (SNR). This will assure the highest level of flexibility.

All the technical details of the RO-SG receiver are given in Industry Documents. A summarizing description of the instrument modes and observing modes is provided below.

***Table 3 GNSS signals and frequencies that will be tracked by RO-SG (see* [*EURD*]*, Sect.5.4). *GLONASS and **Compass-BeiDou signal ICDs are currently not available for the signals specified in the table. The assumption of future availability of these signals within the EPS-SG time frame is based on public available information.***

| System | Signal | Carrier Frequency [MHz] |
|---|---|---|
| GPS | L1 C/A | 1575.42 |
| GPS | L1 C | 1575.42 |
| GPS | L5 | 1176.45 |
| Galileo | E1-B/C | 1575.42 |
| Galileo | E5a | 1176.45 |
| GLONASS* | L1 OC | 1575.42 |
| GLONASS* | L5 OC | 1176.45 |
| Compass-BeiDou** | B1 | 1575.42 |
| Compass-BeiDou** | B2A | 1176.45 |

The RO-SG instrument represents times in two different ways:

- On-board Time (OBT): This is the spacecraft time in Consultative Committee for Space Data Systems (CCSDS) Time Code format. OBT is distributed via the spacecraft communication network. A Local On-Board Time (LOBT) synchronised with OBT is maintained by the instrument and used to time stamp events and telemetry;
- Instrument Measurement Time (IMT): This is the time used by the instrument to time-tag all the GNSS observables. It is an integer counter which is adopted to precisely time stamps individual measurement data samples. Each GNSS Receiver Module (GRM) forming the RO-SG (there are four GRMs, one for each antenna plus one redundant for the zenith antenna) has its own IMT and they are all derived from the same frequency source (the Ultra Stable Oscillator (USO)) so their frequencies are identical but the epoch (time 0) may differ.

Such times representations will be converted to one unique time scale by the on ground processing, where other necessary information is available (GPS time, Galileo System Time and their relationship with the Coordinated Universal Time (UTC)). This unique time scale will be used to time stamp all the reconstructed GNSS observables.

## 4.3 Observation Modes

Looking at occultations, there are a number of different phases (defined tracking states) that are traversed, these depend on the geometric relationship between the receiver, the GNSS space vehicle and (for RO measurements) the Earth. The different tracking states address different algorithms for the reconstruction of standard GNSS observables.

For the Navigation mode the RO-SG will be characterized by standard, already well known tracking algorithms. New tracking strategies are implemented in the Occultation mode in order to allow a longer signal availability coming from the limb sounding observations. As for the GRAS receiver, two main tracking schemas are applied in occultation mode: the standard closed-loop and an open-loop one. The closed-loop schema is sufficient to track signals in the ionosphere and the higher neutral atmospheric layers. During this tracking state, both code and carrier phase of each GNSS received signals are locked, and the provided NCO carrier and code phases are enough to reconstruct the standard GNSS observables.

The open-loop tracking instead makes the receiver more robust to the stronger dynamics expected when the signal is passing through the troposphere. In the GRAS instrument, this open-loop schema was applied only to the carrier phase tracking, while the code phase tracking was implemented through a standard Delay Locked Loop (DLL). In the RO-SG receiver, the code phase tracking is also implemented following an open-loop schema. As for the carrier phase, also for the code phase an on-board model is available. This model will provide one of the components necessary to compute the final carrier phases and code phases.

The other components will be derived by the provided I, Q signal components from multiple correlators (10 correlators in the wide mode tracking, or 5 correlators in the narrow mode tracking, depending on the Straight Line Tangent Altitude (SLTA)) and by the provided NCOs code and carrier phases. Open-loop and closed-loop tracking will be performed in parallel, insuring a discrete overlap between data. The overlapping can be easily extended by configuration parameters, provided that the maximum data rate is not violated.

Finally, another improvement of the new RO-SG receiver is the use of pilot GNSS signals. Since these signals are not modulated by any navigation message, their tracking is easier and faster and it can provide a useful aid for the tracking of the standard data signals. This aspect will be taken into account by the on ground processing.

The possible closed loop tracking frequencies are given in Table 4. Open loop is performed with either 200 Hz or 250 Hz.

***Table 4 Closed-loop sampling rates.***

| Height Range [km] | Sampling Rates [Hz] |
|---|---|
| 0– 30 | 10, 50, 200, 250 |
| 30 – 150 | 10, 50, 200, 250 |
| 150 – 500 | 1.0, 5.0, 10, 50, 200, 250 |

The RO instrument only tracks the signal in open loop mode when the received power is very low and not sufficient to acquire the signal. This will occur at the lower part of the atmosphere, until ~ 20 km SLTA (this parameter is configurable). Once the received signal power is above a threshold, the RO instrument acquires the signal and track it in closed loop mode. The accuracy of the measurements at 200/250 Hz in closed loop mode is higher than in open loop mode. Therefore, in the ionosphere the RO instrument will always work in closed loop mode.

Since the SLTA at which open loop starts/terminates is configurable, there is the possibility to set the RO instrument to track at all altitudes at open loop, allowing high sampling frequencies also in the stratosphere and thermosphere / ionosphere. Data rates and available channels are considered sufficient to support this. This setting is however not the baseline.

## 4.4 Bending Angle Requirements

Partly based on EPS GRAS [*Loiselet et al.* 2000], the *EURD* [2016] gives the bending angle (BA) accuracy at Threshold level as:

- 1 µrad or 0.4% of the BA between 35 to 80 km, considering whichever value is larger;
- from 0.4% to 1% of the BA linearly in height between 35 km and 10 km;
- from 1% to 10% of the BA linearly in height between 10 km and the surface.

At Breakthrough level, accuracy shall be better than:

- 0.5 µrad or 0.2% of the BA between 35 to 80 km, considering whichever value is larger;
- from 0.2% to 0.5% of the BA linearly in height between 35 km and 10 km;
- from 0.5% to 5% of the BA linearly in height between 10 km and the surface.

# 5 POD FOR THE RO INSTRUMENT AND FUTURE SIGNALS [AH, JI]

The development of new Global Navigation Satellite Systems (GNSSs) and the modernization of legacy systems cause significant changes in satellite navigation environment over the last decade. The GPS constellation operated by the US Air Force is undergoing a modernization through the launch of new generations of satellites, which introduce new signals and frequencies. The Russian GLONASS system is expected to follow this development with a new generation of satellites in the future. The European Galileo system gains momentum in the deployment of its constellation and the declaration of initial services in December 2016.The Chinese BeiDou system already offers regional navigation service in the Asia-Pacific region and will now expand beyond this state to a global system. All of these developments are work in progress and are likely to last at least until the end of 2020.

In case of GPS and Galileo, interface control documents of the relevant signals for EPS-SG are published and provide confidence about the signal specification of the future signals, which is necessary for the development of user equipment. However, the performance of these new signals for precise orbit determination (POD) of space vehicles (SVs) and radio occultation (RO) applications has yet to be assessed.

In case of BeiDou and GLONASS, predictions about the future constellations are more ambiguous. At the time of writing, a test ICD has been published for the future BeiDou 3 signals relevant to EPS-SG. In case of GLONASS, ICDs for the future CDMA signals have been released, but none of them are on frequencies that are relevant to EPS-SG. The timeline of the deployment for a full BeiDou and GLONASS constellation with signals relevant to EPS-SG is subject to speculation at this point in time.

Japan’s regional Quasi Zenith Satellite System (QZSS) has reached full deployment of a four satellite constellation in 2017. The satellites transmit GPS-compatible signals and an ICD has been published. Therefore using QZSS satellites for RO may be an interesting alternative in view of the uncertainties in the deployment status of the other constellations.

The current status and the expected development until 2020 of these five relevant global satellite navigation systems is briefly discussed and potential issues which deserve special attention for the development of a future RO instruments are pointed out. The discussion of GNSS signals is limited to the signals usable without special authorization. Afterwards, different options for POD processing and instrument monitoring are discussed.

## 5.1 Overview of GNSSs

The following sections will provide a brief overview of the current status of the global navigation systems GPS, GLONASS, Galileo, BeiDou, and QZSS. The majority of RO measurements will stem from these systems, provided that the constellations are fully deployed and all satellites provide the necessary signals. Regional navigation systems like the Indian Regional Navigation Satellite System (IRNSS) and other Satellite Based Augmentation Systems (SBASs) are not considered. All statements about the constellation status refer to the time of writing at December, 2017.

### 5.1.1 GPS

The current GPS constellation as of December 2017 consists of three types of satellites with different capabilities: The oldest Block IIR satellites transmit the legacy signals C/A code and P(Y) in the frequency band L1 centred at 1575.42 MHz, and P(Y) code in the frequency band L2 centred at 1227.60 MHz. The civil C/A code signals can be tracked directly, whereas tracking of the P(Y) signals is only possible through codeless or semi-codeless tracking techniques. The Block IIR-M satellites are a modernized version of the Block IIR type. One of several design modifications has been the addition of a new civil signal L2C on L2. The latest generation of GPS satellites in the current constellation is the Block IIF type. It provides the legacy signals, the L2C signals, and an additional civil signal in the L5 frequency band centred at 1176.45 MHz. The future GPS Block III satellites will broadcast another new civil signal L1C on L1 in addition to the Block IIF signals.

The GPS constellation as of December 2017 consists of 31 operational satellites. A large fraction of the constellation consists of Block IIR (12 SVs) satellites. The Block IIR-M satellites amount to 7 spacecraft. BlockIIR and IIR-M satellites are no longer produced and all available units have been launched. The Block IIF satellites with L5 signal capabilities have recently been added to the constellation following a rapid launch schedule. Twelve satellites of this type have been produced and put into orbit. The newly developed GPS Block III satellites are currently in production. Manufacturing of the first ten spacecraft has been contracted and the first six space-vehicles are already in different stages of production. The launch of the first Block III satellite is expected in 2018 and the entire batch of 10 satellites will be launched until 2023. [*GPSW2016-Budget*, 2016]. Additional contracts for up to 22 space vehicles will be awarded in the future. The deployment of these additional satellites is currently foreseen to take place between 2026 and 2034 [Whitney, 2017]. An overview of satellite block types is provided in Table 5.

***Table 5: Overview of current and future GPS satellites as of December 2017.***

| Satellite Type | Civil Signals | # active | # to be launched | Notes |
|---|---|---|---|---|
| Block IIR | L1 C/A, L1/L2 P(Y) | 12 | - | |
| Block IIR-M | all Block IIR + L2C | 7 | - | |
| Block IIF | all Block IIR-M + L5 | 12 | - | |
| Block III | all Block IIF + L1C | | 10 (+up to 22) | 1st launch expected 2018 |

It is planned to discontinue codeless and semi-codeless access to the L1/L2 P(Y) signals in the future. The 2014 Federal Radionavigation Plan states, that the signal access is not discontinued until 24 satellites on orbit transmit the new L5 signal, which is estimated to occur in 2024. It is also interesting to note that 24 operational satellites with L2C signal capability are expected to be available by 2018 [*FedRadNavPlan*, 2014].

If the 24 satellites with L5 signal transmission capability are favourably distributed in the orbital slots, a continuous availability of L1/L5 dual-frequency navigation solution anywhere on the globe is possible with GPS only. However, the reduced number of satellites will lead to lower redundancy of observations, which adversely affects the robustness of measurement outlier detection. As a result, dual-frequency navigation solutions or precise orbit determination results are likely to be of lower accuracy compared to the results obtained currently using the L1/L2 observations from the full constellation.

The short-term stability of GNSS clocks is assessed using the 1-way carrier-phase method. High-rate data sampled at 1 Hz from a receiver connected to an H-maser has been used for the analysis. The Allan deviation has been computed based on one-hour time series of single-frequency carrier-phase observations, which are centred at the highest point of a satellite's pass. The receiver-satellite range is removed from the observations with precise orbit information. The residual effects of carrier-phase ambiguity, troposphere, ionosphere and biases are removed with a 3rd-order polynomial fit. This method yields reliable results for averaging intervals up to 1000 seconds [*A. Hauschild et al.*, 2013]. The same method is also used for the clock assessment of GLONASS, Galileo, and BeiDou in the following sections.

The plot in Figure 2 depicts results for Allan deviation from a short-term clock characterization of the atomic frequency standards (AFSs) of the current GPS constellation for averaging intervals between 1 second and 1000 seconds. The satellites of type Block IIR and Block IIR-M are equipped with Rubidium AFSs exclusively. It becomes obvious that all satellites have a similar performance. The newer Block IIR-M satellites tend to have a lower Allan deviation of about 3e-12 at 1 second averaging interval compared to the older Block IIR satellites, which typically reach about 4e-12 at this interval.

The newest generation of Block IIF satellites is equipped with Rubidium and Cesium AFSs. The majority of these satellites are currently operated on Rubidium clocks, which are the most stable clocks in the constellation for time intervals greater than 4 seconds. Interestingly, for shorter time intervals, these clocks have a larger Allan deviation compared to the previous generation of Rubidium AFSs. Two Block IIF satellites are operated using its Cesium clock, which exhibits a significantly reduced performance.

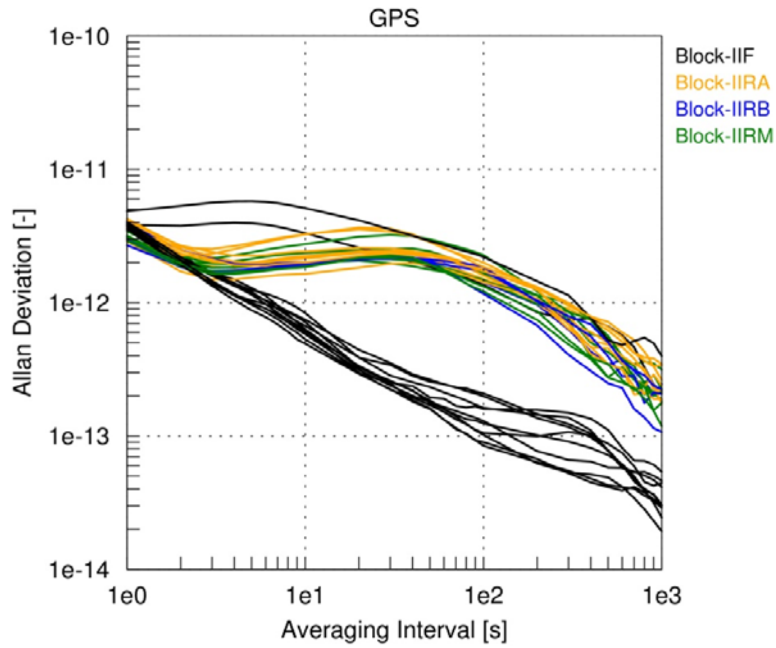


***Figure 2: Short term Allan deviations for current GPS satellite clocks.***

An important feature to consider for processing triple-frequency data from the Block IIF satellites is a thermally induced bias variation in the signals of some or all of the transmitted frequencies [*Montenbruck et al.*, 2012]. This effect leads to an inconsistency between a satellite clock correction derived from L1/L2 or L1/L5 data and is depicted in Figure 3. The peak-to-peak amplitude of the clock offset differences depends on the sun's illumination of the satellite. The effect amounts to 20 cm in the worst case and repeats with the orbital period. As a result, for a precise orbit determination with L1/L5 data, the effect must either be corrected for by an empirical model developed in *Montenbruck et al.* [2012] or clock correction values derived from L1/L5 observations must be used.

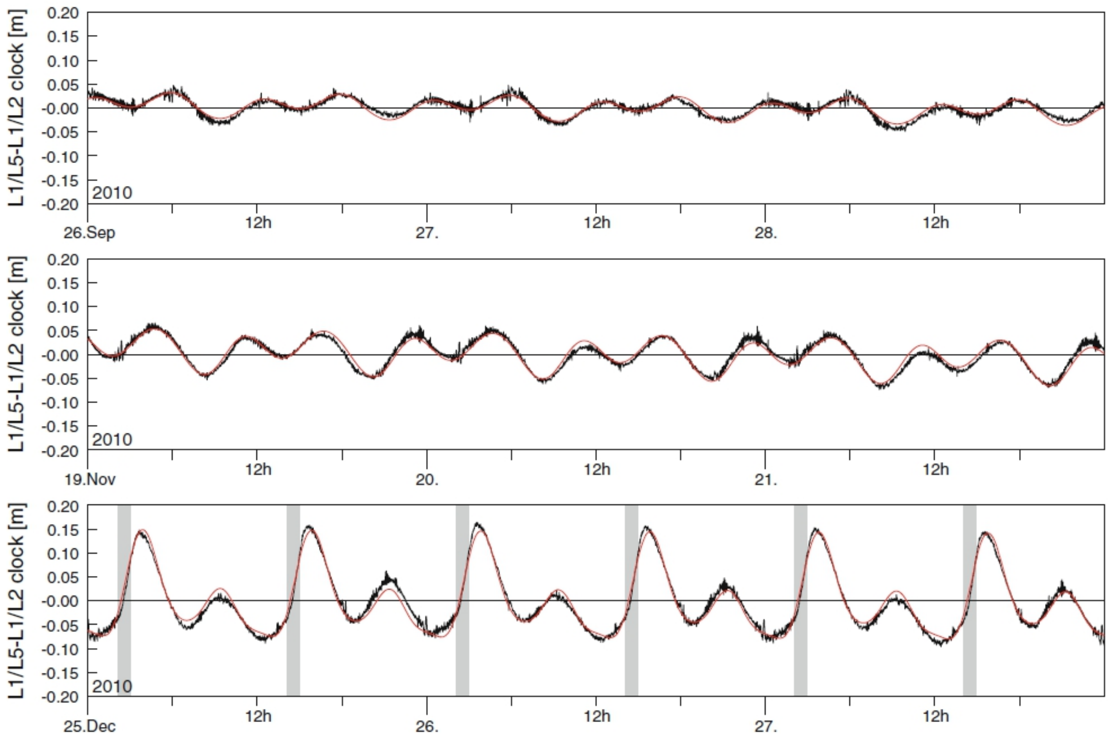


***Figure 3: Variation of the L1/L2-L1/L5 clock offset of a Block IIF satellite (from Montenbruck et al. [2012]).***

### 5.1.2 GLONASS

The current operational GLONASS constellation consists of 24 satellites, which transmit frequency-division multiple-access (FDMA) signals at two frequency bands. The first band is centred at 1602.0 MHz and thus located near the GPS L1 band. The other band is centred at 1246.0 MHz, close to GPS L2. Contrary to the code-division multiple-access (CDMA) concept, where all satellites use the same centre frequencies for their signals and the individual satellites are distinguished through a unique code sequence modulated on their signal, all GLONASS satellites transmit identical signal modulations, but each satellites uses a slightly different frequency shifted by integer multiples of 0.5625 MHz from the centre frequency at L1 and 0.4375 MHz from the centre frequency in L2.

More precisely, 15 different frequencies (or channels) are available and two satellites located on opposite sides of the earth share one channel. The reception of GLONASS signals therefore requires a different user equipment design compared to the other GNSSs. The operational constellation as of December 2017 consists of modernized GLONASS-M satellites and one next generation GLONASS-K1 satellite. Although almost the entire GLONASS constellation as of the same satellite type, notable differences in received signal power levels and satellite onboard clock performance for individual satellites indicate that design changes and improvements have been made throughout its production.

Future developments of GLONASS will introduce GLONASS CDMA signals in addition to the legacy signals. First steps towards this goal have been made with the production and launch of two new GLONASS-K1 satellites in 2011 and 2014, which transmit the legacy signals and an additional CDMA signal on a frequency denoted as L3. This frequency band is centred at 1202.025 MHz and is therefore different from the GPS L5 frequency. Also, the last GLONASS-M satellite added to the constellation in June 2014 transmits CDMA signals on L3 [*InsideGNSS*, 2014]. This signal will also be present on all future GLONASS-M satellites. There are sufficient satellites in stock on ground to maintain the constellation fully operational [*Karutin*, 2016].

Original planning only accounted for two GLONASS-K1 satellites to be built as test satellites. A series of newly developed GLONASS-K2 satellites with additional CDMA signals should have followed and integrated into the operational constellation. However, plans have been adjusted. The second GLONASS-K1 has become an operational satellite and nine additional enhanced GLONASS-K1 satellites will be included in the constellation [*GPSW2015-GLOK1*, 2015]. The enhanced GLONASS-K1 satellites will transmit L1, L2 and L3 CDMA signals [*Karutin*, 2016]. The first launch of a GLONASS-K2 satellite is now foreseen for 2018 [*GPSW2015-GLOK2,* 2014].

In addition to new signals, the latest generation of GLONASS-M satellites carry improved atomic frequency standards with improved performance. The second GLONASS-K1 satellite launched in February 2016 is equipped with the first Rubidium atomic frequency standard ever utilized for GLONASS. The future GLONASS-K2 satellites will be equipped with a newly developed passive hydrogen maser (PHM). The PHM's stability is expected to exceed all other GLONASS AFS and will be tested onboard the first GLONASS-K2 satellite scheduled for launch in 2018.

Signal specifications for the legacy FDMA are available to the public through an official interface control document. Official interface control documents for the L1, L2 and L3 CDMA signals have been released in December 2016 and are by now also available in English. According to these ICDs, the centre frequencies of the GLONASS CDMA signals do not coincide with the centre frequencies of the GPS, Galileo or BeiDou signals. Future GLONASS CDMA signals which are interoperable with GPS, Galileo or BeiDou are currently under study, but it is unlikely that they will be introduced into the operational constellation in the foreseeable future.

***Table 6: Overview of current and future GLONASS satellites as of December 2017.***

| Satellite Type | Open Service Signals | # active (+ # unhealthy) | # to be launched | Notes |
|---|---|---|---|---|
| GLONASS-M | L1, L2 FDMA | 21 | - | |
| GLONASS-M+ | L1, L2 FDMA + L3 CDMA | 1 | 6 | |
| GLONASS-K1 | L1, L2 FDMA + L3 CDMA | 1 (+1) | 9 | One SV operational, One SV in orbit testing |

| | | | | |
|---|---|---|---|---|
| GLONASS-K2 | L1, L2 FDMA, + L1, L2, L3 CDMA | 0 | ?? | Exact signals capabilities still TBD |

The Allan deviation results for the current operational constellation of GLONASS-M satellites and one GLONASS-K1 test satellite are depicted Figure 4. Only little information is publicly available about the frequency standards on board the GLONASS satellites. However, the GLONASS-M satellites exclusively use Cesium AFSs. To allow a distinction, the SVs have been grouped depending on the year of launch for this analysis. It becomes obvious that the individual satellites in the constellation exhibit significantly different performance, which can either be attributed to the use of different clock models or to aging effects of the clocks depending on their duration of operation. The plot in Figure 4 shows, that the most recently launched satellites tend to have the lowest Allan deviation (ADEV) at averaging intervals larger than 4 seconds. At the shortest time interval of 1 second, the two most recently launched satellites reach an ADEV of about 7e-12. Surprisingly, the GLONASS-K1 satellite launched in 2014 does not exhibit a significantly lower Allan deviation than the newest GLONASS-M satellites although it is reportedly equipped with an improved Rubidium AFS. Earlier analysis for a dataset if June 2015 yielded a different result, where the GLONASS-K1 satellite AFS has outperformed all other clocks for averaging intervals between 2 and 30 seconds. The results depicted in Figure 4 suggest that the satellite's clock has been switched to a Cesium AFS instead with similar performance to the GLONASS-M satellites.

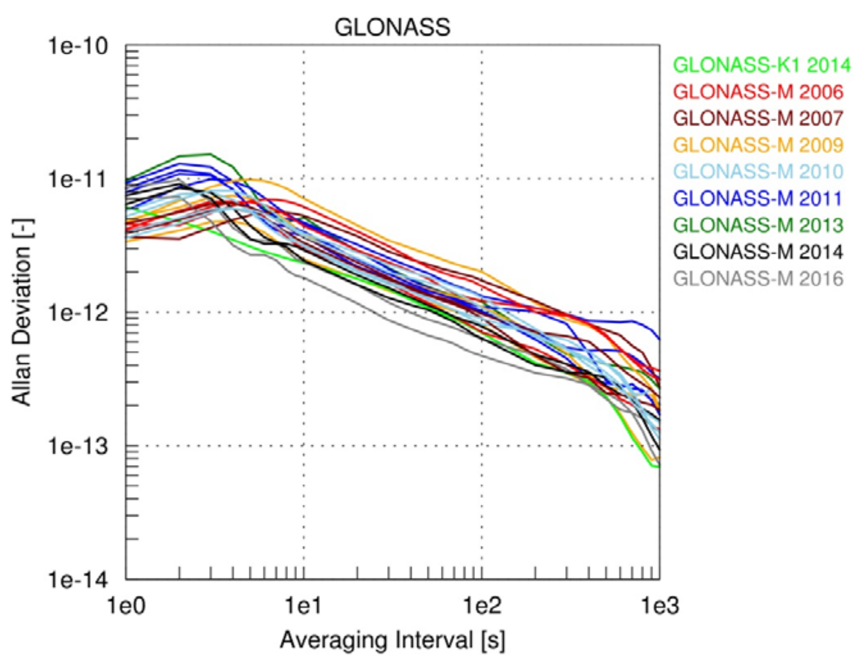


***Figure 4: Short term Allan deviation for current GLONASS satellite clocks.***

### 5.1.3 Galileo

The Galileo constellation is still in the stage of deployment in December 2017. It currently consists of 4 in-orbit validation (IOV) satellites launched in 2011 and 2012, and 18 satellites with full operational capability (FOC) launched between 2014 and 2017. The next launch of four Galileo FOC satellites is scheduled for 2018 [*Chatre*, 2017] followed by four more launches of two satellites each between 2019 and 2021.

The signal generation unit on board one of the IOV satellites is permanently damaged. This satellite transmits only single-frequency signals and is permanently flagged unhealthy. The third IOV satellite is operated with a reduced transmission power, but is otherwise healthy and fully usable.

The first two FOC satellites could not be placed into their nominal orbits due to an injection failure of the launcher's upper stage. The orbits of these satellites have a significantly larger eccentricity compared to the almost circular nominal orbits. As a result, the orbit information cannot be transmitted in the satellite almanac due to format restrictions. The satellites are currently set unhealthy, but are otherwise fully functional and transmit standard signals with navigation data content. It is therefore investigated if these satellites can be set healthy in the future without being included in the almanac. The acquisition of these satellites may take longer or require special firmware adaptions due to the missing almanac information [*Falcone*, 2016]. The four FOC satellites of the most recent launch on December 12, 2017, are still in early operations phase and will become usable in 2018. With the additional launch of four satellites in 2018, the Galileo constellation will reach its full deployment of 26 satellites [*Quiles*, 2017]. It is not quite clear if the remaining eight satellites launched between 2019 and 2021 will extend the operational constellation beyond 26 spacecraft or serve as in orbit spares.

The IOV and FOC satellites transmit signals on the E1 signal band centred at 1575.42 MHz, which coincides with the GPS L1 centre frequency, on the E5a signal band centred at 1176.45 MHz, which coincides with the GPS L5 centre frequency, and on the E5b band centred at 1207.14 MHz. The signals on E5a and E5b can also be tracked in combination as the E5 AltBOC signal. Except for the IOV-4 satellite, which only transmits on E1, all IOV and FOC satellites will share the same signals [*Falcone*, 2016].

***Table 7: Overview of current and future Galileo satellites as of December 2017.***

| Satellite Type | Open Service Signals | # active (+ # unhealthy) | # to be launched | Notes |
|---|---|---|---|---|
| Galileo IOV | E1, E5a, E5b, E5 AltBOC | 3 (+1) | - | No E5 signals on IOV-4 |
| Galileo FOC | E1, E5a, E5b, E5 AltBOC | 14 (+4) | 12 | FOC-1/2 on wrong orbit |

The Allan deviation results for three IOV satellites and nine FOC satellites are depicted in Figure 5. All satellites are equipped with both Rubidium AFSs and passive hydrogen masers (PHMs). All but two satellites use the hydrogen masers clocks. The PHMs reach an ADEV of about 3e-12 at 1 second and about 1e-13 at 100 seconds. One IOV and one FOC satellite are operated on their Rubidium clocks. The lower stability of these AFSs is clearly visible in the plot.

It is also interesting to note in this context that the first two IOV satellites have in the past been affected by a high-frequency oscillation of the carrier-phase observation with a period of 6 Hz and amplitude of approximately 5 mm. The cause of this oscillation was the combination of the signals of two active onboard clocks into a single frequency reference for the signal generation. This effect has been mitigated in the meantime due to a configuration change on board the first two IOV satellites. All subsequently launched satellites have not been affected by this problem.

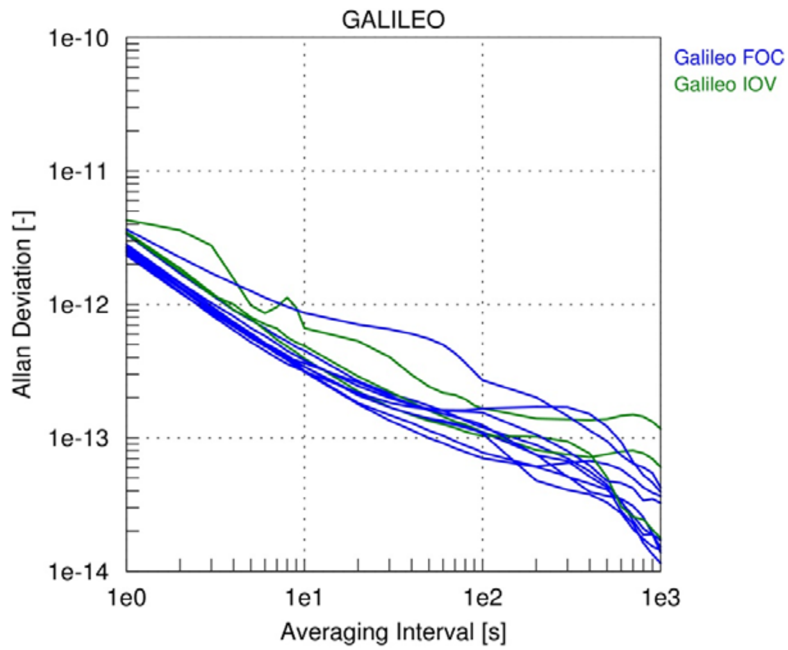


***Figure 5: Short term Allan deviation for current Galileo satellites.***

### 5.1.4 BeiDou

The Chinese BeiDou (formerly also denoted as Compass) satellite navigation system is deployed in different phases. The first generation of the system consisted of a constellation of three operational and one backup satellite on geostationary orbit (GEO). The system was based on a different mode of operation than today's satellite navigation system, which required active two-way communication between the satellites and the user terminal. The satellites of the first generation are no longer in operation.

The satellites of the second generation of the system have been deployed from 2007 until 2016 and now offer regional navigation service in the Asia-Pacific region. The current constellation consists of 5 satellites on geostationary orbit, 5 satellites on inclined geosynchronous orbit (IGSO), and 4 satellites on medium Earth orbit (MEO). One of the MEO satellite is currently not transmitting standard codes. The system's mode of operation is also based on one-way range measurements like GPS, GLONASS and Galileo. Signal specifications for these open-service signals are publicly available in an official interface control document. The satellites transmit open signals in the B1 frequency band centred at 1561.089 MHz and the B2 frequency band centred 1207.14 MHz. The latter centre frequency coincides with the Galileo E5b signal. Since the centre frequencies of the BeiDou-2 signals do not coincide with GPS L1/L5, the satellites of this constellation cannot be tracked by the RO instrument on EPS-SG.

In March 2015, a new IGSO satellite has been launched, which is the first satellite of the third generation [*GPSW2015-BDS3*, 2015]. The satellites of this generation will enable global navigation capabilities and provide new signals that are interoperable with GPS L1 and L5. Rapid deployment with 30 launches of third generation satellites has been announced to happen in 2018-2020 [*Ma*, 2017].

China initiated the deployment of the modernized, global BeiDou-3 constellation with the launch of a new IGSO satellite in March 2015 [*GPSW2015-BDS3*, 2015]. This spacecraft is the first of a series of five test satellites launched in 2015 and 2016. The satellites of this generation will enable global navigation capabilities and provide new signals that are interoperable with GPS L1 and L5. The three MEO and two IGSO test satellites are capable of transmitting both the legacy as well as the modernized BeiDou signals. An ICD of the new B1C and B2a signals has been released in November 2017. The B1C signal is centred at the GPS L1 and Galileo E1 frequency and the B2a signals is centred at 1176.45 MHz. The satellites are equipped with improved Rubidium atomic frequency standards as well as passive hydrogen masers. The latter serve as the primary on-board clock [Zhao, 2018].

In addition to these 5 test satellites, the first two BeiDou-3 MEO satellites of the operational constellation have been launched on November 5, 2017. The next launches are scheduled for January 11 and February 15, 2018. Rapid deployment with 30 launches of third generation satellites has been announced to happen in 2018-2020 [*Ma*, 2017].

***Table 8: Overview of current and future BeiDou satellites as of December 2017.***

| Satellite Type | Public Service Signals | # active (+ # unhealthy) | # to be launched | Notes |
|---|---|---|---|---|
| BeiDou-2 GEO | B1, B2 | 5 | - | |
| BeiDou-2 IGSO | B1, B2 | 5 | - | |
| BeiDou-2 MEO | B1, B2 | 3 (+1) | - | |
| BeiDou-3 GEO | TBC | 0 | 5 | |
| BeiDou-3 IGSO | TBC | 2 | 1 | |
| BeiDou-3 MEO | TBC | 3 (+2) | 22 | |

The Allan deviation results for three BeiDou-2 and four BeiDou-3 MEO satellites are depicted in Figure 6. BeiDou GEO and IGSO satellites cannot be observed from the receiver's location at sufficiently high elevation. The satellites of the BeiDou-2 constellation use Rubidium AFS from Chinese and European manufactures. It becomes obvious that the AFS of one satellite reaches an ADEV of 3e-12 at 1 second and two satellites have an ADEV of 4e-12 at the time interval.

The Allan deviation results for the four BeiDou-3 satellites comprise two MEO test satellites as well as the two satellites launched in November 2017. All four satellites exhibit a similar Allan deviation, which indicates that the same clock types are used. The analysis shows that the BeiDou-3 clocks have a better performance compared to BeiDou-2 and reach a similar performance as the GPS Block IIF RAFS and the Galileo PHM.

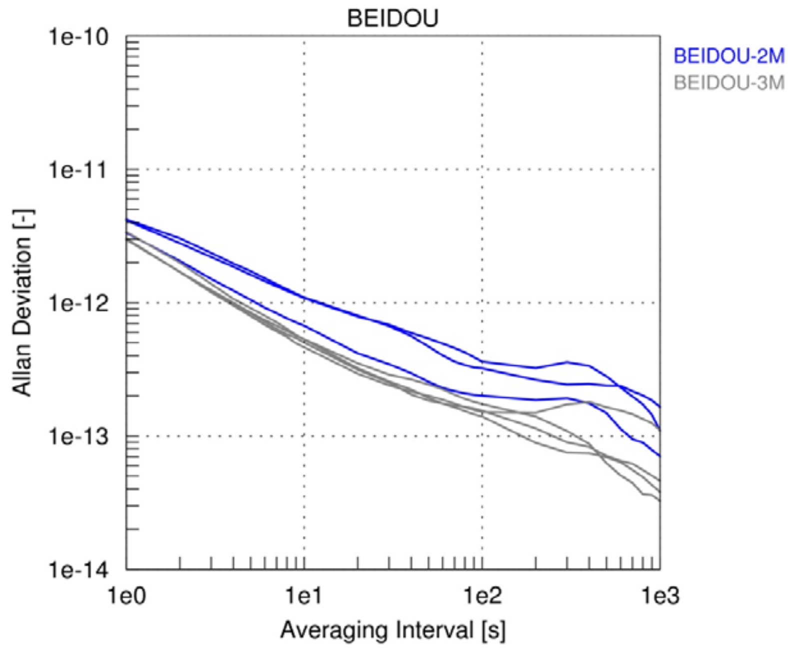


***Figure 6: Short term Allan deviation for BeiDou-2 and Beidou-3 MEO satellites.***

### 5.1.5 QZSS

The Japanese Quasi Zenith Satellite System (QZSS) is a regional navigation system, which transmits signals that are fully interoperable with GPS. The first QZSS satellite has been launched in 2010. With three additional launches in 2017, the constellation has reached its full deployment of four satellites and transmits signals on the GPS L1, L2 and L5 frequencies as well as on the LEX frequency, which coincides with Galileo E6. ICDs for all signals are published. In view of the uncertainties in the deployment status of the other GNSSs, the QZSS satellites may be a valuable substitute to be used for the generation of additional radio occultation observations.

The constellation consists of three satellites on inclined geosynchronous eccentric orbits and one geostationary satellite. The satellites also employ high quality rubidium atomic frequency (RAFS) standards, which are identical to the GPS Block IIF RAFS. Full operational service is expected to start in 2018. A replacement satellite for the oldest QZSS satellite is scheduled for launch in 2020. It is planned to extend the constellation even further to seven satellites in the near future. Three additional satellites are planned to be launched in 2022 and 2023 [*Kogure*, 2017].

### 5.1.6 Summary and Concluding Remarks on GNSS Status

The GNSS constellations are currently undergoing great changes due to the modernization of the heritage GPS and GLONASS constellations and the deployment of the new Galileo, BeiDou and QZSS systems. The following can be summarized with respect to the availability of CDMA signals on the centre frequencies 1575.45MHz (GPS L1) and 1176.42 MHz (GPS L5), which are relevant for POD and RO observations on EPS-SG:

1. the deployment of the new GPS Block III satellites with L5 signal capability is currently delayed and a full 32 satellite constellation with L1/L5 signals may not be readily available at the launch of EPS-SG;
2. the Galileo system makes great progress towards the full deployment of the constellation and will most likely be completed and in full operation by 2020;
3. the BeiDou system is currently transitioning from the regional BeiDou-2 system to the global BeiDou-3 system. Only the latter has L1/L5 compatible signals relevant for EPS-SG. A preliminary ICD for these signals has been released in 2017, which confirms their availability on the new generation of satellites. A rapid constellation deployment has been promised for 2018;
4. the GLONASS system is also been modernized and although new CDMA signals are being introduced, these signals do not share their centre frequencies with the other GNSSs. The GLONASS L1M CDMA at 1575.42 MHz and L5M CDMA at 1176.45 MHz are currently under study, but it is unclear if or when they will be introduced. Based on current information, it seems unlikely that GLONASS signals will be available at all for EPS-SG;
5. the new QZSS system is currently being deployed and fully interoperable with GPS. Although it only consists of 4 (or in the future 7) satellites, it may be a valuable substitute for the GLONASS constellation.

In view of the aforementioned delays or uncertainties, the necessary signals on L1 and L5 for the operation of the RO receiver may only be available from partly deployed constellations or may even only become available after the launch of the instrument. As a result, auxiliary products like precise GNSS clock corrections or signal bias corrections for these constellations and signals may also not yet be available from external providers like the International GNSS Service (IGS). It may therefore be necessary to procure the required products for the POD and the RO processing from an external source.

## 5.2 POD Processing Options

This section presents an overview of several POD processing options that might be relevant for future satellites equipped with GNSS receivers. Section 1.2.1 lists the higher order ionospheric (HOI) terms, which are mostly neglected in the POD of (low) Earth orbiting satellites. Different possibilities to account for these HOI terms are mentioned. In addition, it is shown that GPS tracking errors due to ionospheric scintillation might be reduced by tuning of the GPS receiver settings.

Although this is not a processing option that can be adjusted in the POD processing itself, it seems worthwhile to mention this possibility to improve the tracking performance of a GPS receiver under scintillation conditions. Section 1.2.2 focuses on integer ambiguity fixing and lists three recently developed Precise Point Positioning (PPP) integer ambiguity resolution methods. Finally, section 1.2.3 introduces antenna Phase Centre Variation (PCV) maps and briefly describes two different ways to determine empirical PCV maps.

### 5.2.1 Ionospheric Propagation Effects

The ionosphere is currently one of the largest error sources for GNSS users, especially for high-accuracy applications like PPP and real time kinematic (RTK) positioning. The ionospheric range error is proportional to the total number of electrons along the path between the satellite and the receiver and can be up to several tens of meters. The electron density in the ionosphere is highly variable, depending on e.g. altitude, local time, geographic location, season, and solar activity.

Fortunately, because the ionosphere is a dispersive medium, the magnitude of the ionospheric delay depends on the signal frequency. It is therefore possible to eliminate the major part of the ionospheric error through a linear combination of dual-frequency observables. This so-called ionosphere-free combination eliminates around 99% of the total ionospheric error. The disadvantage of using this combination is that the observation noise increases with an amplification factor that is inversely proportional to the separation of combination frequencies. For the GPS L1-L2 combination the noise increases with a factor 2.98, whereas for the L1-L5 combination the amplification factor is 2.59.

In addition, the ambiguity term of the carrier phase combination is no longer integer and higher order ionospheric terms remain uncorrected. For single frequency receivers, this linear combination cannot be applied. Instead, it is possible to use the so-called GRAPHIC combination to remove the first order ionosphere effect. This combination makes use of the fact that the first order ionosphere effect on phase and code is the same in magnitude but with opposite sign. However, this combination has the disadvantage that the resulting observation noise is half the code noise, which is usually substantially larger than the carrier phase noise.

Higher order ionospheric errors that are not eliminated when the dual-frequency combination is used are second and third order ionospheric terms, errors due to the bending of the signal and the Total Electron Count (TEC) difference at two frequencies. The range error due to these higher order effects is around 1% of the first order effect and can be up to several tens of cm at low elevation angles and during high solar activity conditions. With the current level of accuracy for the POD of low flying satellites, it becomes more and more important to also take these effects into account. For most of these higher order ionospheric effects, corrections have been developed [*Hoque and Jakowski*, 2008]. However, these corrections usually require the knowledge of parameters like the magnetic field strength or the atmospheric scale height, which are not easily available to GNSS users. This makes it quite difficult to apply these corrections in the POD processing.

When additional frequencies are available, it is also possible to make combinations using three or four frequencies to cancel out the second and third order ionospheric effect. However, these combinations generally amplify the observation noise substantially. Assuming the same noise level for each frequency, the combination using three GPS frequencies, which would eliminate the first and second order effect, has a noise amplification factor of 33.7. For a combination using the four available Galileo frequencies, the amplification factor becomes 626.1. It is clear that such noise levels significantly reduce the usefulness of these frequency combinations.

GPS receivers onboard of LEO satellites can also be affected by ionospheric scintillation. Ionospheric scintillation occurs when electromagnetic signals propagate through an irregular ionosphere. GPS signals are vulnerable to ionospheric scintillation, which can degrade or interrupt GPS receiver operations [*Kintner et al.*, 2007]. Ionospheric scintillation manifests as rapid fluctuations in the intensity and phase of the received GPS signal. The rapid phase variations cause a Doppler shift in the GPS signal, which may exceed the bandwidth of the GPS receiver phase lock loop. Additionally, amplitude fades can cause the signal-to-noise ratio to drop below the receiver threshold, resulting in loss of code lock. These effects have larger impact on GPS receivers that employ codeless and semi-codeless technologies to extract the encrypted L2 signal, compared to full code correlation [*Skone et al*., 2001].

The occurrence and intensity of ionospheric scintillation depends on e.g. geographical location, local time, season, solar cycle and geomagnetic activity. *Basu et al.* [2002] show that scintillation is most intense in the equatorial region, along two bands north and south of the geomagnetic equator. The occurrence of equatorial scintillation has strong local time dependence, with most intense scintillations after sunset. At high latitudes, scintillations are moderate and can occur at any local time, while at middle latitudes scintillations are generally absent. For a spaceborne GPS receiver, the occurrence of scintillation also depends on the spacecraft altitude. The irregularities in the ionosphere that cause scintillation occur predominantly in the F-layer of the ionosphere at altitudes between 200 and 1000 km, with most ionospheric irregularities typically between 250 and 400 km [*Aarons*, 1982].

The tracking performance of a GPS receiver under ionospheric scintillation conditions depends not only on the magnitude of the observed scintillation activity, but also on the receiver tracking capabilities. Differences in receiver performance are due to many factors, such as antenna gain patterns, internal processing algorithms and tracking loop bandwidths [*Skone et al*., 2001]. The receiver-dependent response allows tuning of the receiver parameters, in order to maximize the tracking in the presence of ionospheric scintillation. Widening of the tracking bandwidths on L2 and L1, or both, can improve the capability of tracking in the presence of a reduced signal-to-noise, as well as larger phase variations [*van Dierendonck*, 1996]. However, it would also produce noisier observations of the carrier phases. To obtain optimal receiver settings with respect to these two effects, a trade-off has to be made.

Figure 6 shows as an example the impact of modifying the bandwidth of the L1 and L2 tracking loops on the Swarm GPS receiver performance. The Swarm GPS receivers were shown to have a degraded performance when flying over areas affected by ionospheric scintillation [*van den IJssel et al*., 2015]. To improve the robustness against scintillation, the tracking bandwidths of the receiver have been widened [*van den IJssel et al*., 2016]. Because these modifications were first implemented on Swarm-C, their impact can be assessed by a comparison with the close flying Swarm-A satellite. The top panel of figure 6 shows for Swarm-A polar plots of the GPS carrier phase residuals resulting from a reduced-dynamic POD, which have pronounced systematic errors. The bottom panel shows a similar plot for Swarm-C, which has wider tracking loop bandwidths, and shows significantly reduced systematic errors.

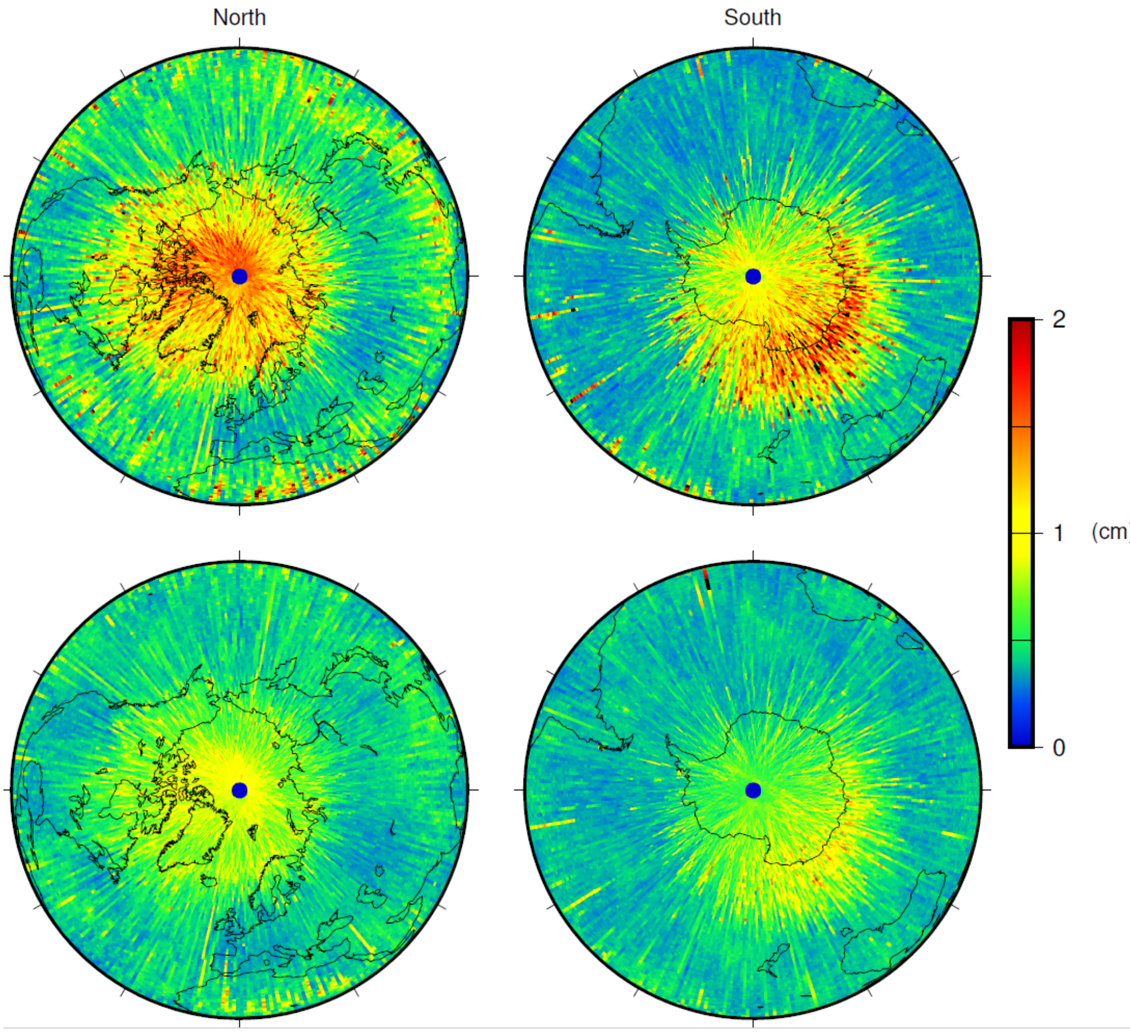


***Figure 7: Polar plots of the distribution of bin-wise RMS errors of the reduced-dynamic carrier phase residuals for Swarm-A (top panel) and Swarm-C (bottom panel) for the time period between 7 May and 21 July 2015.***

### 5.2.2 Integer ambiguity fixing

The POD accuracy usually significantly improves when the GPS carrier phase ambiguities are correctly fixed to their integer values. Until recently, the algorithms to resolve these integer ambiguities required differenced data from a pair of receivers and a pair of transmitters, in order to cancel receiver and transmitter hardware delays. However, nowadays the POD of Low Earth Orbiting (LEO) satellites is usually based on a PPP strategy using the ionosphere-free combination of dual-frequency carrier phase observations. Using this approach, the estimated ambiguity is a combination of the integer ambiguity and the receiver and satellite biases, which means that the integer property of the ambiguity is lost.

Recently, several PPP integer ambiguity resolution methods have been developed which are able to fix the carrier phase ambiguities also for PPP processing schemes. These methods include the single-difference between satellites model, the de-coupled clock model and the integer phase clock model [*Shi and Gao*, 2014]. These methods rely on advanced satellite augmentation corrections and have the potential to significantly increase the POD accuracy for LEO satellites. To benefit from such methods, it is therefore important that the integer property of the carrier phase ambiguity is maintained in the satellite receiver software.

Although this is rather straightforward, it is not always automatically done. For e.g. the GOCE satellite it seems that this was unfortunately not the case. For the current Swarm mission, the integer property of the carrier phase ambiguity is also not maintained. RUAG has indicated that the Swarm carrier-phase ambiguities probably have half-cycle properties instead. It is expected that in the near future integer fixing capabilities will become more commonly available in the different POD processing packages, and therefore it is recommended that care is taken to ensure the integer property of the carrier phase observations for GPS receivers on future Metop satellites.

### 5.2.3 Empirical Antenna Patterns

A precise knowledge of the GPS antenna phase centre location is a prerequisite for high-precision orbit determination. To obtain the most accurate orbits, it is also necessary to take GPS antenna Phase Centre Variations (PCVs) into account. Neglecting the antenna PCVs can introduce systematic errors in the POD of LEO satellites. Unfortunately, not all GPS receiver antennas have accurate PCV maps available. In addition, the PCVs of spaceborne GPS receiver antennas are generally not well determined on ground, because the ground calibration does not include the influence of error sources which are additionally encountered in the actual space environment, like near-field multipath. For spaceborne GPS receiver antennas, therefore, the PCVs are usually estimated during flight.

There are two different approaches to derive empirical phase centre corrections. In the direct approach, the PCVs of the receiver antenna are estimated directly when processing the GPS carrier phase measurements. To obtain an accurate PCV map, a long time series of GPS carrier phase observations is preferred. Therefore, usually daily normal equations are set up and accumulated for the total selected time span. The combined system is then solved for the antenna PCVs. Due to the significant computational burden and storage requirement, the resolution of the estimated PCVs with the direct approach is usually limited. This method was successfully applied to improve the JASON-1 orbits [*Lutcke et al.*, 2003].

With the residual approach, the empirical PCVs are derived as the bin-wise mean values of the GPS carrier phase residuals in the antenna frame, obtained from e.g. a reduced-dynamic POD. The residual approach is limited to recover PCVs of LEO receiver antennas, because GPS-specific parameters such as receiver clock corrections and carrier phase ambiguities partly absorb the largescale structures of the PCVs. For a fixed alignment of a spacecraft with respect to the orbital frame, e.g. for the two GRACE satellites, PCVs perpendicular to the flight direction are to some extent absorbed by the carrier phase ambiguities.

The small-scale structures of PCVs, however, can be well recovered with the residual approach. The achievable resolution of the estimated PCV map depends on the availability of long time series of residuals. When long time series are available, the resolution of the estimated antenna PCV can easily be up to 1° x 1°, which allows to take very short scale PCV structures into account. Generally, several iterations have to be performed, because parts of the unmodeled PCVs can be absorbed by other estimated parameters in the POD. This method was successfully applied to improve e.g. the orbits of the GRACE satellites [*Jäggi et al.*, 2009] and the GOCE satellite [*Bock et al.,* 2011].

Figure 8 shows as an example the empirical phase centre corrections derived for the three Swarm satellites from the ionosphere-free carrier phase residuals of reduced-dynamic orbits. For each satellite, 70 days of 1 Hz ionosphere-free carrier phase residuals were used to generate the PCV maps. In total eight iterations have been performed, after which no further significant changes were visible in the estimated PCVs and the resulting orbits. The estimated PCVs have a clear azimuth-elevation dependent pattern, with values that can be up to 20 mm. The PCVs are very similar for all three satellites, which is expected, as the GPS instruments on the Swarm satellites are identical.

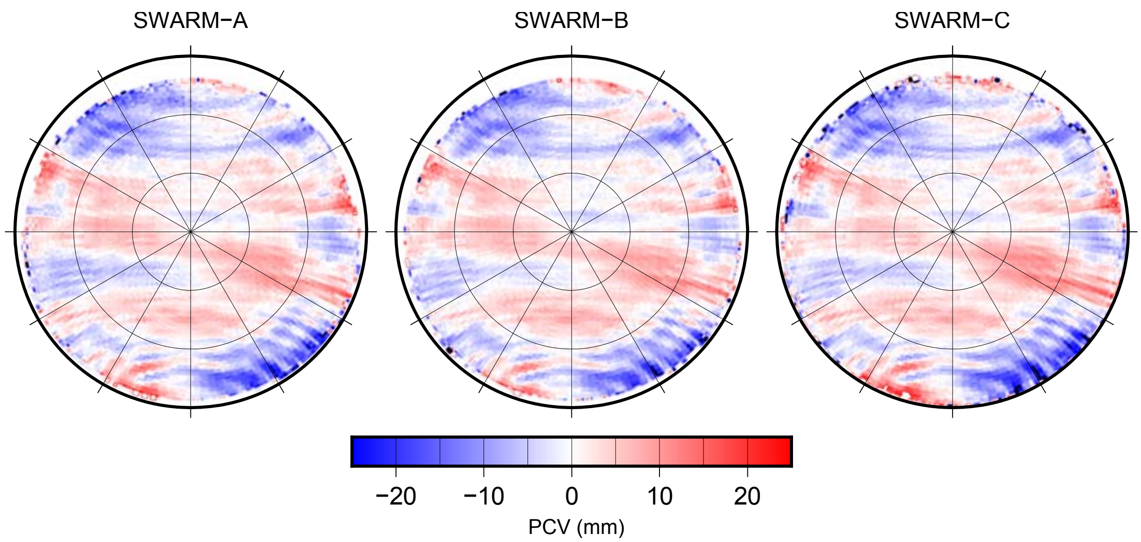


***Figure 8: Empirical PCVs for the nominal Swarm POD antennas.***

## 5.3 Instrument Monitoring

### 5.3.1 USO Characterization

The precise orbit determination process yields in addition to the satellite's trajectory also a precise clock offset estimate of the receiver's oscillator. The performance of the oscillator with respect to stability or temperature dependency can be analysed based on the time series of the clock offset estimates. Since the navigation observations and the RO observations refer to the same ultra-stable oscillator (USO), these results directly reflect the oscillator-dependent effects in the RO measurements. The following results for the USO performance on Metop-A and Metop-B have been obtained during calibration and validation activities for Metop-B in October 2012.

The results for the oscillator offsets presented in the following analysis have been obtained from a carrier-phase based precise orbit determination used a reduced-dynamic orbit model. The temporal variations of the USO of the GRAS instrument of Metop-B are depicted in Figure 9 for three selected days during the first week of the receiver activation. Directly after the activation of the GRAS instrument, the peak-to-peak amplitude of the USO clock offset was approximately 300 meters. In the course of the first week of operation, this amplitude reduced notably to about 100 meters. It is not known, if a similar change has also occurred in the USO of Metop-A, since the first systematic analysis has happened two months after the activation of the receiver. At this point in time, the USO clock offset exhibited a diurnal variation on the order of 20 meters after the removal of a second-order polynomial [*Montenbruck et al.*, 2008].

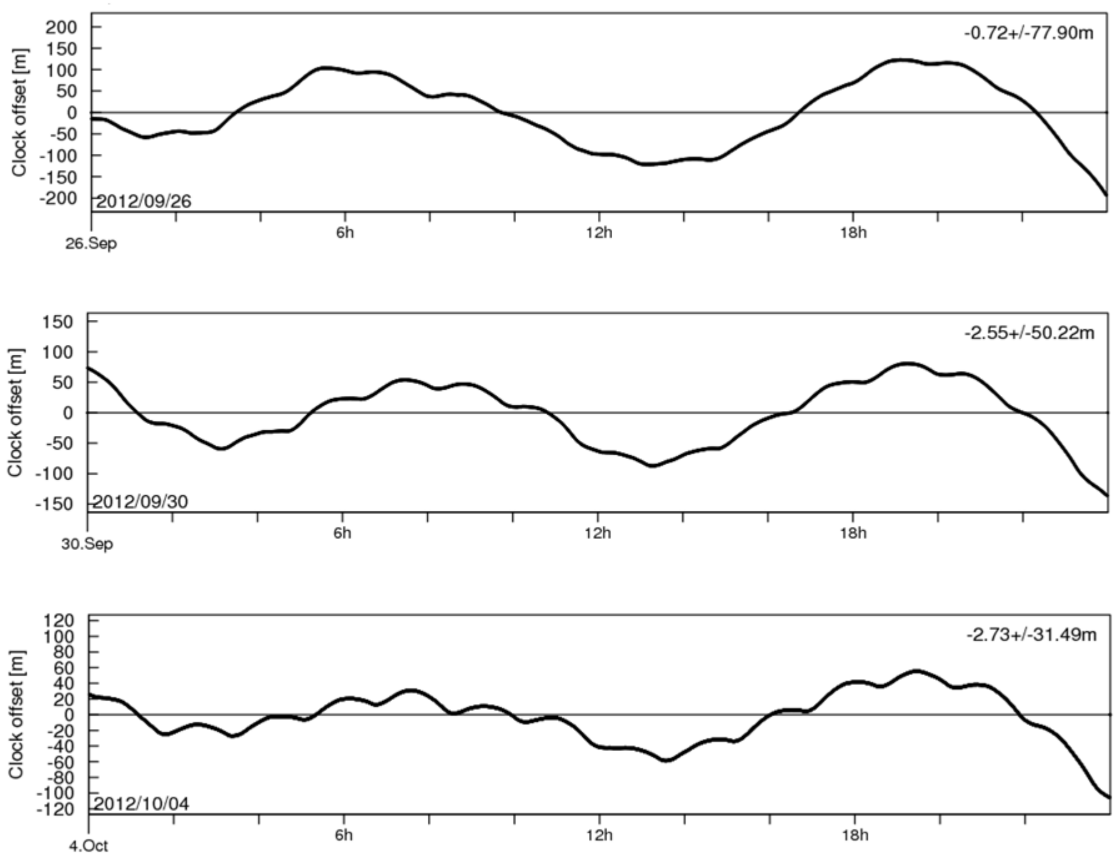


***Figure 9: Changes in the long-term temporal variation of Metop-B USO for three selected days of the first week of GRAS operation. The clock offset is corrected for a second-order polynomial.***

The dependency of the oscillator frequency on the external USO temperature is another key performance indicator. Using temperature data from the satellite's telemetry and the corresponding clock drift from the clock solution of the POD, the clock drift has been plotted over temperature for both Metop satellites using data of October 1, 2012 in Figure 10. It becomes obvious, that the variation of the clock drift is significantly larger for Metop-B. Furthermore, it becomes obvious that the external USO temperature of Metop-B is about 1.4 K lower compared to Metop-A. The red trend line in the plots indicates the changes in clock drift depending on temperature change. For Metop-A, the drift changes with 13.0 ps/s/K (or $1.3\cdot10^{-11}$/K), which is well below the specification of $5.0\cdot10^{-11}$/K. On the other hand, Metop-B with a drift changes of 51.2 ps/s/K (or $5.1\cdot10^{-11}$/K) barely meets this requirements.

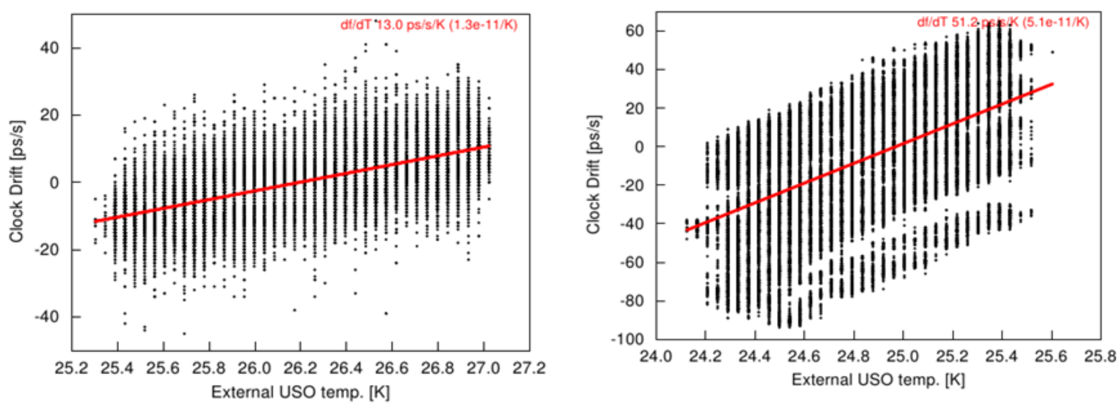


***Figure 10: Dependency of USO clock drift on external temperature for Metop-A (left plot) and Metop-B (right plot) for October 1, 2012.***

The difference in the USO performance becomes also visible in the plots of the Allan deviation in Figure 11. The Allen deviation has been computed based on the clock offsets from a 1 Hz POD solution for October 1 and October 3. It becomes obvious that the USO of Metop-A has virtually identical performance on both days. The USO of Metop-B exhibits identical Allan deviations up to averaging intervals of 3 seconds, but is less stable for longer intervals. This is an expected result considering the higher variation of the clock observed in the POD solution for Metop-B. It is also interesting to note that there is apparently a small improvement of the Allan deviation for the USO of Metop-B from October 1 to October 3.

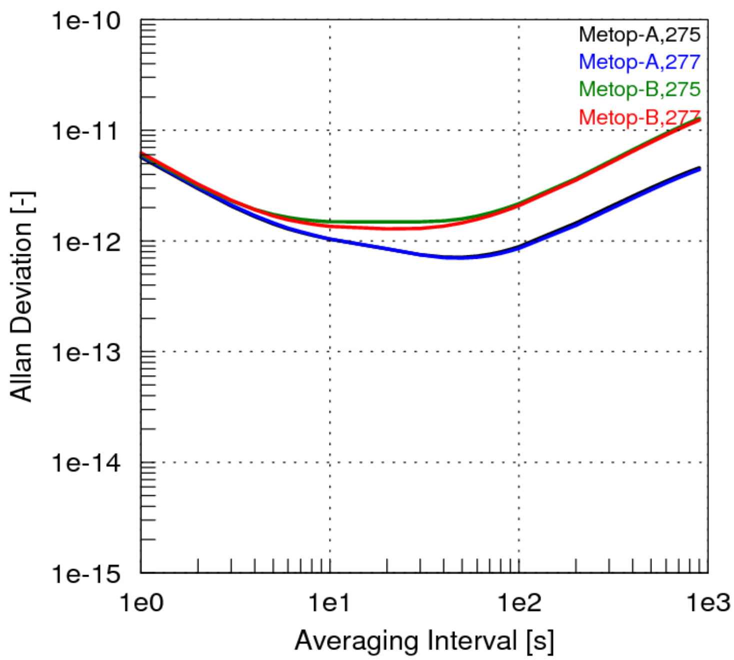


***Figure 11: Allan deviation for the USOs of Metop-A and Metop-B based on 1 Hz clock solutions from reduced-dynamic POD for October 1 and October 3, 2012.***

# 6 STATUS AND OUTLOOK OF RO APPLICATIONS

## 6.1 NWP Applications

GNSS-RO observations have a significant impact in operational NWP systems because they complement the information provided by satellite radiance measurements. This is primarily because they have superior vertical resolution to the radiances, and they can be assimilated without bias correction to the NWP model. This means they are “anchor measurements” and they constrain the bias corrections applied to radiance measurements.

Most operational NWP centres have reported a positive impact from GNSS-RO, particularly on upper-tropospheric and stratospheric temperatures (e.g., *Healy and Thépaut* [2006]; *Aparicio and Deblonde* [2008]; Cucurull and Derber [2008]; Poli et al. [2008]; *Cucurull* [2010]; *Rennie* [2010]; *Huang et al.*, [2010]; *Le Marshall et al.* [2010]; *Harnish et al.* [2013]). For example, Figure 12 shows the impact of the GNSS-RO measurements on the ECMWF short-range forecast biases in the stratosphere when they we first assimilated on December 12, 2006.

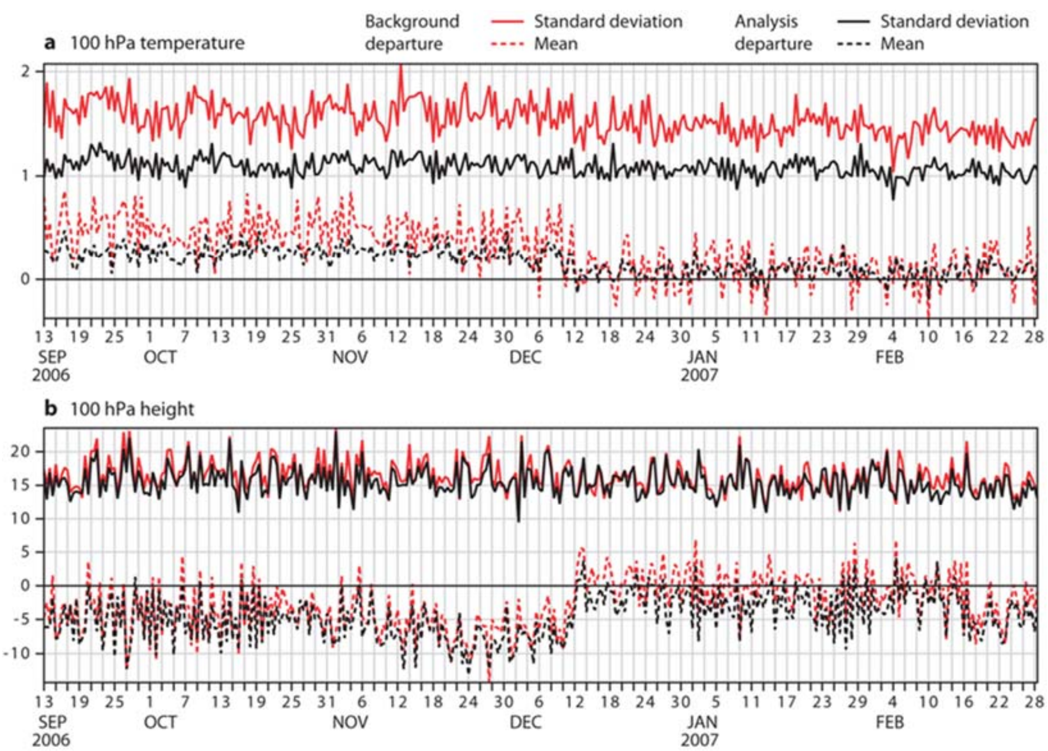


***Figure 12 Time series of the mean and standard deviation of the ECMWF operational background departures and analysis departures for (a) temperature and (b) geopotential height radiosonde measurements at 100 hPa in the southern hemisphere. GNSS-RO was introduced on December 12, 2006.***

A recent set of observing system experiments (OSEs) has been performed at ECMWF by Tony McNally. It has been shown that the largest GNSS-RO impact is on upper-tropospheric and lower/middle stratospheric temperature errors, which is consistent with the early 1D-Var information content studies. Although there is some evidence that the GNSS-RO measurements improve tropospheric water vapour, it appears that the GNSS-RO contribution to the water vapour analysis is small at this time, when compared to the other observing systems. This may be a result of data numbers.

Currently, GNSS-RO contributes around 3 % of the total number of measurements assimilated in the NWP system. Ensemble of Data Assimilation (EDA) computations, used to estimate how the GNSS-RO impact scales with observation number, support the case for a significant increase of measurements, to at least 15000-20000 profiles per day [*Harnisch et al.*, 2013]. In addition, it is hoped that improved forward modelling and data processing techniques will improve the impact in the troposphere.

A relatively new application currently being investigated at the Met Office and ECMWF is verifying short and medium-range stratospheric forecasts with GNSS-RO. Verifying stratospheric forecasts against radiosondes in the southern hemisphere is problematic because there are only around 40 sites. The use of GNSS-RO will circumvent this limitation of the radiosonde dataset.

It is also hoped that GNSS-RO level 3 datasets will become an increasingly useful tool for GCM (NWP and climate) developers, so that model changes can be tested against reliable GNSS-RO climatologies. This is likely to be most effective for the upper-tropospheric and lower/middle stratospheric temperatures. The ROM SAF bending angle and refractivity forward models have recently been introduced in the Met Office version of the COSP satellite simulation software tool for climate model assessment [*Bodas-Salcedo et al.,* 2011].

As an anchor measurement, GNSS-RO now has important applications for climate reanalyses. For example, recent work (Adrian Simmons, pers. Comm.) has shown that the JRA-55 and ERA-Interim reanalyses have produced more consistent stratospheric temperature analyses since the assimilation of COSMIC GNSS-RO measurements in both systems.

## 6.2 Planetary Boundary Layer Height

The planetary boundary layer bridges the gap between the Earth's surface and the free troposphere, and therefore plays a key role in the exchange of heat, moisture and momentum between them. Its characteristics, including, crucially, its depth, are therefore important parameters in developing the understanding of such exchanges that is needed to get the most out of process studies, parameterisations and climate monitoring [*Garratt*, 1993]. The shallow depth (~1-3 km), thinness of the top boundary (~10-100 m) and frequent presence of cloud and rain mean that routine, widely available, accurate and reliable planetary boundary layer height (PBLH) estimates have thus far eluded atmospheric scientists.

Radio Occultation measurements, on account of their high vertical resolution and relatively uniform spatial distribution over land and sea alike, have long been considered as possible measurements of PBLH. Numerous studies (e.g. [*Ratnam and Basha*, 2010; *Guo et al*, 2000; *Ao et al*, 2012]) have confirmed this potential.

PBLH estimates based on the location of maximum vertical gradients of various RO profile fields, including bending angle and refractivity, have been implemented in ROPP9.0. Example diagnosed PBLHs for an occultation sited over the S Pacific marine stratocumulus region are shown in Figure 13. (The consistency between the various measures is not always this good.)

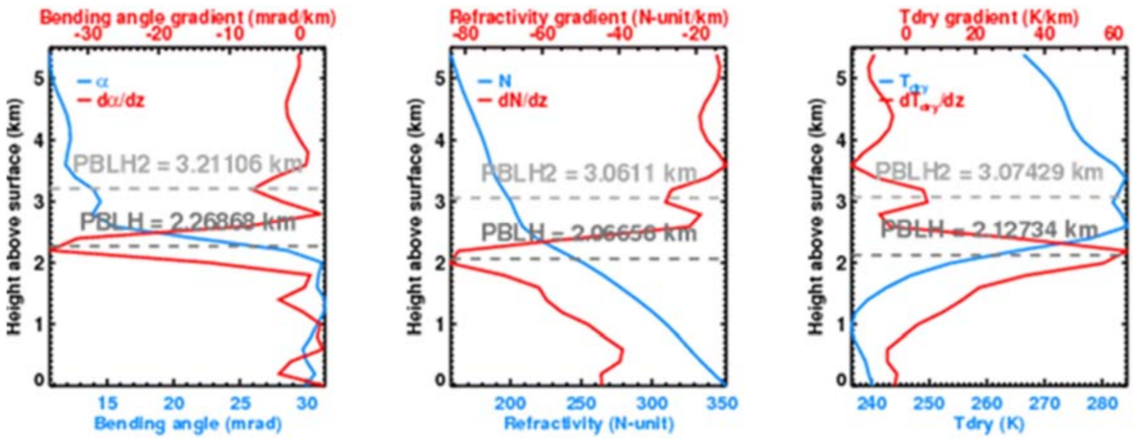


***Figure 13 PBLHs defined by bending angle, refractivity and dry temperature for an occultation situated over the marine stratocumulus region off the west coast of South America at (108W, 25S).***

A monthly average PBLH, as defined by the location of the maximum absolute value of the refractivity gradient, is shown in Figure 14.

Future work on the use of RO data to measure planetary boundary layer height could include:

- an investigation of the sensitivity of the various PBLHs to vertical resolution, spatial location, the rising or setting of the occultation, the processing of the RO data in the lower troposphere (GO or WO), the season, the year, and so on. This variability could guide the construction of uncertainties on the PBLHs — essential if, eventually, they are to be assimilated or used as reference dataset for model development;
- an examination of the PBLH sensitivity to horizontal gradient errors, including those in the ionosphere. Recent work [*Zeng et al.*, 2016] suggests impacts of up to 100 m;
- an assessment of the possible utility of these measures as climate data record, as soon as the sensitivities discussed above are understood better. It would be straightforward to generate dry temperatures, refractivities or bending angles from the climate model fields, and these could be directly compared to observationally derived PBLHs.

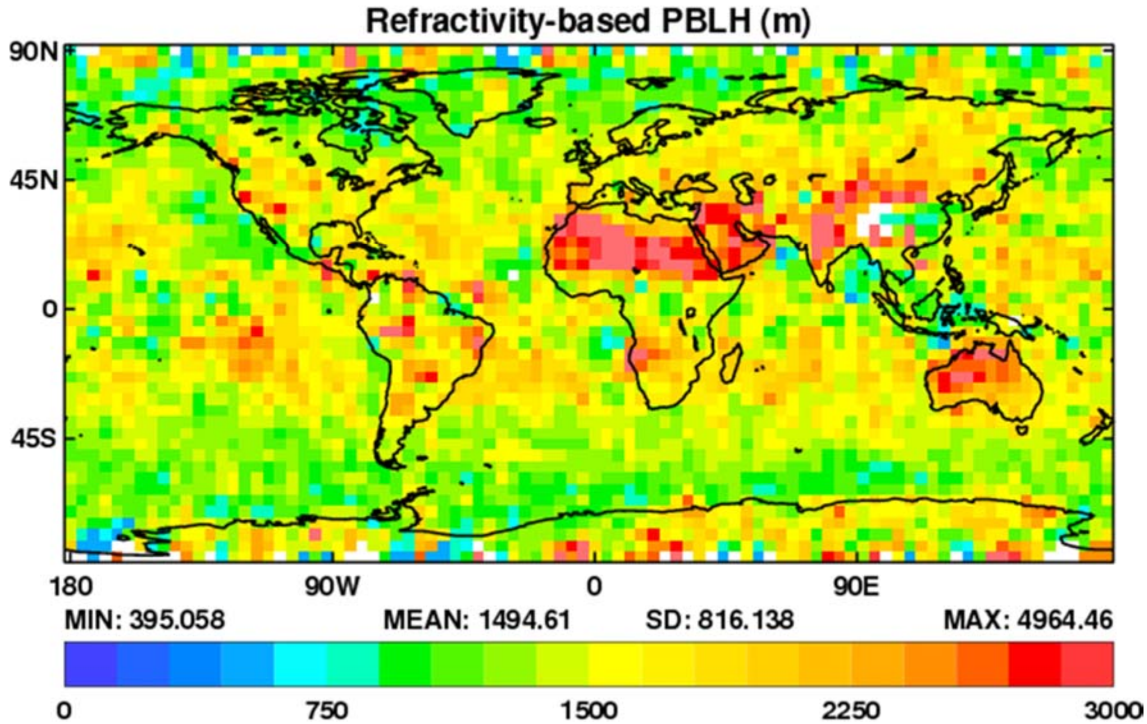


***Figure 14 Monthly mean refractivity-based PBLH, using all available occultations in April 2013.***

### 6.3 Tropopause Heights

Reanalyses and radiosonde observations during the last few decades have indicated an increase in the global mean tropopause height (TPH) [*Seidel and Randel*, 2006]. One possible reason for this is a warming of the troposphere (due to more $CO_2$) and a cooling of the lower stratosphere (due to less stratospheric ozone), both of which have been observed [*Randel et al.*, 2009].

*Lewis* [2009] introduced a new method for the identification of TPHs from GPS RO bending angles, based on the use of the covariance transform of the profile data. Using RO data since 2001, *Schmidt et al.* [2010] demonstrated an increase of the global tropopause height by about 70 m over the last decade, associated with a tropospheric warming and a lower stratospheric cooling. Tropopause issues can are dealt with in *Borsche et al.* [2007], *Foelsche et al.* [2009], *Rieckh et al.* [2014] *and Scherllin-Pirscher et al.* [2017].

The continuous monitoring of the tropopause height is therefore an important goal in atmospheric and climate research, and robust operational tools for its routine measurement are of great scientific value.

ROPP contains tools to diagnose tropopause height from RO bending angle, refractivity and dry temperature profiles, the latter being defined in terms of the lapse rate. An example (S. Atlantic, May 2009) is shown in Figure 15. The agreement between the first two and the two temperature-based TPHs is reasonable, although there is room for improvement.

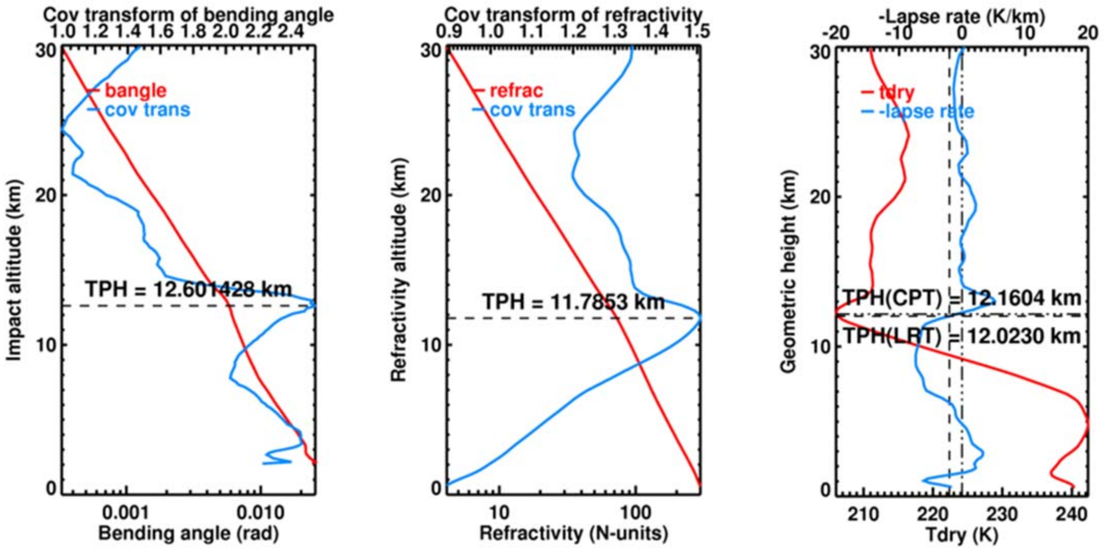


***Figure 15 TPHs defined by bending angle, refractivity and dry temperature for an occultation situated at (10W, 27S) on 1 May 2009.***

Figure 16 compares the zonal, monthly mean of the TPH derived from the lapse rate of the dry temperature (which is in fact the WMO definition of the tropopause height) calculated by ROPP and by different (but similar) algorithms at GFZ, on different datasets (all missions for ROPP, GRACE-A and TerraSAR-X for GFZ) covering the same month (April 2013). The agreement in general shape and in average value is encouraging.

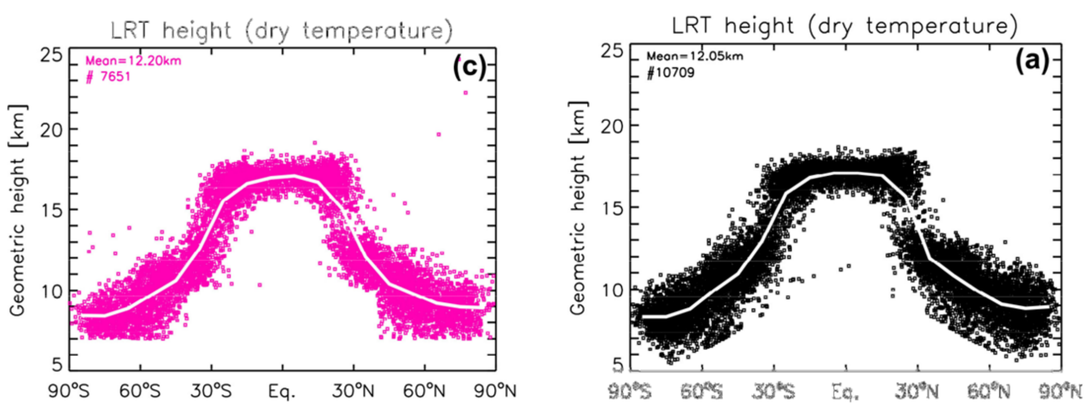


***Figure 16 Zonal and monthly (April 2013) mean dry temperature lapse-rate-based TPH, calculated by ROPP (left) and by GFZ (right) algorithms and data [Schmidt, 2013].***

Future work on the use of RO data to measure the tropopause height could include:

- an effort to understand, and then reduce, the difference between the various ROPP TPH measures;
- an attempt to identify the uncertainties in TPH estimates (necessary if TPH data are to be used as a reference for model development);

- their continued use in monitoring climate change.
- assist application of TPH products in various process studies. E.g. deep convection, Asian Monsoon, stratospheric composition, troposphere-stratosphere exchange.
- aid remote sensing of cirrus clouds.

## 6.4 Gravity Waves

Gravity waves (GWs) are buoyancy waves, traversing vertically and horizontally inside the atmosphere as perturbations in temperature and wind fields. Their vertical wavelengths range from below one to tens of kilometres, and their horizontal wavelengths ranges from a few to thousands of kilometres. At mid latitudes GWs are mainly emitted from strong wind fields passing mountain ranges (orographic waves) and from instability in the stratospheric jet stream, while in the tropics the main source of GWs is convection, [*Fritts*, 2003] and [*Khaykin*, 2015].

Numerous important atmospheric processes are controlled by gravity waves. Especially GWs ability to transport momentum has implications for the circulation. Examples are the stratospheric Quasi Biennial Oscillation which is driven by breaking gravity waves [*Lindzen*, 1968], the formation of the stratospheric polar vortex, [*Garcia*, 1994], and the summer hemisphere meridional transport [*Alexander*, 1996]. Gravity waves also play a role in triggering nucleation of polar stratospheric clouds and cirrus clouds [*Spichtinger*, 2005]. A brief introduction to physics of gravity waves and their role in atmospheric processes can be found in ROM SAF VS 29, *Khaykin* [2016], and references therein.

Since the l-short wavelength part of the gravity wave spectrum is not resolved by NWP and Climate models, GW representation in models is a challenge, and their parameterization has to be validated against measurements, [*Geller*, 2013].

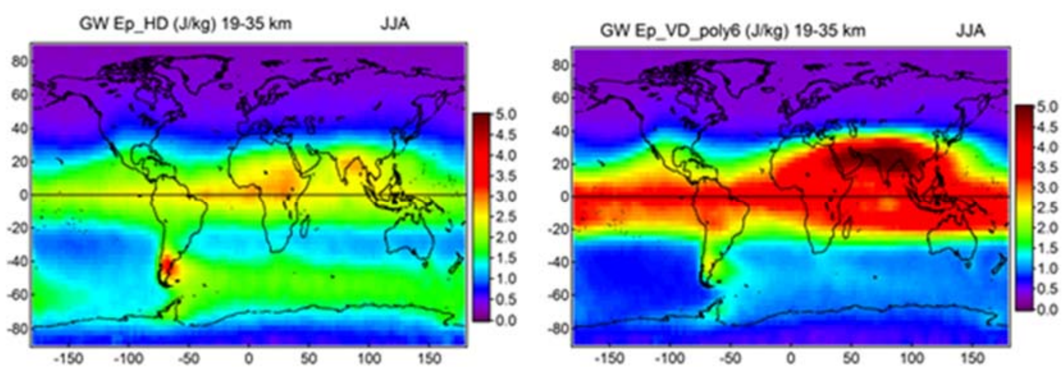


***Figure 17 From Khaykin [2016]: Example of gravity wave potential energy climatology from the ROM SAF CDR1 v 0.0 (June-August) based on dry temperature fluctuations. Left: Horizontal de-trending. Right: Vertical de-trending.***

Radio occultations provide a quite unique opportunity to access the global GW intensity. It is possible to extract the potential energy density from a single RO profile [*Tsuda*, 2000], [*Steiner*, 2000] and [*Šácha*, 2014]. Single profile methods rely on a reference profile needed to extract the fluctuations that can be attributed to wave activity. Figure 17 shows two such methods; "horizontal de-trending" (averaging over nearby profiles) and "vertical de-trending" (using a smoothed version of the actual profile). The single profile GW retrieval does not allow for an assessment of the momentum transported by the wave, which is in many applications the important parameter.

In Figure 18 the equatorial gravity wave potential energy density retrieved from RO is shown as an example. The zonal-mean potential energy density reveals a QBO signature. It is a two way process, the crossover between westerly and easterly winds in the stratosphere acts as barrier for vertical GW penetration, and the gravity waves delivers momentum pushing the crossover further downward.

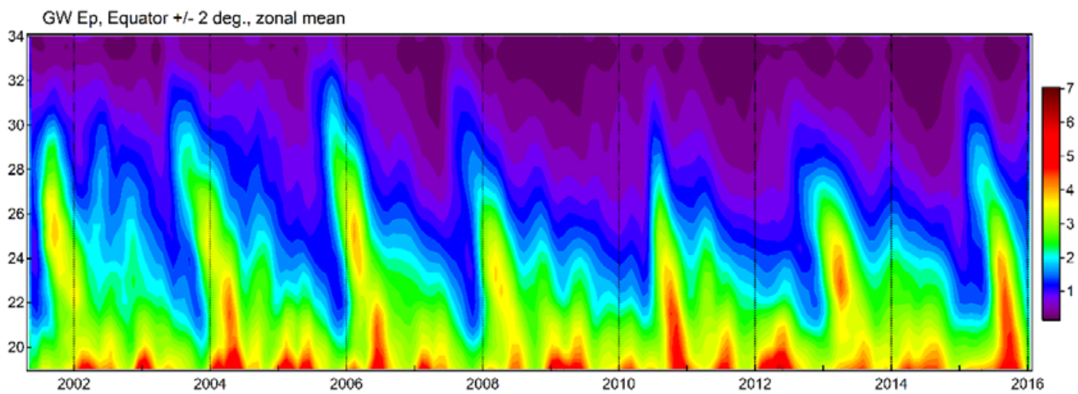


***Figure 18 From Khaykin [2016]: Time series of zonal-mean Ep7HD vertical distribution at the equator (+/- 2 deg.).***

Future work on the use of RO data to assess gravity wave activity could include:

- implementation of experimental offline gravity wave product for CDR/reprocessing, following recommendations of ROM SAF VS 29, [*Khaykin*, 2016];
- development of tomographic characterisation of gravity waves by multiple collocated RO incidents, with possibility of characterising momentum flux;
- approach climate community, provide datasets for model validation;
- assist in various science applications where gravity waves play a role. These can be local area as well as global studies.

## 6.5 Cloud Tops

Many studies have been conducted to determine the altitude of the storm cloud top using satellite instruments and different techniques [*Knibbe et al.*, 2000; *Koelemeijer et al.*, 2002; *Poole et al.*, 2002; *Platnick et al.*, 2003; *Minnis et al.*, 2008; *Chang et al.*, 2010; *Biondi et al.*, 2013], but the results strongly depend on the physical retrieval method and on the satellite data used [*Sherwood et al.*, 2004]. The use of GNSS RO during extreme convection and tropical cyclones has demonstrated the large capabilities of this technique improving the accuracy of cloud top altitude determination in comparison with other satellite measurements thanks to the very high vertical resolution, the global coverage and because the RO signal is unaffected by the weather conditions.

The so called "RO bending angle anomaly" technique applied for the first time by *Biondi et al*. [2011] uses the difference between the bending angle value during the study case, and the climatology in the same area for detecting the anomaly due to the presence of the extreme event itself (Figure 19). The extreme event creates an alteration of the regular atmospheric conditions and leaves a clear signature in the atmospheric structure [*Biondi et al.*, 2011; *Biondi et al.*, 2012a; *Biondi et al.*, 2013].

Comparison with independent measurements such as radiosondes [*Biondi et al.*, 2012b] and satellite based lidar [*Biondi et al.*, 2012b; *Biondi et al.*, 2013] has shown errors in the cloud top determination of about 300 m (Figure 20). *Biondi et al.* [2015] has also shown how the GNSS RO bending angle could be used for detecting and to map the overshooting tops generated by tropical cyclones. The overshooting are important features for understanding the atmospheric circulation and for aviation safety issues.

However this technique cannot be systematically applied at the moment due to the lack of operational satellites providing GNSS RO profiles with sufficient temporal resolution for monitoring extreme weather events.

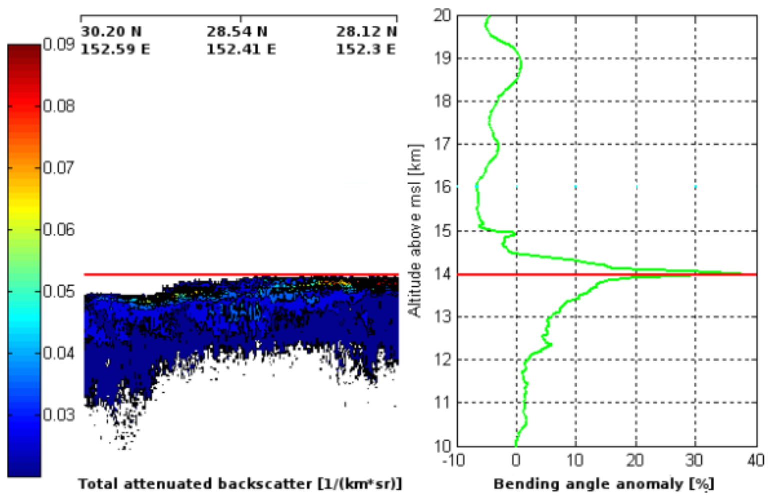


***Figure 19 Total attenuated backscatter (left) at 532 nm from CALIOP of a convective system the 14 April 2008, and the bending angle anomaly profile (right) corresponding the cloud top. The horizontal red line is the altitude of the cloud top corresponding to the bending angle anomaly spike [Biondi et al., 2012].***

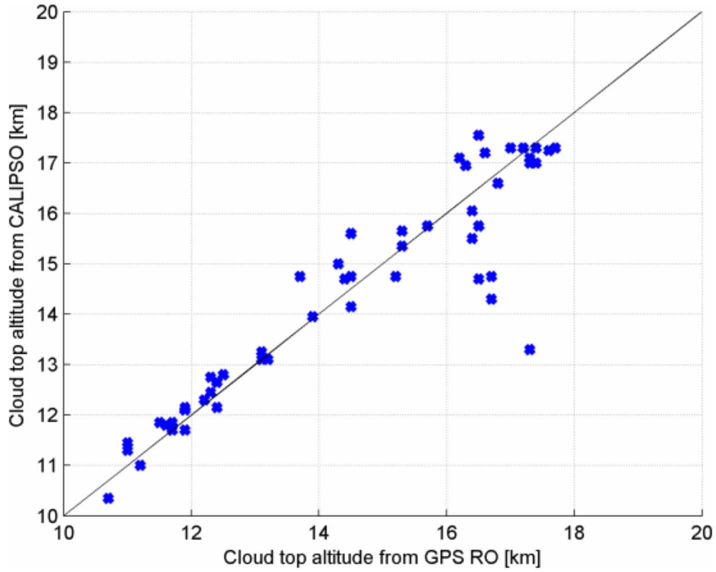


***Figure 20 Scatter plot showing correlation between cloud top heights derived from GPS RO and from CALIOP during a selected number of deep convective systems [Biondi et al., 2012].***

Another interesting application of the RO bending angle anomaly technique is the volcanic cloud top height detection. The determination of the volcanic cloud top altitude is still an open issue, *Tupper et al.* [2004] advocate the use of new techniques alongside the established ones to improve the ash cloud detection and monitoring and that "a reliable detection system cannot be dependent on the meteorological conditions and it is necessary to have a weather independent warning capacity".

The ESA-EUMETSAT workshop on Eyjafjöll eruption [*Zehner*, 2010] came up with recommendations including "Studies should be made of potential new satellites and instruments dedicated to monitoring volcanic ash plumes and eruptions" stating that "there is an urgent need to gather information on the vertical structure of evolving volcanic clouds". The GNSS RO are very well suited for such kind of studies and *Biondi et al.* [2017] have demonstrated how the bending angle can also be used for detecting the volcanic cloud top altitude (Figure 21) in combination with other measurements.

The capabilities of GNSS RO in this field are very broad and would allow a complete understanding of the volcanic cloud thickness in case a large number of profiles would be available during the eruptions.

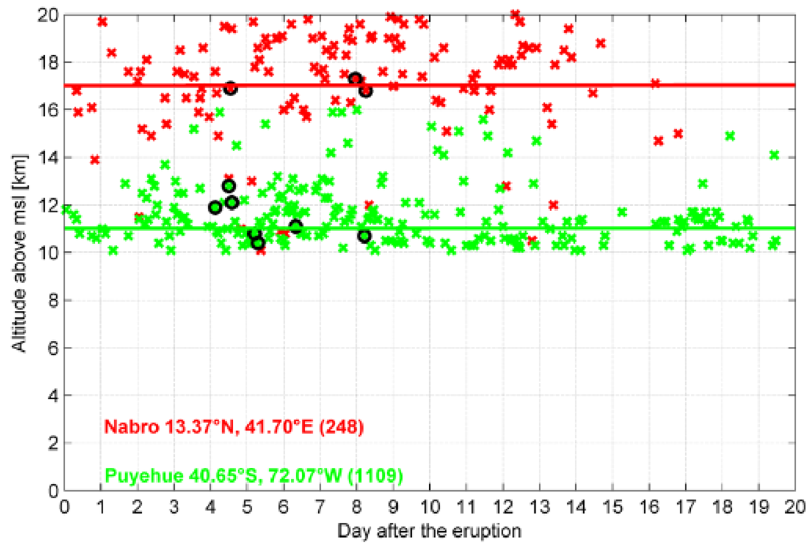


***Figure 21 Cloud top altitudes of volcanic plumes (cross symbols) for Puyehue (green) and Nabro (red), derived from RO data over the first 20 days from the eruption; co-located CALIOP data are indicated (black circles). Numbers in brackets denote the number of RO profiles while the horizontal solid lines denote the respective monthly climatological tropopause altitudes for the two volcano locations [Biondi et al., 2017].***

A complete study of cloud tops (weather or volcanic clouds) and systematic algorithms require the availability of a higher number of GNSS RO profiles, and the unique characteristics of RO (high vertical resolution, independency on weather conditions, availability in remote areas) would contribute to solve several issues not solvable with other instruments.

# 7 ATMOSPHERIC RO DATA PROCESSING AND PRODUCTS

## 7.1 Processing of Atmosphere Products

A RO instrument onboard a low-Earth orbit (LEO) satellite, e.g. the GRAS instrument onboard Metop, measures the L1 and L2 Doppler shifted radio signals from a GNSS satellite as the satellite sets or rises behind the Earth's limb. Through a complex sequence of processing steps the Doppler shift as a function of time is converted to neutral-atmosphere profiles of bending angle, refractivity, dry pressure and dry temperature, and finally to 1D-Var pressure, temperature, and humidity [*Kursinski et al.*, 1997; *Anthes,* 2011]. The latter quantities require a priori information taken from an atmospheric model [*Healy and Eyre,* 2000]. A priori data are also used for bending angle high-altitude initialization in order to retrieve refractivity [*Gobiet and Kirchengast,* 2001].

The level 3 gridded monthly mean data are derived through averaging and gridding of level 1 and 2 profile data. The aim of the climate processing algorithms is to generate homogeneous CDRs meeting the requirements set by various climate applications (see Chapter 9 where climate applications of RO data are discussed). The Level 3 data are e.g. provided as zonally gridded monthly means on a relatively coarse latitude-height grid. The processing from Level 1B, 2A and 2B profile data to Level 3 gridded data includes quality screening and data rejection, binning and area-weighted averaging, sampling-error correction through sampling of an atmospheric model, and estimation of uncertainties in the averages [*A. Steiner et al.*, 2013; *B. Ho et al.*, 2012].

The following sections provide a brief description of common steps involved in the processing of RO data to atmosphere products. Table 9 shows radio occultation atmosphere product groups together with the level definitions used by EUMETSAT and ESA.

***Table 9. Atmosphere product groups***

| **Product group** | **Main characteristics** |
|---|---|
| Level 1B bending angle | Bending angle as function of impact parameter |
| Level 2A refractivity | Vertical profile |
| Level 2A dry temperature | Vertical profile |
| Level 2B and 2C "1D-Var"<br><br>temperature, specific humidity, pressure, and surface pressure | 1D-Var vertical profiles, scalar at surface |
| Level 3 gridded data | Gridded and averaged data |

The fundamental observable measured by an RO instrument is the phase and amplitude of the Doppler-shifted incoming signal. The processing of the measured quantities leads to retrieved atmospheric profiles of geophysical variables [*Kursinski et al.*, 1997].[1] From phase and amplitude measurements, and the satellite's positions and velocities, we obtain the observed

[1] The ROPP User Guide [ROPPUG] gives a detailed description of the algorithms used in the ROM SAF processing.

bending angles as a function of impact parameter at the GNSS frequencies. The bending angle retrieval is performed separately for the GNSS signals typically using the standard geometric optics (GO) approach above some fixed height (e.g. 25 km) and using the so-called wave optics (WO) retrieval below that height [*Gorbunov,* 2000*; Jensen et al.,* 2003; *Gorbunov and Lauritsen*, 2004].

The wave optics algorithm performs a global mapping of the incoming wave signal to the (effective) impact parameter space where the impact parameter can be demonstrated to uniquely define a given ray under the assumption of local mirror symmetry. Under atmospheric conditions where this assumption is not fulfilled, the WO optics mapping will typically lead to a correct retrieval as long as the strength of horizontal gradients is not too strong.

The influence of the ionosphere can be removed to first order by forming a linear combination of the two L1 and L2 bending angles, $\alpha_{L1}$ and $\alpha_{L2}$, thus obtaining the observed (LC) bending angle $\alpha_{obs}$. This observed bending angle is contaminated with noise that increases exponentially with altitude rendering it useless above a certain height. However, we need bending angles to infinite altitudes in order to obtain the refractivity.

The solution is to form a statistically optimal linear combination of the observed bending angle, $\alpha_{obs}$, and a background bending angle, $\alpha_{bg}$, where the relative contributions of observation and background (or *a priori* data) are determined by the errors $\sigma_{bg}$ and $\sigma_{obs}$ (the latter is an estimate of the error in the observed LC bending angle) [*Gobiet and Kirchengast,* 2004]. The error models are chosen such that the fraction goes from no background at low altitudes to no observational information at high altitudes. The ionospheric correction and the statistical optimization steps may be combined into a single framework [*Gorbunov,* 2002].

### 7.1.1 Level 2A Refractivity Profiles and Dry Temperature Profiles

Bending angle is related to the vertical gradient of the refractive index *n*. The relation can be inverted using the inverse Abel transform to give the refractive index as a function of height from knowledge of the bending angles as a function of impact parameter [*Kursinski et al*., 1997]. The refractive index is expressed in terms of the refractivity, defined as

$$N \equiv (n-1)\cdot 10^6 \;, \qquad (1)$$

which can be regarded as an ordinary physical state variable since it is a function of other state variables. In the RO community it is common practice to use the following two-term expression

$$N = \kappa_1 \frac{p}{T} + \kappa_2 \frac{p_w}{T^2} \;, \qquad (2)$$

where $p$ is total pressure, $p_w$ is the partial pressure of water vapour, $\kappa_1$ is 77.6 K/hPa, and $\kappa_2$ is $3.73\cdot10^5$ $K^2$/hPa [*Kursinski et al*., 1997].

When humidity is negligible, the second term on the right hand side in Eq. (2) vanishes and the refractivity is directly proportional to the air density. Using the equation of state for an ideal gas and assuming hydrostatic equilibrium, the dry pressure profile is obtained by integrating a version of the hydrostatic equation from an upper boundary where the pressure is assumed to be known. Dry temperature is then computed from the dry pressure and the observed refractivity (using Eq. (2) with the "wet" term ignored).

### 7.1.2 Level 2B 1D-Var Products—Temperature, Humidity, Pressure Profiles

In the troposphere the influence from water vapour on the observed refractivity is not negligible. We thus have a temperature-humidity ambiguity which can only be resolved by introducing additional data on temperature and humidity. This is typically done through a 1D variational (1D-Var) procedure in which the observed refractivity profile (or bending angle) is combined with a model profile in a statistically optimal way considering the errors and vertical error correlations of both the observations and the *a priori* data [*Healy and Eyre,* 2000]. A solution is found by minimizing the cost function,

$$J(\mathbf{x}) = \frac{1}{2}(\mathbf{x}-\mathbf{x}^{\mathrm{b}})^{\mathrm{T}}\mathbf{B}^{-1}(\mathbf{x}-\mathbf{x}^{\mathrm{b}}) + \frac{1}{2}(\mathbf{y}^{\mathrm{o}}-\mathbf{H}(\mathbf{x}))^{\mathrm{T}}\mathbf{O}^{-1}(\mathbf{y}^{\mathrm{o}}-\mathbf{H}(\mathbf{x})) \ , \qquad (3)$$

with respect to the atmospheric state $\boldsymbol{x}$. **H** is the forward operator mapping the atmospheric state $\boldsymbol{x}$ (temperature, pressure, humidity) into measurement space (refractivity), and **O** and **B** are the observation and background error covariance matrixes, respectively. The *a priori* state $\boldsymbol{x}^{\mathrm{b}}$ is typically obtained from a global NWP model.[2]

### 7.1.3 Level 3 Gridded Data—Monthly Climatological Data Records

The profile data (Level 1B, 2A, and 2B) are processed into Level 3 gridded data consisting of, e.g., zonal monthly means on a 5 degrees by 200 meters latitude-height grid. The Level 3 processing is based on a rather straight-forward binning and averaging procedure (see, e.g., *Gobiet et al.* [2005]; *Borsche et al.* [2007]; *Foelsche et al.* [2008]; *Ho et al.* [2009b]; *Gleisner* [2010]).[3] A set of equal-angle latitudinal bands, or grid boxes, are defined and all quality-controlled observations that fall within a latitude band and calendar month undergo a weighted averaging to form an area-weighted zonal mean for that latitude and month. The quality screening is essential to remove erroneous outliers that otherwise could have a significant impact on the statistics [*Steiner et al.*, 2013a; *Ho et al.*, 2012].

The monthly means obtained through this procedure are affected by errors due to under-sampling of the atmospheric variability. This includes under-sampling of the diurnal cycle (*Pirscher et al.* [2007]). A part of these sampling errors are systematic, causing biases, rather than random errors, in the monthly means. Using an atmospheric model that has a realistic variability (e.g. the ECMWF operational analyses, or ERA Interim reanalyses), an estimate of the sampling errors can be found by sampling at the same locations and times as the actual observations (see also Chapter 9). The estimated sampling errors are subtracted from the

[2] The background state used in the ROM SAF 1D-Var processing is interpolated from the ECMWF 6-hour forecasts given on a 1.0˚x1.0˚ degree grid.[ROPP1DV]

[3] The description of the algorithms used in the ROM SAF climate processing is given in [ROPPL3G].

observed means, leaving the much smaller *residual sampling errors*, which combine with the statistical *measurement errors* to form the total errors (or, more correctly, uncertainties) in the monthly means (e.g., *Scherllin-Pirscher et al*. [2011b; 2017]).

In summary, the RO climate data products are generated by the following steps:

- listing of all occultations that were observed within a calendar month;
- flagging invalid profiles according to a set of quality criteria;
- vertical interpolation of profiles onto the regular climate height grid;
- weighted averaging into monthly latitude bins;
- estimation of the errors in the zonal monthly means;
- estimation of the a priori information in the zonal monthly means;
- formatting of the RO climate data and meta-data into appropriate data files.

The generation of zonal monthly mean climate data may be followed by further averaging into seasonal and annual means, and into regional, hemispheric, and global means (e.g., *Lackner et al.* [2011a]; *Ao et al.* [2015]; *Gleisner et al.* [2015]; *Steiner et al*. [2016b]).

# 8 IONOSPHERIC RO DATA PROCESSING AND PRODUCTS

## 8.1 Retrieval of Profiles and related Quantities from Ionospheric Occultations

The most relevant ionosphere-related product that could be delivered from EPS-SG occultation data are the vertical profiles of electron density up to 500km, and its realistic extrapolation with recent developed techniques. These profiles could be computed using the techniques proposed during the execution of the ROPE project[4]: Least Mean Square-based Abel inversion with improved topside modelling and using Separability Hypothesis (see *Garcia-Fernandez et al.* [2003]). The vertical resolution of such profiles might be between 2 to 4km for a sampling rate of 1Hz in the occultation data, using the Linear Mean Square approach (see *Garcia-Fernandez and Hernandez-Pajares* [2016]).

### 8.1.1 Ne Profiling and hmF2 NmF2 hmE NmE Metrics

One of the possibilities offered by inverted profiles of electron densities is the provision of key profile parameters such as the height and maximum of ionospheric layers (see Figure 22). In particular:

1. **hmF2**, Height of the F2 layer peak;
2. **NmF2**, Electron density of the F2 layer peak;
3. **hmE**, Height of the E layer local peak (when available);
4. **NmE**, Electron density of the E layer local peak (when available);
5. **Sporadic E prediction**. Based on high rate (50Hz) occultation data, the detection of sporadic E layer would be more reliable. This would in turn allow to maintain a database of historic sporadic E occurrence. The long term analysis of such historic data would then allow to predict the occurrence of this phenomena.

Obtaining such parameters is, essentially, a process as simple as to obtain the local maxima of the profile. The historical values of such parameters could be then made available in a similar fashion as done by the SPIDR web service[5] [*Zhizhin et al.* 2008].

[4] ROPE Project, under EUMETSAT contract EUM CO 15 4600001591 AVE
[5] http://spidr.ionosonde.net/spidr/

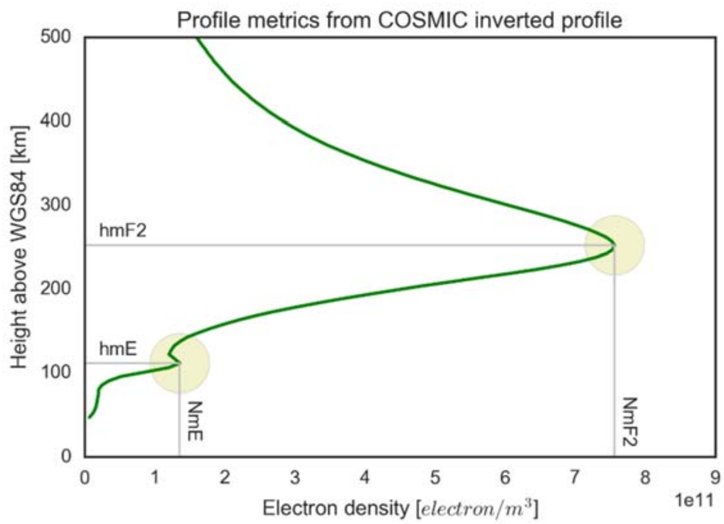


***Figure 22 Example of a set of profile metrics extracted from a COSMIC occultation.***

The errors of the parameters in the F2 layer (compared to values obtained from ionosondes) obtained from occultation data amount to ca. 10% to 20% in the case of electron density and ca. 25km to 50km in the case of the height estimation (see *Garcia-Fernandez et al* [2003]). The values at the E layer are expected to be higher due to the accumulation of errors in the inversion process (in particular for the electron density).

Additionally to these raw values of the profile, other parameters of interest such as the M(3000)F2 value could be derived. This value represents the highest frequency that can be received (by ionosphere refractivity) at 3000km and is usually derived from ionograms. Actually, when using ionosonde data, the hmF2 is estimated using expressions such as the Dudeney formula or similar (see *MacNamara* [2008] and references therein), which tie both magnitudes. In case the profiles of electron density are available through inversion of occultation data, all parameters needed to compute the M(3000)F2 are available.

### 8.1.2 Topside VTEC Estimation

Topside VTEC maps (> 800 km) can be built using the POD antenna measurements. A two voxel layer model (in a forward+backward Kalman filter) to estimate the VTEC can be used in order to avoid the need of an a-priori mapping function (such as the standard one which is not applicable anyway above the hmF2). This provides information on the topside as well as from the plasmasphere that can be later used as a background model to refine the ionospheric occultation inversion.

As an example, the results for COSMIC POD data obtained during day 264 of year 2011 are summarized in Figure 23 where the distribution of electron content estimates in first and second layer are shown (shells centred at 1130 km and 1810 km respectively, with a horizontal voxel dimension of $12^o \times 10^o$ in right ascension and declination/latitude).

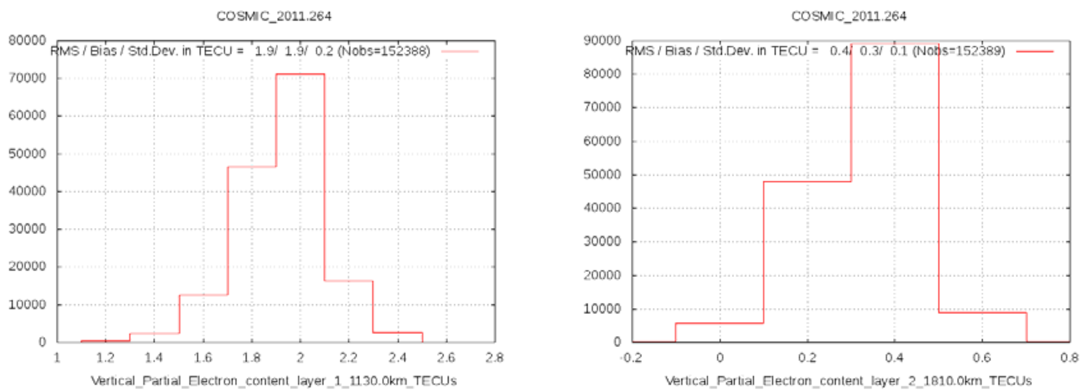


***Figure 23 Distribution of COSMIC/FORMOSAT-3 topside electron content estimates, first and second shells of voxels, respectively shown at left and right hand sides, during day 264, 2011.***

Two snapshots of the corresponding final estimations can be found in Figure 23, where a smooth distribution which highest values (of few TECUs and tenths of TECUs for first and second layer respectively) are distributed around the Sun position (right ascension of about 178$^{o}$ and latitude of 1$^{o}$ approximately). Moreover the associated plasmaspheric scale heights are distributed with values in between 565 km and 1118 km, in agreement with the values derived from topside ionospheric sounders (see *Marinov et al.* [2015], in corresponding comparing with top plot in Figure 3 in this paper).

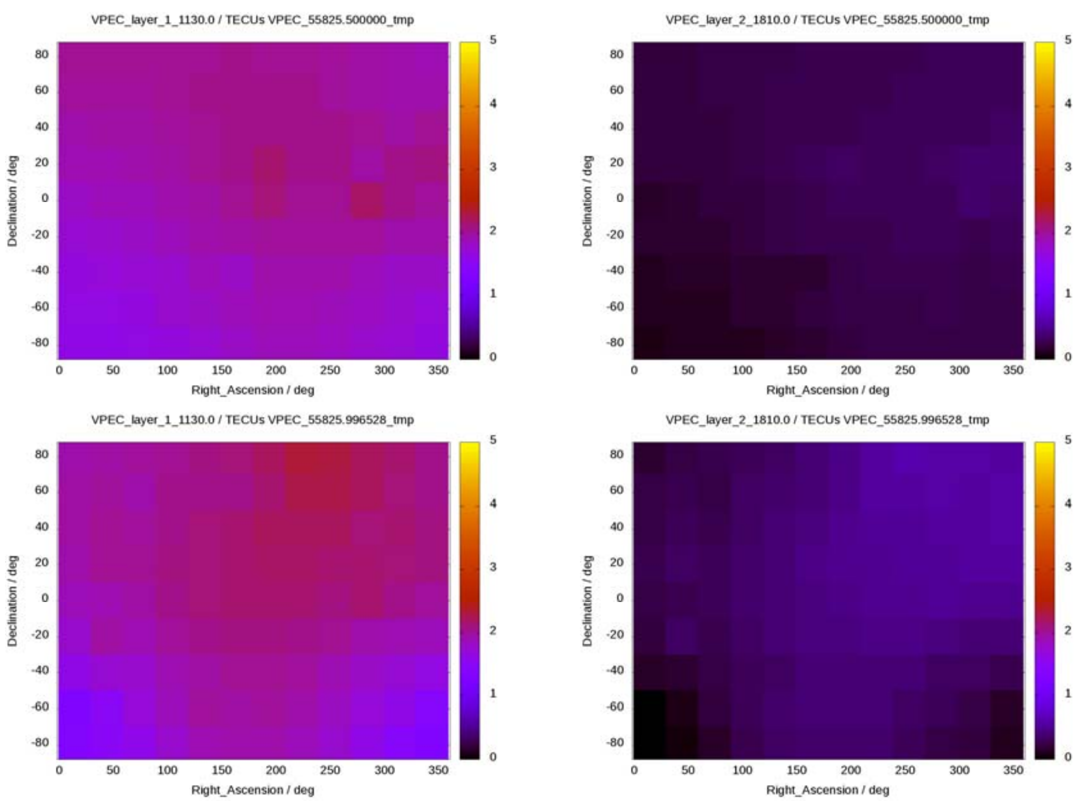

***Figure 24 Topside electron content estimates derived from COSMIC/FORMOSAT-3 POD antenna measurements, first and second shells of voxels respectively shown at left and right hand sides, during day 264, 2011 at 12:00 (top row) and 23:55 (bottom row) GPS time.***

### 8.1.3 Profile Initialization

As a direct and mainly intended application, the calibration of the STEC from radio-occultation measurements could be performed using the dual-layer tomographic estimations of the plasmasphere, after smoothing it with a low degree polynomial. This smoothing is needed to remove the discontinuities of the derivative, associated to the grid tomographic estimation, from the ionospheric delay correction above the LEO (see Figure 24).

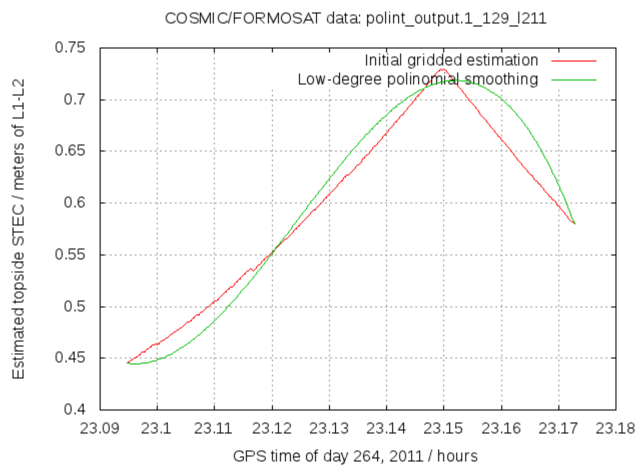


***Figure 25 Example of topside slant electron content correction for COSMIC occultation during day 264. Note that the correction has been smoothed in order to remove the voxel discretization of the tomographic algorithm.***

Finally an example of the impact of the application of such LEO topside slant electron content corrections can be seen in Figure 25. Indeed, an improvement on bottomside electron density profile (removing negativity) after applying the dual-layer tomographic plasmaspheric correction (autonomously computed from POD COSMIC measurements) is shown.

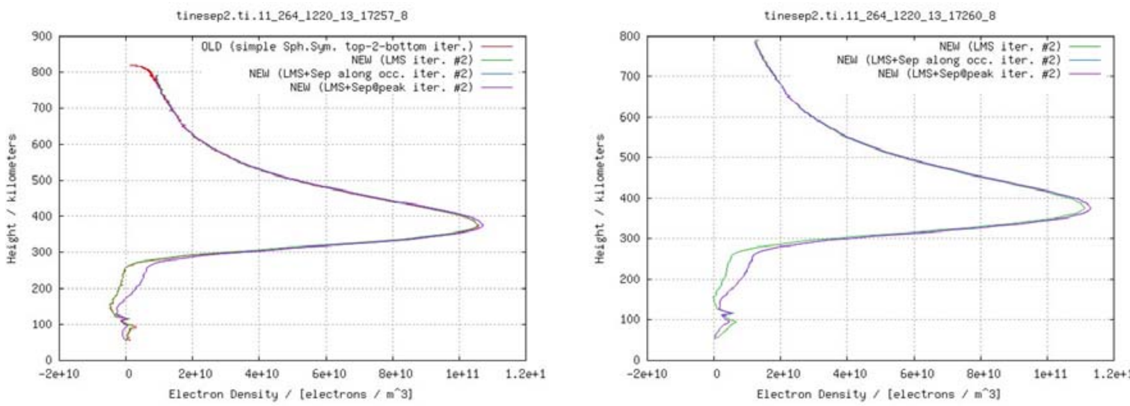


***Figure 26 Electron density profile, inverted from the COSMIC/FORMOSAT-3 radio-occultation measurements before (left) and after (right) applying the POD-antenna measurements based plasmaspheric electron content estimation (day 264, 2011).***

### 8.1.4 Bending Angles Estimation

Additional side products that could be delivered are the bending angles of the ionospheric refractivity at each frequency (i.e. L1 and L5) using the classical Abel inversion approach (see *Aragon-Angel et al.* [2011]). Despite the fact that these products typically require precise orbits and clocks (i.e. no combinations that remove the geometry can be used to obtain the ionospheric information in undifference processing), the knowledge of the bending at each frequency (proportional to the electron density) can provide valuable information on the ionospheric state. In particular to the estimation of higher order ionospheric effects such as the difference in STEC due to the different curved paths of each frequency (see e.g. Section 5.2 of *Petrie et al.* [2011]).

### 8.1.5 Lower Layers of the Ionosphere

When obtaining vertical profiles of electron density using the Abel inversion (or its *peel onion* implementation with or without separability hypothesis), one of the main problems is the treatment of lower layers. Due to the fact that this technique is a top-to-bottom processing, the errors accumulate specially in the lower layers of the profile (E and D layers). This is evidenced when comparing vertical profiles from Radio Occultations (RO) with (spatially and temporally) co-located scaled ionograms (see Figure 26). In those plots, the COSMIC profiles at the E and D layers have a higher electron density compared with their ionosonde counterparts.

RO and ionosonde profiles are complementary in that RO profiles provide a more realistic topside estimation, while ionosonde profiles (requiring a bottom-to-top inversion) offer, in general, a better estimation in the lower layers but require a model beyond the F2 layer (i.e. there is no observations in the valleys of Ne and beyond hmF 2). This is also evidenced in Figure 26, where the topside between the two techniques differs substantially.

During the execution of the ROPE project, several modifications on the peel onion approach to invert occultation data into electron density profile have been tested and implemented.

These modifications are the Linear Root Mean Square to jointly estimate the profile with constraints as well as the correcting the topside content beyond the height of the LEO satellite. These upgrades improve a bit the estimation of the lower layers due to the overall reduction in error, especially when compared with the equivalent profile computed using the spherical symmetry assumption. However, there is still some room for improvement regarding the E and D layers.

In order to provide with a potential realistic measure of the error in both the F2 and E layer height and density estimations, a routine comparison with ionosonde data could be performed in the future (and in particular during the operations of the EPS-SG mission). Due to the vast amount of ionosondes and ionosonde data available today (see Figure 28), a quality metric such as the one herewith proposed could be readily computed.

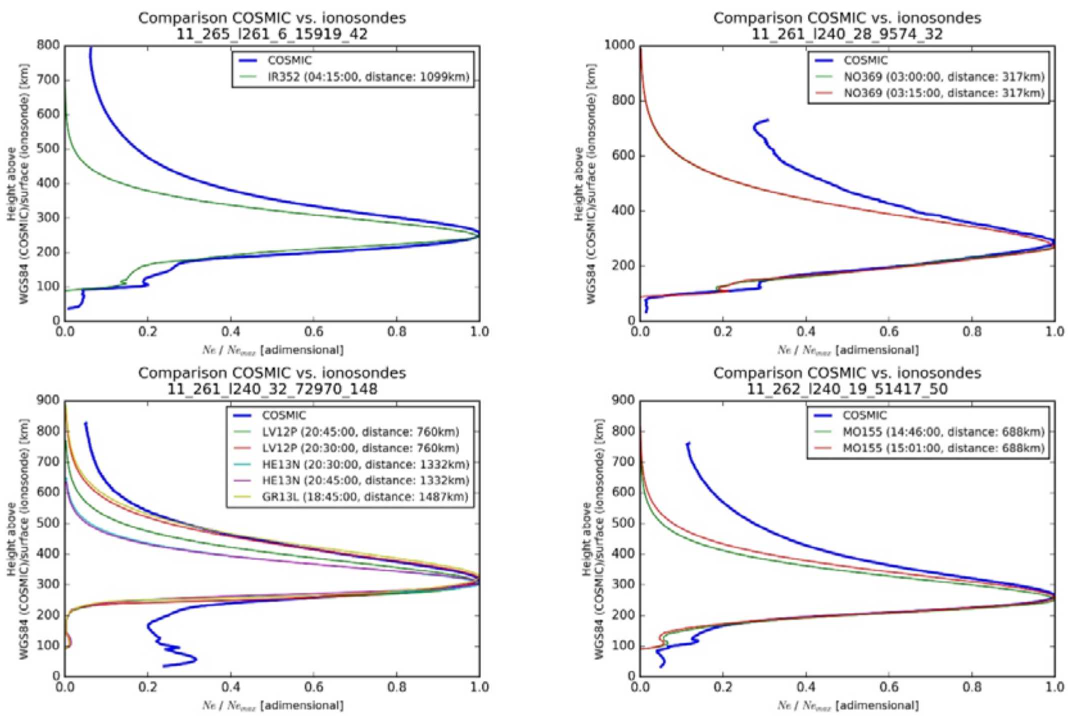


***Figure 27 Examples of comparisons between inverted occultations obtained with COSMIC satellites and spatially and temporal collocated ionosondes.***

Automatically and manually scaled ionograms can be fetched at the following url path (using UNIX date format specifiers[6]):

```
https://www.ngdc.noaa.gov/ionosonde/data/<staid>/ ...
        individual/%Y/043/scaled/<staid>_%Y%j%H%M%S.SAO
```

where `<staid>` refers to the station name. An example of such path for the Ebre station in Spain (EB040) for February 12th 2016 (day of year 043) would be the following:

[6] https://docs.python.org/2/library/datetime.html#strftime-and-strptime-behavior

```
https://www.ngdc.noaa.gov/ionosonde/data/EB040/ ...
        individual/2016/043/scaled/EB040_2016043000002.SAO
```

This cross-comparison task would require, however, developing a data editing process (in some cases manual scaling) due to the fact that the ionograms can show uncertainties that lead to inaccurate profiles (see for instance *Buresova et al.* [2007]).


***Figure 28 Map of the global ionosonde network. Source of the station list courtesy of NOAA.***

One of the main problems when retrieving electron density profiles using GNSS RO data is that the errors accumulate at lower heights. This is usually evident when comparing electron density profiles obtained with RO data against profiles from ionosondes properly calibrated.

Calibration of Ne profiles using manually scaled spatial- and temporal collocated ionograms could be performed to overcome this limitation close to the available ionosonde facilities.

## 8.2 Monitoring Scintillations with RO Observations
### 8.2.1 Scintillation Indices from RO Observations

The computation and interpretation of the scintillation indices might entail some complexities due to factors such as the strong variation in geometry and latitude (and associated magnetic field effect), and various phenomenology at the lower layers of the ionosphere.

Some computation of the S4 index could be focused at the upper layers of the ionosphere, where the effects are localized and the geometry is less variable than in lower heights. And in this way the different scintillation phenomenology between equatorial regions (with predominant amplitude scintillation) and high latitude areas (with predominant phase scintillation) might be better distinguished. This computation could be based on the algorithm proposed for the FORMOSAT-3/COSMIC constellation[7].

[7] http://cdaac-www.cosmic.ucar.edu/cdaac/doc/documents/s4_description.pdf

### 8.2.2 Scintillations to deduce Irregularities/Instabilities from RO Observations

The propagation through inhomogeneities in the spatial distribution of the refractive index can originate scattering of radio signals. In the ionosphere, spatial variations of the refractive index are caused by irregularities in the electron density spatial distribution. In the presence of relative motion between transmitter, receiver and propagation medium, the scattering originates temporal fluctuations in the signal amplitude and phase, which are known as radio wave scintillation [*Yeh and Liu*, 1982].

The scattering can be weak or strong, depending on the electron density fluctuations relative to the background medium, the size of the irregularities, the distance between irregularities and transmitter/receiver, and the carrier frequency of the radio signal [*Ishimaru*, 1978; *Coleman*, 2016].

Irregularities in the electron density spatial distribution are formed as a consequence of plasma instabilities that can modify background equilibrium under the effect of changes in electric field, magnetic fields, and currents. Instability mechanisms appear different between the equatorial, auroral and polar ionosphere, owing to different electrodynamics conditions [*Kelley*, 2009; *Forte et al.*, 2016]. Ground and in-situ observations alone have limitations in resolving to the spatial and temporal variability of the irregularities and, as a consequence, the instability mechanisms responsible for their formation.

RO measurements can be utilised to complement in-situ and ground observations in order to advance the understanding in:

- instability mechanisms operating in the equatorial, auroral, and polar ionosphere;
- the scales of irregularities forming in the equatorial, auroral, and polar ionosphere;
- the modelling of plasma instability mechanisms in the equatorial, auroral, and polar ionosphere;
- the ionospheric response to given space weather events;
- the modelling of different scattering regimes in trans-ionospheric propagation.

RO measurements can help investigating on these aspects. In particular, the new RO instrument is well suited to support these studies in view of the following:

- closed and open loop measurements in parallel up to 500 km;
- sampling rate 200-250 Hz;
- GPS and Galileo measurements.

Both in high and low latitudes ionospheres, the bulk of irregularities extends between 100 km and 600 km on average (with plumes of ionisation reaching 1000 km at low latitudes). Assuming diffractive scattering of GNSS signals under a phase screen approximation, the typical Fresnel frequency [*Yeh and Liu*, 1982] of the observations can be in excess of 100 Hz (at L1), making the new instrument suitable to capture the nature of plasma irregularities (and associated instabilities) in future.

### 8.2.3 Effects on Receiver Hardware and Observables, and Countermeasures

Radio wave scintillation arising from the propagation through ionospheric irregularities can affect the performance of GNSS receivers in several ways. Scintillation-induced effects can be present on space-borne receivers utilised for example in RO missions.

Scintillation effects can be summarised as follows [*Skone and De Jong*, 2001; *Skone et al.*, 2000; *Morton et al.*, 2013]:

- Weak-to-moderate scintillation - increase of higher-order errors in the estimate of observables (e.g. carrier phases); these errors are not frequency-scalable and do not necessarily cancel out from combination of phases observations at various carriers. The magnitude of these errors relative to oscillator and thermal noise depends on the amount of scattering and on the propagation conditions (i.e. whether low or high latitudes)
- Moderate-to-strong scintillation – increase in the occurrence of losses of lock and cycle slips following strong scattering, typically arising when propagation is along field-aligned irregularities. Losses of lock can reduce the number of measurements available.
- Strong scintillation – presence of non-linearity in the receiver logics, which introduces errors in the estimate of carrier phases in the presence of strong/saturating scintillation.

RO measurements can be utilised in conjunction with theoretical and simulation studies in order to advance the understanding of scintillation effects on the receiver performance as well as to characterise the accuracy of the measurements carried out.

## 8.3 Assimilation of RO Ionospheric Observations into Ionospheric Models

Data assimilation (DA) models aim to optimally combine disparate measurements with a background model. DA methods are well established in meteorology and a wide range of techniques have been developed; i.e. weighted least squares (WLS) [*Plackett*, 1950], Kalman filters [*Kalman*, 1960; *Houtekamer and Mitchell*, 2005], Optimal Interpolation (OI) [*Gandin*, 1963; *Eddy*, 1967] and variational methods [*Le Dimet and Talagrand*, 1986]. DA is much less well developed in the ionospheric domain; however, it has emerged over the last 15 years, driven largely by the availability of large scale ground based GNSS receiver networks (i.e. the International GNSS Service, IGS [*Beutler et al.*, 1999]).

Ionospheric data assimilation models include the Multi-Instrument Data Analysis System (MIDAS) [*Mitchell and Spencer*, 2003; *Spencer and Mitchell*, 2007], the Electron Density Assimilative Model (EDAM) [*Angling and Jackson-Booth*, 2011], GPS Ionospheric Inversion (GPSII) [*Fridman et al.*, 2009], the Texas Reconfigurable Ionosphere Plasmasphere Logarithmic Data Assimilator (TRIPL-DA) [*Gaussiran et al.*, 2011] and TOMION [*Hernández-Pajares et al.*, 1999]. Other data assimilation models, which use physics models for their background include the Utah State University Global Assimilation of Ionospheric Measurements (USU-GAIM) Model [*Scherliess et al.*, 2011] and the Jet Propulsion Laboratory's Global Assimilative Ionospheric Model (GAIM) [*Mandrake et al.*, 2005]. A review of ionospheric data assimilation models can be found in *Bust and Mitchell* [2008].

A variety of approaches have been taken to assimilate ionospheric radio occultation data: *Angling* [2008] and *Komjathy et al*. [2010] both assimilated RO TEC (derived from COSMIC) and ground based TEC (into EDAM and JPL-GAIM respectively) to assess the impact of the RO data. Similarly, [*Lin et al.*, 2015] have assimilated RO TEC using a Kalman Filter, but have examined the impact of non-stationary background model error covariances. *Lee et al.* [2012] used the NCAR Data Assimilation Research Testbed (DART) to implement an ensemble Kalman filter with which to assimilate RO data into a coupled thermosphere/ionosphere model (TIE-GCM).

Most studies of ionospheric RO DA have focussed on the F region. However, *Nicolls et al.* [2009] describe an approach to extract E region profiles by first modelling and removing the F region gradients using IDA3D. IDA3D is a 3DVAR based DA model [*Bust et al.*, 2004] which has also been used with COSMIC data to image the ionosphere during geomagnetic storms [*Bust*, 2006].

Given the DA research that has been conducted with previous RO instruments, the EPS-SG science plan for RO data assimilation should focus on addressing fundamental questions that will have applicability across the wide range of DA techniques employed in ionospheric research:

- Choice of measurements to assimilate;
- Characterisation of the measurement errors;
- Development of an observation operators.

### 8.3.1 Assimilation of Abel Transform Products with External Data

It is likely that processing centres will continue to produce standard Abel Transform inversions of electron density. Although such data has known problems related to the inherent assumptions in the inversions, the data may still be able to add value to DA schemes in conjunction with other data sources. Therefore, the ability of Abel Transform RO to augment other data types (ground based TEC, ionosondes, etc.) should be assessed. In particular, the contribution of data from EPS-SG should be considered in light of the other upcoming RO constellations (COSMIC2, etc.).

### 8.3.2 Assimilation of Augmented Abel Transform Products

Similarly to the standard Abel Transform inversions, augmented Abel Transform results should also be assessed as potential inputs to DA models. These studies will provide baseline results against which further improvements, using more advances methods, can be measured.

### 8.3.3 Assimilation of TEC Measurements

Due to the dispersive nature of the ionosphere, phase measurements at two frequencies can be used to derive a line of sight total electron content (TEC) [*Garner et al.*, 2008]. The TEC can conveniently be assimilated using a 3D observation operator in a manner analogous to the use of ground based slant TEC. However, the choice of how to derive TEC (i.e. which phase/pseudorange combination to use) affects the error characteristics of the measurement. This was discussed by *Syndergaard* [2002] but little work has been done to investigate the impact on a DA scheme. Furthermore, the magnitude of the TEC is generally dominated by the F region and thus assimilating TEC can be insensitive to variations in the E region and E/F valley. As stated previously, *Nicolls et al.* [2009] used a two-step approach to mitigate this. However, other methods should be investigated.

#### 8.3.4 Assimilation of Bending Angle Measurements

An alternative assimilation method is to ingest products based on the measured Doppler shift of the GNSS signals. For neutral atmosphere models this is usually done by estimating the bending angle and assimilating that. The conversion to bending angle relies on the assumption of spherical symmetry; however, the bending angle is sensitive to vertical gradients in the electron density, so may provide a better way to capture information about the bottom side structure the ionosphere. Initially a 1D bending angle operator can be used. However, experience from DA in the neutral atmosphere has shown the benefit of 2D bending angle operators [*Healy et al.*, 2007] and these should also be developed and assessed.

#### 8.3.5 Development of Combined Neutral Atmosphere/Ionosphere Assimilation

Ionospheric DA is unaffected by the neutral atmosphere since the rays to not penetrate low enough in the atmosphere. Further, neutral atmosphere DA generally uses a correction to the bending angles to remove the effects of the ionosphere [*Vorob'ev and Krasil'nikova*, 1994; *Healy and Culverwell*, 2015]. Consequently the neutral atmosphere and ionospheric DA is conducted independently. However, as the community moves towards whole atmosphere models it would be useful to consider the possibility of assimilating neutral and ionospheric data consistently in the same DA scheme.

### 8.4 Model Assessment and Validation using RO-derived Data

This activity would consider the possibility to assess and validate ionospheric electron density models using RO-derived products.

As an example, the International Reference Ionosphere (IRI) [*Bilitza*, 2014] and the NeQuick 2 [*Nava et al.*, 2008] could be considered. They are climatological models since they describe the median behaviour of the ionosphere. Nevertheless, they can also provide weather-like description of the ionosphere using suitable data ingestion procedures (e.g. [*Nava et al.,* 2011; *Shaikh et al.*, 2017]) or they can be used as background models in more sophisticated data assimilation schemes [*Lin et al.*, 2015; *Minkwitz et al.*, 2016].

These models compute the (vertical) electron density profiles on the basis of anchor points related to peak parameters like foF2 and the propagation factor M(3000)F2, or values like hmF2. Therefore, as a first extent, they could be evaluated in terms of electron density profiles (including data like NmF2, hmF2, M(3000)F2) by comparison with the corresponding RO-derived quantities, taking into account the relevant accuracies.

Subsequently, TEC data could be considered for complementary analyses. Occultation links can be used to study the lowest part of the topside ionosphere, while POD-derived TEC can be taken into account for plasmaspheric studies. In this context, the work by Zhang et al. [2016] can be mentioned as the authors have compared the topside ionospheric and plasmaspheric electron content (TPEC) of IRI-plas model [*Gulyaeva et al.*, 2012] with the corresponding COSMIC-derived TPEC data, during low and high solar activity periods.

## 8.5 Improvement of Empirical Models using RO-derived Data (Bruno, ICTP)

An activity devoted to possible improvements of empirical models on the bases of GNSS RO-derived data is envisaged. Particular attention would be devoted to the shape of the models' electron density profile above the F2 peak height. The NeQuick model could be considered as an example since it is not always able to perfectly reproduce the experimental ionospheric slab thickness [*Nava et al.,* 2011]. Therefore the ideas expressed e.g. by *Liu et al.* [2008] or *Olivares-Pulido et al.* [2016] could be adopted to extract the (topside) scale height information and utilize it to modify the NeQuick topside formulation (given by a semi-Epstein layer with a height-dependent thickness parameter).

In addition, following *Haralambous and Oikonomou* [2013], specific RO-derived topside electron density profiles matching the F2 peak values, as measured by a co-located ionosonde, could be used as reference. In this case, the electron density model could be forced to match the ionospheric peak characteristics at the ionosonde/RO-profile location in order to estimate the topside electron density profiles over the area of interest. From the differences between the model-retrieved and the corresponding RO-derived topside electron density profiles, indications about how to modify the model topside scale height parameterization could be obtained.

# 9 CLIMATE USE OF RO DATA

Observations for climate monitoring and change detection have to meet stringent quality criteria as stated by the Global Climate Observing System (GCOS) Program on climate monitoring principles for satellite observations and the generation of satellite-based Climate Data Records (CDRs) of Essential Climate Variables (ECVs) [*GCOS*, 2006; 2010a,b; 2011]. A Fundamental Climate Data Record (FCDR) is defined as a long-term record involving a series of instruments with sufficient calibration and quality control for the generation of homogeneous products, accurate and stable enough for climate monitoring [*GCOS*, 2010a].

Main requirements are long-term stability and traceability to standards of the international system of units (SI) since separate data sets from different platforms must be directly comparable to give reliable long-term records [*Ohring*, 2007]. FCDRs for generation of the ECV upper-air temperature are typically calibrated passive microwave and infrared radiances. For RO measurements, bending angles are considered FCDRs. Furthermore, the term Thematic Climate Data Record (TCDR) denotes long-term series of ECVs that are *derived* from FCDRs, such as RO atmospheric temperature or RO refractivity [*GCOS*, 2011].

The accuracy requirement for climate observations is much more stringent than for weather observations (e.g., 0.1 K vs 1 K) [*Trenberth et al*., 2013]. Uncertainty must be smaller than the signals expected from decadal change [*Ohring et al*., 2005; *Bojinski et al*., 2014]. GCOS target requirements for ECV upper air temperature as specified for temperature profiles in the troposphere to the stratosphere are a horizontal resolution of 25 km to 100 km, a vertical resolution of 1 km to 2 km, an accuracy of 0.5 K, and a stability of 0.05 K [*GCOS*, 2011].

## 9.1 Quality of RO Data for Climate Use

### 9.1.1 RO Data Characteristics for Climate

RO provides a data record of high quality for monitoring the Earth's atmosphere and climate. Observations are provided in near all-weather conditions with global coverage and high accuracy (temperature <1 K) and vertical resolution (~1 km) in the UTLS [*Kursinski et al*., 1997]. Precise time measurements guarantee SI-traceability [*Leroy et al*. 2006a], long-term measurement stability and consistency, and is a characteristic of a climate benchmark record. Thus, consistently processed data from different RO missions are can be combined without any inter-calibration to a seamless climate record [*Foelsche et al*., 2011; *Steiner et al*., 2016], shown in Figure 29 for the Wegener Center OPSv5.6 record [*Angerer et al.*, 2017]. A detailed description on the unique characteristics of RO is given by *Anthes et al*. [2011] and by *Steiner et al*. [2011] with focus on climate.

The continuity and global coverage of GNSS RO observations is essential to ensure a continuous long-term CDR. *GCOS* [2011] identified RO as key component for the GCOS and stated that a continuation of the record must be ensured. The number of occultation observations per day depends on the number of transmitters and receivers and it increases with the availability of GNSS and LEO satellites. Global coverage is given if the receiving satellite is in a near-polar orbit. Current and future Metop satellite series only cover certain local times. However, RO observations from multiple satellites are used to establish CDRs for climate monitoring. In any case, the sampling has to be taken into account if atmospheric variability in space and time is not fully captured by the discrete sampling of RO.

While large-scale climate monitoring can be successfully tackled with current occultation observations, the study and improved understanding of many regional-scale and large-scale climate processes critically depends on diurnal-cycle and meso-scale resolution. For reference, a monthly mean record utilizing the effective horizontal resolution of about 300 km with a 6-hour resolution of the diurnal cycle requires at least 20,000 occultations per day as is stated as a main recommendation of the International RO Working Group (IROWG) [*IROWG*, 2015].

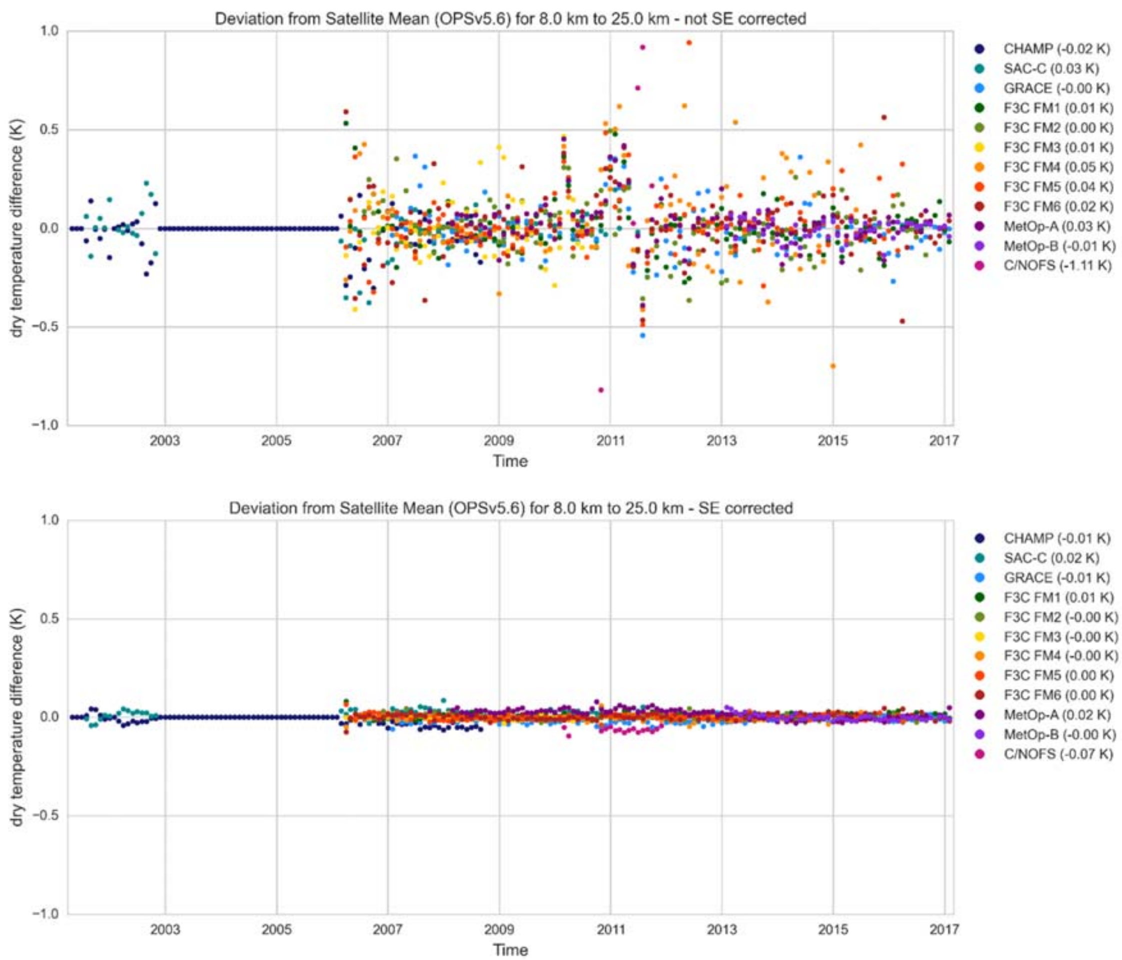


***Figure 29 Consistency of RO data from different satellites. Shown are deviations of individual satellites from the multi-satellite mean for monthly mean dry temperature in the altitude layer 8–25 km, without sampling error (SE) correction (a) and with SE correction applied (b). The satellite mean is calculated from all missions available for the respective month (before May 2006 only CHAMP and SAC-C delivered data) [Angerer et al., 2017].***

### 9.1.2 Uncertainty Characterization of RO Climatologies

Precise knowledge of errors is an important prerequisite for the utilization of data in climate studies. Empirical error estimates [*Kuo et al*., 2004; *Steiner and Kirchengast*, 2005; *Steiner et al*., 2006] are available for the observational error of RO atmospheric profiles and described by a simple model accounting for latitudinal and seasonal dependencies [*Scherllin-Pirscher et al.*, 2011a]. The observational uncertainty of individual RO profiles in the tropopause region is about 0.8% for bending angle, 0.35% for refractivity, 0.15% for pressure, and 0.7 K for temperature and gradually increases into the stratosphere.

For RO-based climatological fields the total error budget includes statistical (observational) error, (residual) sampling error, and systematic error [*Scherllin-Pirscher et al.*, 2011b; 2016a]. The statistical error in climatologies becomes negligible (<0.01 K to 0.1 K) due to averaging over hundreds of individual profiles per zonal band. The sampling error can reasonably be estimated using reference data, which adequately represent actual spatial and temporal atmospheric variability [*Foelsche et al.*, 2008a; 2009].

The typical average temperature sampling error for single-satellite (CHAMP) monthly-mean 10°-zonal means is <0.3 K in the upper troposphere-lower stratosphere (UTLS), with the local time component being <0.15 K [*Pirscher et al.*, 2007]. Subtracting the sampling error from mean climatological fields leaves a residual sampling error. It is generally less than 30% of the original sampling error amounting to <0.1 K for vertically resolved and to <0.03 K for UTLS large-scale means.

The total climatological error of mean atmospheric fields is, in general, dominated by the systematic error component related to potential residual biases in measurements and in the retrieval process, except at high latitudes, where the residual sampling error can dominate. Reflecting current knowledge of systematic error sources, up-to-date-best guesses of systematic error bounds are about 0.1 K in temperature. The total climatological error in monthly 10° zonal means was estimated to be smaller than 0.15 K in temperature in the UTLS, increasing to 0.6 K towards higher latitudes in wintertime, respectively. Overall the errors of RO climatological fields are small compared to any other UTLS observing system for thermodynamic atmospheric variables.

### 9.1.3 Structural Uncertainty of RO Climate Records from Different Data Centres

Of essential importance for climate use is the knowledge of structural uncertainty in the RO record arising from different processing schemes. Therefore, the RO Trends Intercomparison Working Group (‘ROTrends group’) was established (http://irowg.org/projects/rotrends/), an international collaboration of RO processing centres: Danish Meteorological Institute (DMI)/ROM-SAF, Copenhagen, Denmark; German Research Centre for Geosciences (GFZ), Potsdam, Germany; EUMETSAT, Darmstadt, Germany (EUM); Jet Propulsion Laboratory (JPL) Pasadena, CA, USA; University Corporation for Atmospheric Research (UCAR) Boulder, CO, USA; and Wegener Center/University of Graz (WEGC), Graz, Austria.

The focus of joint studies by the ROTrends group is on intercomparisons of RO multi-year data records for a systematic assessment of accuracy and data quality. The aim is to validate RO as a climate benchmark by demonstrating that trends in RO products are essentially independent of retrieval centre [*IROWG*, 2012].

Intercomparisons were performed for the multi-year CHAMP record. Structural uncertainty was quantified based on RO data provided by the different processing centres for bending angle to dry temperature. Profile-to-profile intercomparisons [*Ho et al.*, 2009b; 2012] were based on exactly the same set of profiles from each data centre. Complementary, RO gridded climate records based on the full set of profiles provided by each centre were averaged to monthly and zonal-mean climatological fields and the sampling error subtracted [*Steiner et al.*, 2013a].

The results for gridded climate records were found consistent with those for individual profiles, indicating that residual sampling error is small to negligible over regions with a lower atmospheric variability. Although the derived variables including bending angle, refractivity, pressure, geopotential height, and temperature are not readily traceable to SI units of time, the high precision nature of the raw RO observables is preserved in the inversion chain, demonstrating the usefulness of all these RO derived variables.

The structural uncertainty (Figure 30) was found lowest within 50°S to 50°N at 8 km to 25 km for all inspected RO variables. In this region, the structural uncertainty in trends over 7 years is <0.03% for bending angle, refractivity, pressure, and <0.06 K for temperature. Structural uncertainty increases above 25 km and at high latitudes, mainly due to different bending angle initialization in the centres' processing schemes.

The results demonstrate that GPS RO meets the GCOS climate requirements for ECVs in low-to-mid-latitudes below 25 km for air temperature. Though currently the use of RO for reliable climate trend assessment is bound to 50°S to 50°N, quality is favourable in the UTLS for climate [*Steiner et al.*, 2013a]. However, further processing advancements are needed and ongoing towards improved initialization, error characterization, and integrated uncertainty estimation [*Kirchengast et al.*, 2016].

The ROTrends activity is meanwhile integrated in the project RO-CLIM (http://www.scope-cm.org/projects/scm-08/) of the interagency initiative SCOPE-CM (Sustained and COordinated Processing of Environmental satellite data for Climate Monitoring; www.scope-cm.org). Advanced intercomparison studies are currently ongoing assessing the structural uncertainty of the 15-year *multi-satellite* RO records 2001-2016 from different processing centres [*Steiner et al.*, 2016]. The main aim of the RO-CLIM project and the contributing centres is to enhance the maturity of RO data [*Bates and Privette*, 2012] and the generation of RO based climate data records (CDR) at the quality standards of the GCOS climate monitoring principles.

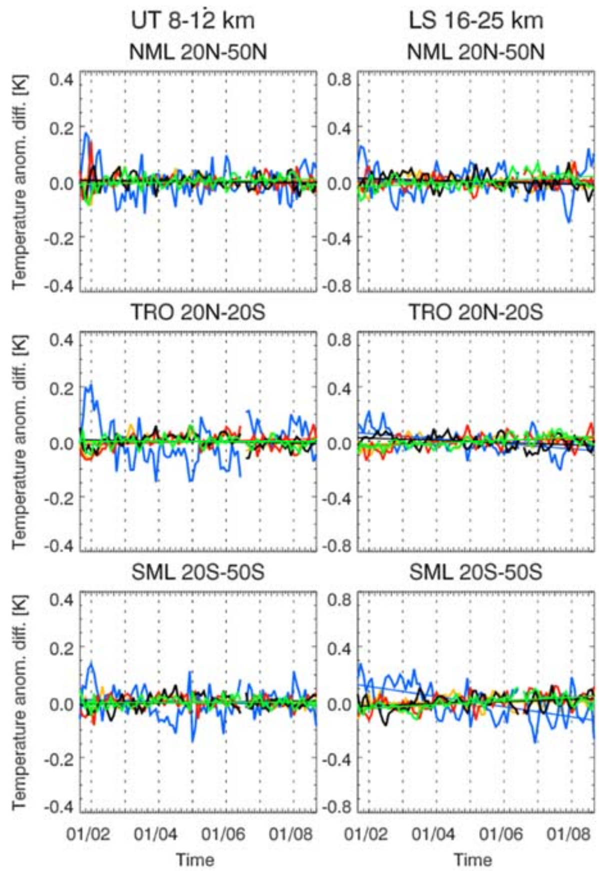


***Figure 30 Structural uncertainty in the CHAMP RO dry temperature record from different processing centres: DMI Copenhagen (yellow), GFZ Potsdam (blue), JPL Pasadena (red), UCAR Boulder (black), and WEGC (green). Difference time series of temperature anomalies are shown for each centre with respect to the all-centre mean for the upper troposphere (left) and the lower stratosphere (right), for northern mid-latitudes, the tropics, and southern mid-latitudes (top to bottom) [Steiner et al., 2013].***

## 9.2 RO Use for Monitoring Atmospheric Variability and Detecting Changes

The capability of RO for climate change monitoring has been tested in a series of studies from observing system simulation experiments to the exploration of climate change indicators and the detection of trends in real RO observations.

*Yuan et al*. [1993] were the first to suggest using RO for trend detection. They simulated the propagation of GPS signals in a climate model with doubled carbon dioxide concentration and found an increase in the signal phase path. *Melbourne et al*. [1994] and *Ware et al*. [1996] discussed that more precise and consistent measurements like RO could enable shorter time periods for identifying climate trends.

This was demonstrated by *Leroy and North* [2000] and *Leroy et al*. [2006b] using RO simulations for climate model. Detection time was shown to depend on correlation time of natural variability and on satellite lifetime and increases with measurement uncertainty

[*Leroy et al*., 2008]. *Ringer and Healy* [2008] demonstrated the utility of RO bending angle profiles for climate trend detection, with detection times of 10 to 16 years.

Regarding key climate RO variables, *Leroy* [1997] discussed geopotential height at constant pressure levels as useful parameter for monitoring climate change. Refractivity was discussed by *Vedel and Stendel* [2003] and *Stendel et al*. [2006]. *Leroy et al*. [2006b] proposed refractivity as function of geopotential height to be used as the more natural independent vertical coordinate [*Scherllin Pirscher et al*., 2016a]. The value of the combined information of key RO parameters for UTLS monitoring was demonstrated based on observing system simulation experiments [*Steiner et al*., 2001; *Foelsche et al*., 2008b] and dedicated studies on climate change indicators [*Lackner et al*., 2011a].

The RO-accessible atmospheric parameters refractivity, pressure/geopotential height, and temperature were found to show complementary climate change sensitivity. RO data are sensitive at different height ranges and thus provide several suitable indicators to trace climate change in different regions of the UTLS.

### 9.2.1 Monitoring Atmospheric Variability and Extremes

The high vertical resolution, high accuracy and precision of RO are of major advantage for the investigation of atmospheric variability in the troposphere, the tropopause region, and the stratosphere. RO observations can be used to quantify atmospheric variability and extreme events spanning time scales of days, weeks, seasons, intra- and inter-annual to over a decade.

Large scale variations associated with the seasonal cycle, the stratospheric quasi-biennial oscillation (QBO), and El Niño–Southern Oscillation (ENSO) are prominent patterns of natural variability which can be well characterized with RO. Several studies demonstrated the application of RO for investigating the QBO (Figure 31) [*Randel et al*., 2003; *Schmidt et al*., 2005] and ENSO (Figure 32) [*Steiner et al*., 2009; *Scherllin-Pirscher et al*., 2012]. This is, e.g., important in trend detection studies to separate the long-term trend signal from natural variability (section 8.2.2). RO data are also a powerful tool to quantify atmospheric waves, such as diurnal tides [*Pirscher et al*., 2010], Kelvin waves [*Tsai et al*., 2004; *Randel and Wu*, 2005; *Scherllin-Pirscher* et al., 2016a], and stratospheric gravity waves (see also Section 6.4).

RO data are found extremely well suited for the characterization of the tropopause region and the tropical tropopause layer [e.g., *Randel et al*., 2003; *Schmidt et al*., 2004; *Borsche et al*., 2007]. Tropopause variability and changes [e.g., *Schmidt et al*., 2008, 2010; Lewis 2009; *Kim and Son*, 2012; *Rieckh et al*., 2014, *Wang et al*., 2013] and coupling with the upper troposphere and stratosphere [e.g., *Randel and Wu*, 2015] have been successfully investigated.

Further exciting applications of RO comprise the variability of atmospheric water vapour [e.g., *Kursinski et al*., 2016; *Rieckh et al*, 2016] as seen e.g., in the Madden-Julian-Oscillation (MJO) [e.g., *Tian et al*., 2012], and the investigation of extreme events such as e.g., sudden stratospheric warmings [*Klingler*, 2014], atmospheric blocking events [*Brunner et al*., 2016, *Brunner and Steiner*, 2017], or atmospheric impacts from volcanic eruptions [*Wang et al*., 2009; *Ozakaki and Heki*, 2012; *Metha et al*., 2015; *Biondi et al*., 2017].

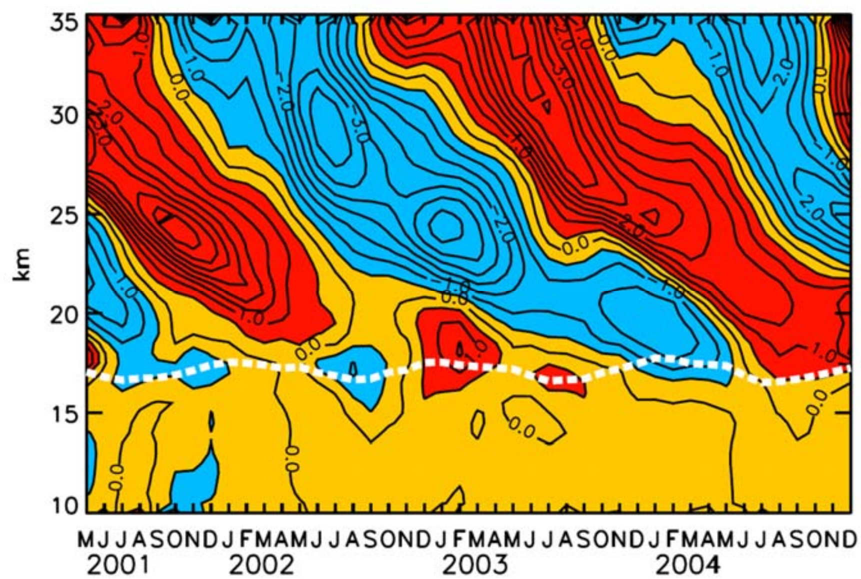


***Figure 31 QBO variability from CHAMP RO temperature anomalies (blue: negative, red: positive) over the equator region (4°S–4°N) for May 2001 to December 2004. The altitude of the cold point tropopause is indicated (white dashed line) [Schmidt et al., 2005].***

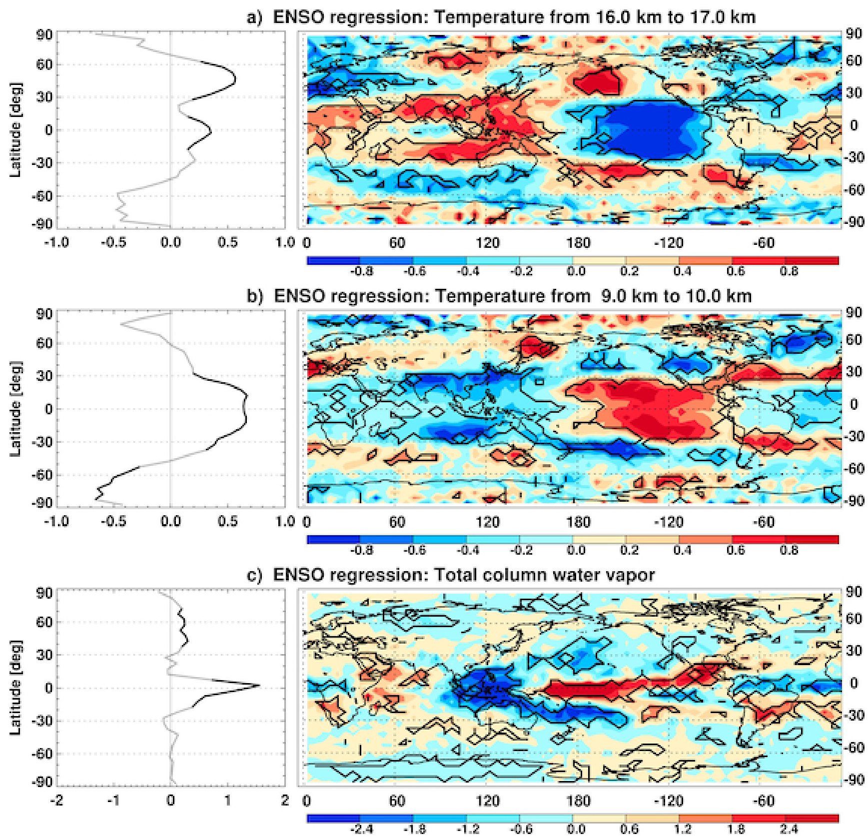


***Figure 32 ENSO variability from RO data. Shown are ENSO regression coefficients of the zonal-mean (left) and eddy (right) temperature fields in the altitude layer from 16 km to 17 km (a) and 9 km to 10 km (b), and of total column water vapour fields (c). Solid black lines enclose areas of statistically significant regressions [Scherllin-Pirscher et al., 2012].***

### 9.2.2 Monitoring and Detecting Climate Trends

The trend detection capability of real RO temperature observations was first demonstrated by *Steiner et al*. [2009a] based on GPS/Met and CHAMP observations within 1995 to 2008. Since GPS/Met provided sufficient observations of good quality only for October 1995 and February 1997, (intermittent) monthly-mean time series for February and October, were tested. Results revealed a significant cooling trend in the tropical lower stratosphere for February 1997 to 2008. In the upper tropical troposphere an emerging warming was obscured by natural variability.

In an optimal fingerprinting study, the RO record of refractivity, geopotential height, and temperature was tested [*Steiner et al*., 2011] on whether RO observations exhibit a UTLS climate change pattern which is consistent with the expected climate change signal as projected in GCMs, for the periods 2001 to 2010 and (intermittent) 1995 to 2010.

The results showed an emerging trend signal in the RO climate record, which was detected for geopotential height (90% confidence level) and temperature (95% confidence level). In the tropics, a geopotential height increase of ~15 m/decade was detected, together with a warming of ~0.3 K/decade in the upper troposphere and a cooling of a ~0.6 K/decade in the lower stratosphere for the period 2001 to 2010 (see Figure 33). The corresponding structural uncertainty in the tropics is for geopotential height <3 m/decade in the UTLS, for temperature 0.02 K/decade in the upper troposphere and 0.07 K/decade in the lower stratosphere, meeting GCOS stability requirements for air temperature.

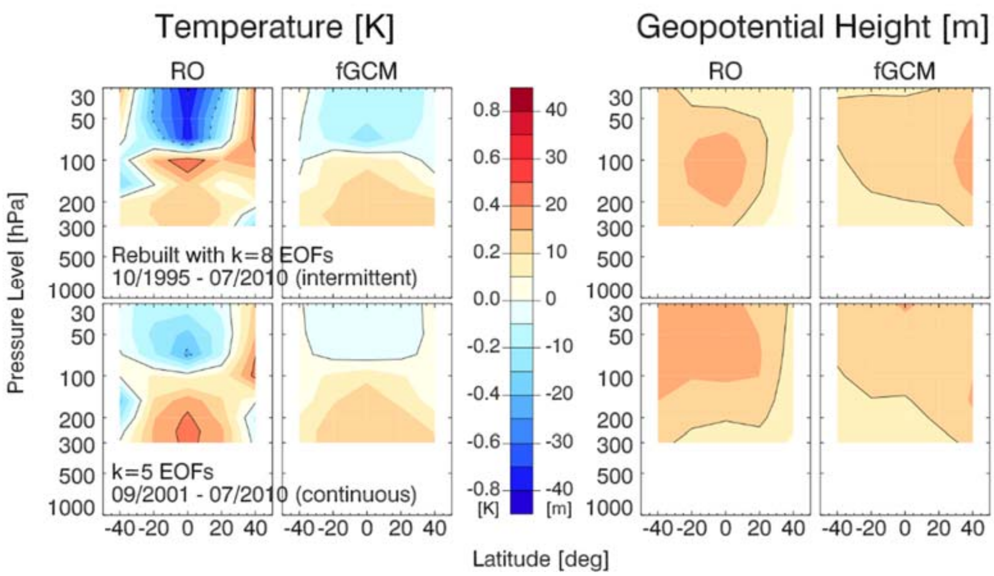


***Figure 33 Trend patterns in RO dry temperature (left) and geopotential height (right). Trends of the intermittent RO period (10/1995, 02/1997, 09/2001–07/2010) (top) and of the continuous period (09/2001–07/2010) (bottom) compare to corresponding trend patterns from global climate models (right subpanels) [Steiner et al., 2011].***

Further work on trends in RO data mainly focused on diagnosing changes in the troposphere and tropopause region. *Schmidt et al*. [2010] used bending angles for deriving tropopause height trends and found a global increase of the tropopause height over the period 2001 to 2009 linked to temperature changes in the UTLS. Follow-on studies by *Wang et al*., [2013; 2015] showed a warming in the tropical tropopause layer over 2001 to 2011. Whereas Gleisner et al. [2015] examined satellite-based data from AMSU and RO for 2002 to 2013 in the lower troposphere, showing stalled warming at low latitudes in the investigated period (see ***Figure 34***). However, atmospheric variability is large [*Randel and Wu*, 2015] and needs to be well characterized, especially for trend detection in vertically resolved data [*Steiner et al*., 2016b], given that the RO record is still short, sensitive to start and end points, for the detection of long-term trends.

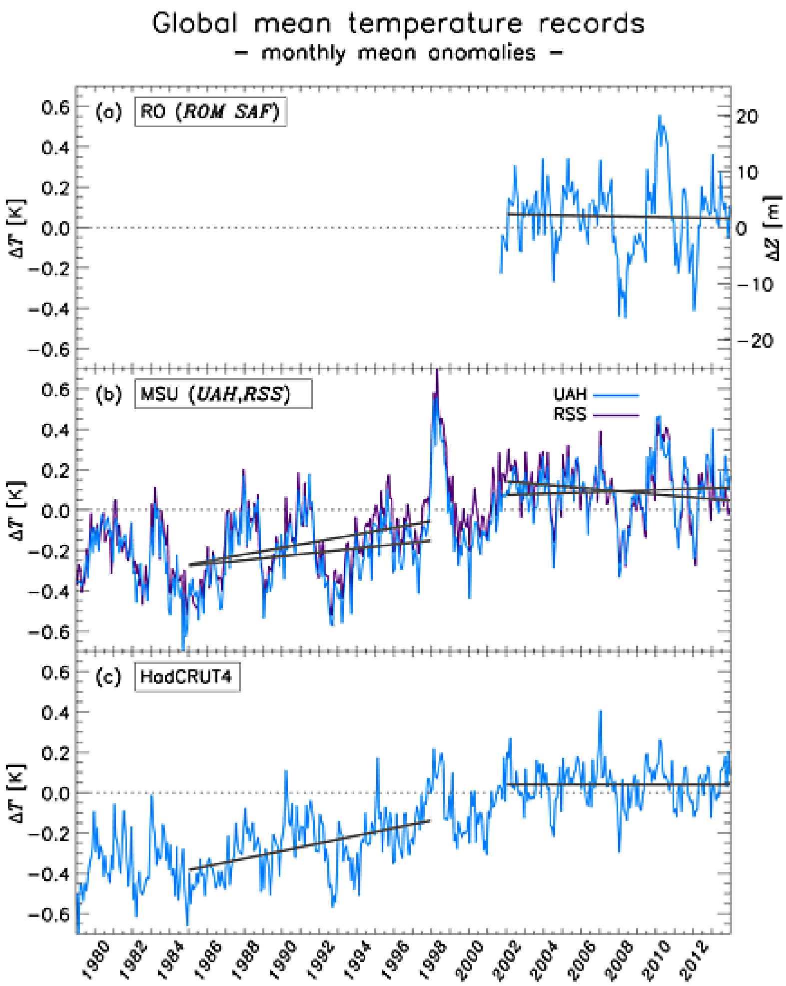


***Figure 34 Global monthly mean temperature records from 1979 to 2013: GNSS-RO 300 hPa geopotential heights from the ROM SAF corresponding to a bulk tropospheric temperature (a), MSU/AMSU global mean lower troposphere temperature from UAH and RSS (b), and surface temperatures fromHadCRUT4 (c). The trend lines indicate the prehiatus (1985–1997) and the hiatus (2002–2013) time periods discussed in the study. [Gleisner et al., 2015].***

### 9.2.3 RO for Evaluating Atmospheric Records and Climate Models

Upper-air temperature records are crucial for detection and attribution of tropospheric and stratospheric climate change and for distinguishing the various possible causes of climate. RO provides benchmark observations that can be used to “calibrate” the other types of temperature measurements and for “anchoring” analysis, re-analysis, and climate model runs since they require no calibration.

Rigorous intercomparison of RO and data of the Advanced Microwave Sounding Unit (A/MSU) has been carried out [*Schroeder et al*., 2003; *Ho et al*., 2007; *Steiner et al*., 2007; 2009b]. *Ladstädter et al*. [2011] detected structural differences between the two records showing a slight divergence in lower stratospheric temperature over time. Possible explanations for the trend differences may be either currently unresolved biases in A/MSU records or so far overlooked error sources in the RO synthetic AMSU temperatures.

However, RO data are found highly useful for the calibration of microwave measurements in the lower stratosphere [*Ho et al*., 2009] in order to identify inter-satellite offsets among measurements from different satellites as well as for identification of biases in radiosonde data [e.g., *He et al*., 2009; *Ladstädter et al*., 2015], shown in Figure 35.

Beside the validation of atmospheric observational records, the use of RO for the evaluation of climate models is of importance. First studies on evaluation of CMIP5 models at standard levels showed the value of RO [*Ao et al*., 2015; *Kishore et al*., 2016] and further potential for more detailed validation at higher vertical model resolution [*Steiner et al*., 2013b]. This topic is becoming of increasing relevance in the next round of the climate model intercomparison project, CMIP6, and provision of RO data for the Observations for Model Intercomparisons Project (Obs4MIPS) is planned as part of the SCOPE-CM project RO-CLIM.

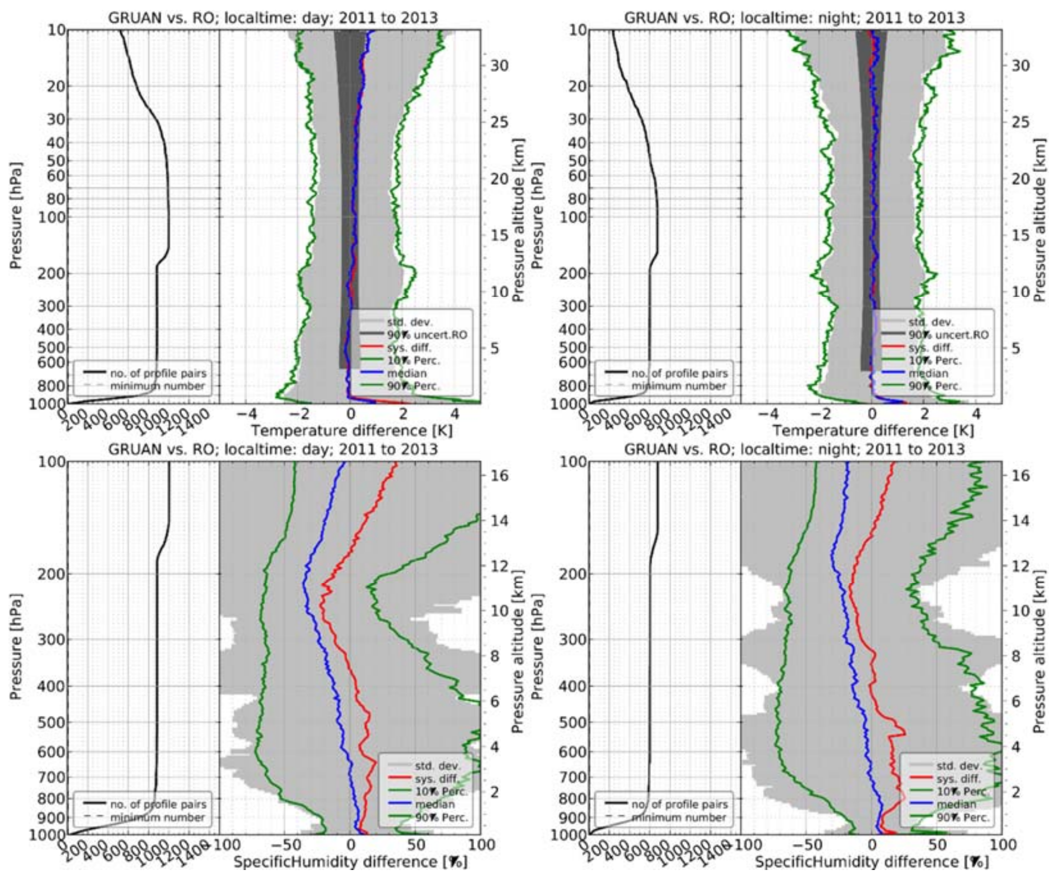


***Figure 35 Global mean difference in temperature (top) and specific humidity (bottom) between GRUAN radiosondes and RO for daytime (left) and night time (right) [Ladstädter et al., 2015].***

# 10 INSTRUMENT AND RO PERFORMANCE MONITORING

Monitoring of the RO instrument will primarily be derived from the activities identified in the EPS-SG RO Cal/Val plan for the Commissioning phase, which in term have been derived from EPS GRAS Cal/Val and monitoring activities - with addition to cover additional RO instrument capabilities. Furthermore, issues identified in this Science Plan were also taken into account in the RO Cal/Val plan. Note that some of the EPS identified activities such as co-location to other than RO observations, or with radio sondes were actually omitted. These were found to be mostly showing issues with the other instruments in various validation campaigns.

## 10.1 EURD Requirements driving the Cal/Val Plan

Generally, the EPS-SG Overall Cal/Val plan does not cover long term monitoring activities, but lists the objectives of Cal/Val as:

- to generate validated products in a timely manner to meet the user requirements and achieve the overall mission objectives;
- to achieve state-of-the-art performance and accuracy from the EPS-SG instruments and their generated data products;
- to ensure consistency and continuity of the EPS-SG products with the EPS ones and among EPS-SG products from subsequent Metop-SG satellites.

Hence the formal Cal/Val plan is driven by the EURD requirements, for RO covering requirements on acquisition, quality, radiometric and geometric ones. These can be further split up into:

- Acquisition:
    - use of GPS, Galileo (Threshold) and GLONASS, COMPASS/BeiDou (Breakthrough);
    - operation on 2 frequencies for each GNSS system;
    - sampling rate adjustments;
    - open-loop tracking in lower troposphere;
    - open-loop tracking at 2 frequencies of each GNSS system;
    - open- and closed-loop simultaneous tracking for setting occultations. Note that this also applies for rising occultations since they have an overlap between open- and closed-loop data too.
- Quality:
    - good quality against acquisition, timeliness, radiometric, spectral, geometric requirements.
- Radiometric:
    - code phase, carrier phase, pseudo range estimates available;
    - carrier amplitude available for all measured GNSS signals;
    - bending angle accuracy within requirements (see Section 4.4);
    - tracking under maximum signal dynamics.
- Geometric:
    - > 2200 occultations / day from 2 satellites;
    - > 1100 occultations / day from 1 satellites;

- coverage from surface to 80km, allowing different sampling rates;
- coverage between 80km and 500km, allowing different sampling rates;
- open-loop tracking from -300km SLTA to 20km;
- geo-location of reference and ray tangent points accurate to < 1.5km (above 6km impact height).

## 10.2 Instrument Health Monitoring

Albeit not a core Cal/Val activity, instrument health monitoring is required to assure high quality products are available. The housekeeping data needs to be monitored to assess the instrument health, covering actually also several of the acquisition requirements. This should thus include:

- monitor temperature/thermal behaviour, wrt limits and do statistics, correlation and trends;
- monitor electrical behaviour/power consumption, wrt limits and do statistics, correlation and trends;
- monitor, if applicable, on board buffers use for data storage;
- monitor number of tracked GNSS satellites on all antennas;
- monitor tracking/tracking state performance on all antennas;
- monitor tracking of L1 and L5 frequencies;
- monitor noise level (including DME/TACAN interference on L5) and trends;
- monitor USO stability (TBC, might require POD run);
- monitor impact of any other instrument on monitored RO parameters;
- monitor correct direct satellite data dissemination for local and regional service;
- monitor impact of manoeuvres/other events (e.g. PL-SOL) on all other parameters monitored.

## 10.3 Low Level Monitoring

For the End-User products, in particular radiometric and geometric requirements are needed to be monitored (remaining acquisition requirements not covered in the housekeeping monitoring can easily be covered by bending angle monitoring) and here in particular the bending angle accuracy (radiometric) and the number of occultations (geometric).

Hence, monitoring should include:

- DME/TACAN monitoring/interference:
    - monitor magnitude and trend of level 0 parameters measuring the interference level;
    - monitor the occultation data quality over hot spots of DME/TACAN interference;
    - monitor the occultation data quality between hot and cold spots of DME/TACAN interference;
    - monitor the penetration depth on the L5 frequency.

- Tracking and noise monitoring:
  - continuously monitor the penetration depth of the L1, L5 signals on the occultation antenna for open- and closed-loop tracking, separate by latitude band, by day/night, by setting and rising, by GNSS system and frequency;
  - where applicable, compare open- and closed-loop data in term of amplitude and phase, compare overlapping regions of sampling rate changes;
  - continuously monitor whether any gaps in tracking occur, in particular monitor if gaps occur that are neither covered in open- nor in closed-loop data, do statistics for altitude, setting/rising, region, GNSS satellite/system if applicable;
  - monitor the vertical coverage of the occultations, separate by latitude band, setting/rising, GNSS system observed, local time (for ionospheric effects), both for open- and closed loop data;
  - continuously monitor mean phase noise, mean SNR, mean signal power and mean noise power for measurements at 60 km < SLTA < 80 km and also in regions where Ionospheric scintillations/Ionospheric features might impact signal tracking (in particular around the region of sporadic E-layer appearance, for 70 km < SLTA < 90 km, TBC).

## 10.4 Level 1A Monitoring

Level 1A is an intermediate product level, nevertheless some monitoring activities can be identified / are needed:

- noise characteristics of level 1a products (like L1 and L5 excess phase delays) shall be estimated with statistical methods like e.g. the generalised cross validation (GCV) technique;
- noise correlations shall be estimated by calculating auto-correlations of the GCV residuals;
- data shall be visualised as a time series, allowing to split this data into latitude bands and day/night subsets.

## 10.5 Precise Orbit Determination Monitoring

The following core POD specific monitoring activities are needed:

- continuously monitor the number of tracked satellites on the zenith antenna for each GNSS system observed;
- continuously monitor the POD orbit/clock bias and drift solution against a reference solution (that can be e.g. run daily), separate radial, along-track, cross-track components;
- continuously monitor the POD velocity solution against a reference solution (that can be e.g. run daily), separate radial, along-track, cross-track components;
- continuously monitor the residuals of the orbit against a reference solution (that can be e.g. run daily);
- continuously monitor the POD orbit/clock bias performance and the residuals for overlapping arcs from the current POD and the previous POD run, separate radial, along-track, cross-track components;

- evaluate impact of the RSN GNSS orbit/clock bias and drift solutions against the impact of an independent, e.g. IGS based, GNSS orbit/clock bias and drift solution, separate radial, along-track, cross-track components (could be part of the reference solution setup mentioned above, otherwise it should be performed in regular intervals);
- evaluate the LEO orbit/clock bias and drift solution by comparing it to a solution obtained from an independent POD software (this could be a one off exercise);
- evaluate POD orbit/clock bias and drift solutions based on GPS or Galileo alone against each other and against using both GNSS systems, separate radial, along-track, cross-track components;
- assess the orbit solution during each manoeuvre;
- continuously monitor the impact of yaw, pitch, roll information on the quality of the POD solution;
- continuously monitor the LEO orbit prediction against the estimation;
- for regional processing, either continuously monitor the orbit/clock bias and drift solutions of the global and the regional processing, or, if predictions are used, focus in particular on the occultations arcs used in the regional processing, separate radial, along-track, cross-track components.

## 10.6 Bending Angle/Number of Occultation Monitoring

The following core activities are identified, which are generally performed on thinned impact height levels when profiles are used:

- continuously monitor the bending angle performance (robust statistics of bias and standard deviation, outlier analysis) vs. an NWP forecast from e.g. ECMWF, separate for different latitude bands, setting and rising, day/night, GNSS systems, PRNs of GNSS satellites (optionally also include the GNSS satellite clock information), DME/TACAN interference level. This activity includes at least a 1DVar based (O-B)/B evaluation (where NWP fields are forward propagated) but could be extended to run a full 1DVar (which would then include monitoring of retrieved temperature, humidity, number of iterations needed in 1DVar, convergence, etc);
- continuously monitor the bending angle performance (robust statistics of bias and standard deviation, outlier analysis) against NWP forecast at one or more altitudes over at least the last 2 weeks for a trend assessment;
- continuously monitor the bending angle (robust statistics of bias and standard deviation, outlier analysis, penetration depth analysis) against other available RO missions, using a co-location criteria of < 300km and < 3 hours (this activity depends on available RO missions and access to data, but should at least include the Metop GRAS instruments, Jason-CS, potentially third party mission like COSMIC-2, ...), separate for different latitude bands, setting and rising, day/night, RO mission/GNSS system;
- compare bending angles (robust statistics of bias and standard deviation, outlier analysis, penetration depth analysis) as derived from the operational processor to those derived from another processor, e.g. the prototype;
- continuously monitor if extrapolation of bending angles at lower altitudes is required in the processing (caused by one GNSS frequency tracking not being available for all

altitudes covered in the other frequency tracking). If extrapolation is found, the monitoring shall include the altitude range over which extrapolation was required, the frequency that was extrapolated;
- continuously monitor the bending angle difference (robust statistics of bias and standard deviation, outlier analysis) between L1 and L5 over all altitudes, including trends over the last at least 2 weeks, further separate into open- and closed-loop where applicable;
- continuously monitor the bending angles (neutral and on L1, L5) from the regional processing vs. the one from the global processing;
- continuously monitor the bending angle behaviour on the two frequencies at ionospheric altitudes, eventually against other available RO missions or using forwarding propagated bending angles from ionospheric numerical models.
- separation of atmospheric scenarios based on e.g. refractivity gradients derived from NWP fields in the lower troposphere. Sorting of these occultation according to the gradient magnitude in order to assess that tracking behaviour is not impacted by the atmospheric condition. This will need to take into account the potentially different SNR levels that these occultations experience.

Regarding the number of occultations per day, core activities for this monitoring should include:

- continuously run an occultation simulator for all EPS-SG LEO satellites carrying an RO instrument, predicting occultations based on propagated GNSS and LEO orbits for the next 14 days. The simulator uses the most recent GNSS constellation information ideally from an independent source than RSN;
- evaluate the occultations per day and LEO satellite as found in the simulator and compare them to the actually observed numbers;
- continuously evaluate options for increasing the number of occultations per day, by checking reasons for non-nominal occultations, checking availability of GNSS satellites provided by RSN, checking availability of GLONASS/BeiDou systems.

### 10.7 Examples of Monitoring Plots

Examples from the routine EPS GRAS bending angle, occultation number, timeliness monitoring are provided below, covering a 2 week interval in May/June 2017. Profile evaluation is following NWP practise and is performed against ECMWF 12h forecast, calculating at each altitude level the ratio of observation (O) minus background (B) normalized to the background: (O-B)/B [%].

- Figure 36 shows bias and standard deviations for different latitude bands, including further information on e.g. total number of occultations, failures;
- Figure 37 shows a time series of bias and standard deviation around 50km impact height for different latitude bands, setting and rising;
- Figure 38 shows the timeliness of each occultation over the 2 week period;
- Figure 39 shows the number of occultations per 6h interval over the 2 week period.

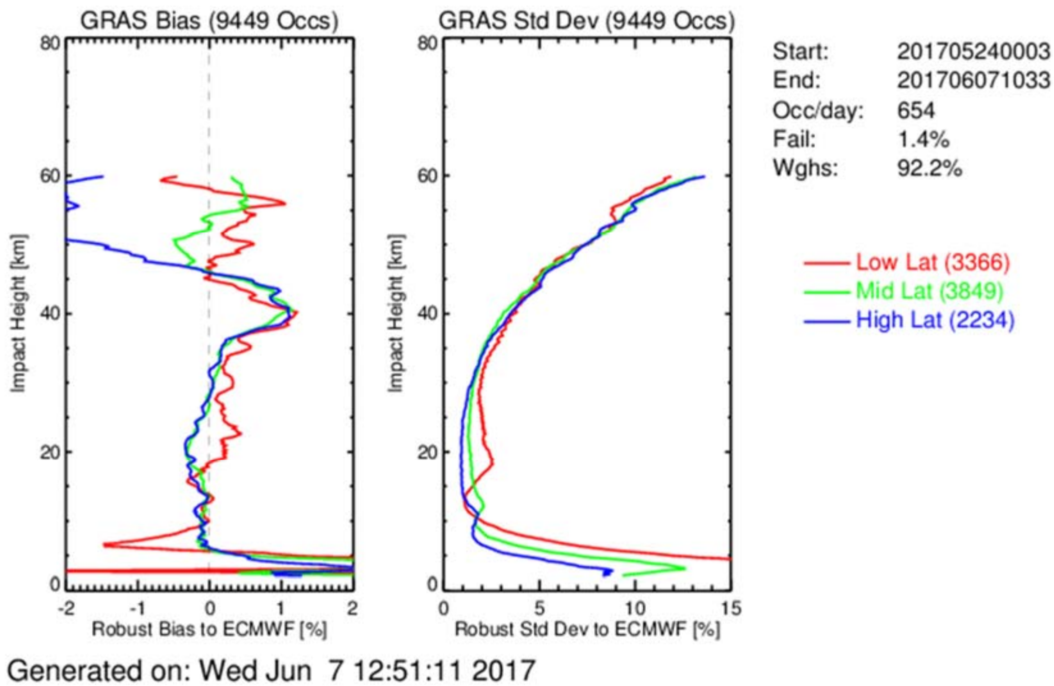


***Figure 36 Routine Metop-A GRAS monitoring plot of robust bias (left) and standard deviation (right) vs. ECMWF 12h forecast data ((O-B)/B) for a 2 week period for different latitude bands (separated by 30° steps). Legend gives the time range, average number of occultations per day (without quality control), the failures (e.g. incomplete tracking, no second frequency available, etc), and the average weight over all altitudes of the robust estimator. Numbers in brackets are found occultations in latitude band.***

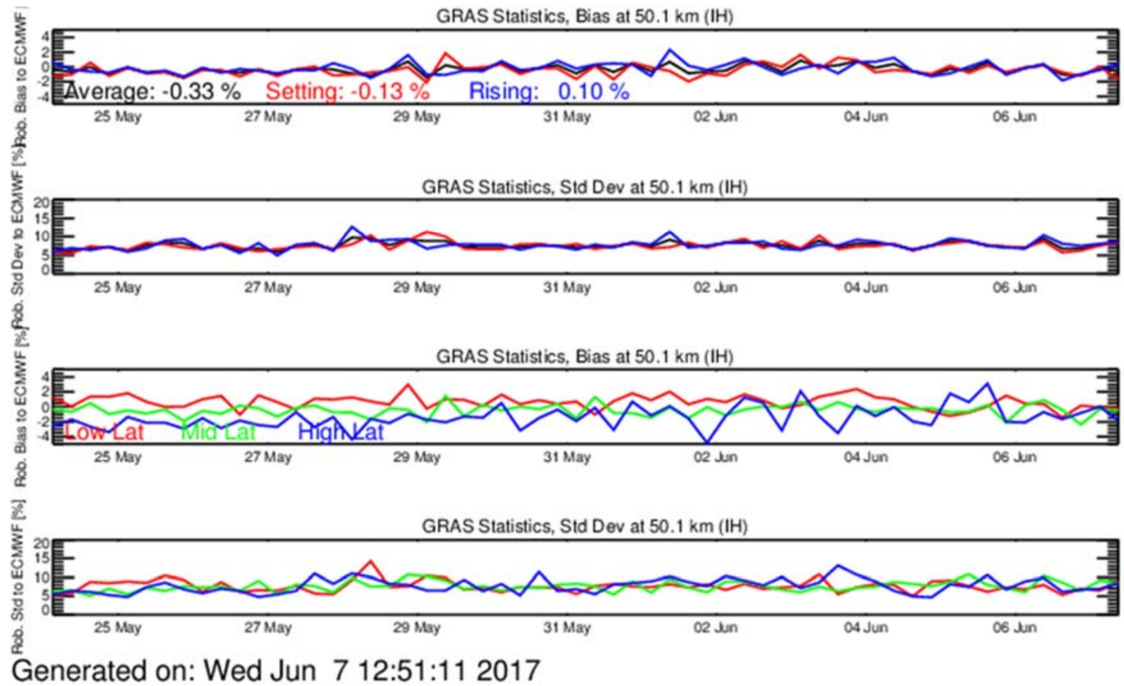


***Figure 37 Routine Metop-A GRAS monitoring plot of 6h timeseries of robust bias (top for setting and rising), standard deviation (2nd to top for setting and rising), and the latitudinal bias and standard deviations (bottom 2 plots) vs. ECMWF 12h forecast data ((O-B)/B) for a 2 week period around 50km impact height.***

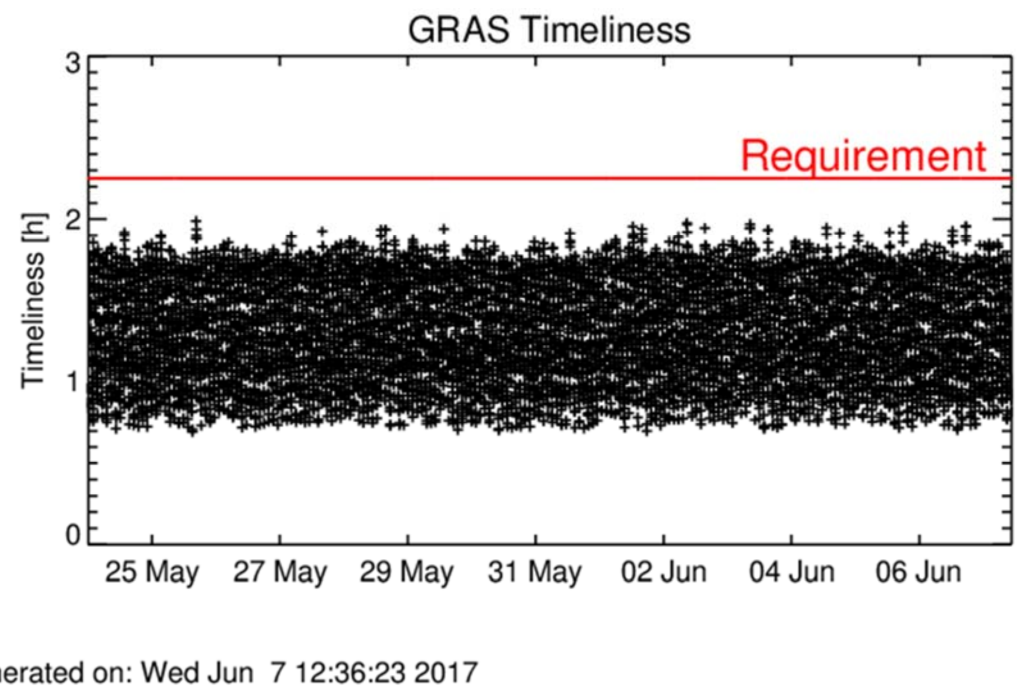


***Figure 38 Routine Metop-A GRAS monitoring plot of occultation timeliness, also showing the requirement of 2:15h, for a 2 week period.***

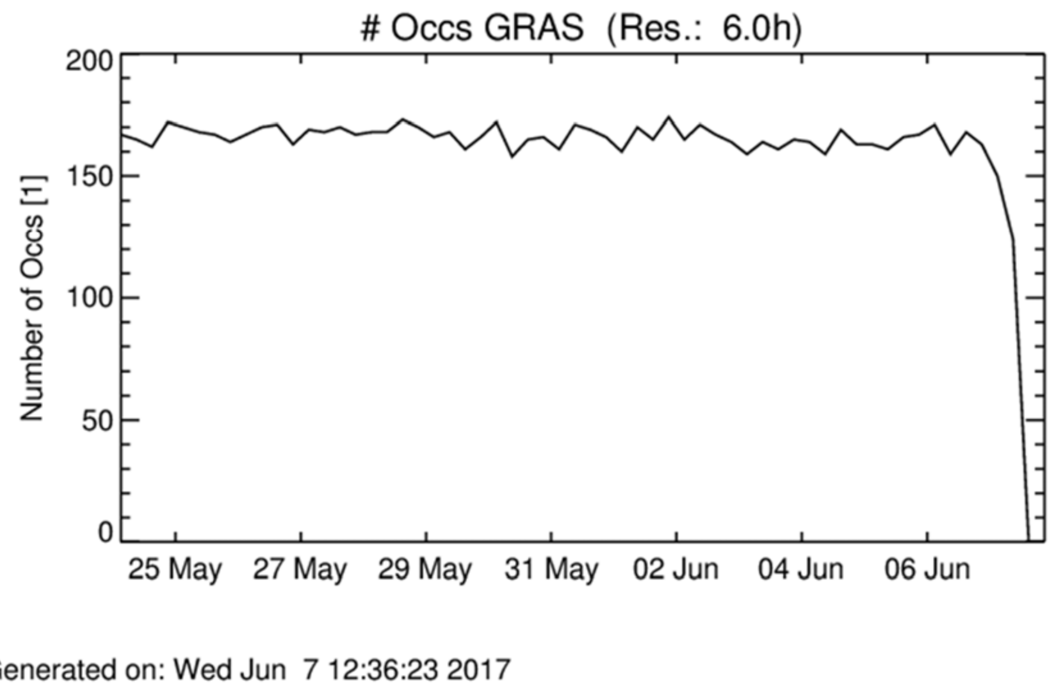


***Figure 39 Routine Metop-A GRAS monitoring plot of number of occultation per 6h interval for a 2 week period.***

# 11 RO RELATED DATA PROCESSING AND PRODUCTS

The RO Science Plan primarily deals with the core radio occultation EPS-SG products; there is however a wider range of "related" products, derived either from radio occultation measurements themselves, or derived from e.g. reflected GNSS signals. The following sections give an overview of some of the possible products.

## 11.1 Reflectometry: Sensing of the Surface Layer

Each GNSS transmitter illuminates the Earth surface and its surrounding atmosphere. The signals reaching the planetary surface can bounce forward towards the LEO RO receiver. Generally, the reflected signals have longer delays than the direct ones (usually longer than the GNSS modulation chip length), as well as distinct Doppler shifts, outside the bandwidth of the tracking loops. Moreover, after a process of diffuse scattering off rough surfaces the reflected signals are generally incoherent and with swapped polarization. The combination of these particularities makes it impossible for a RO receiver to track the reflected signals through the same correlation channel as the direct ones.

Nevertheless, when a radio occultation reaches the lowest few kilometres of the atmosphere, the reflected signals transmitted by the same GNSS source have bounced in a very low elevation angle of observation, under which the effective roughness of the surface tends to vanish (h_eff-roughness ~ h_roughness sin(elevation) ) and consequently the scattering process becomes mostly coherent. Moreover, under these very slant geometries (elevation angles of the order of 1 degree), the polarization does now swap, the co-polar reflectivity is high, and the delay and Doppler shifts of the reflected signal get closer to the direct one, to the point that the delay is within a GNSS modulation chip length (~300 m for the GPS C/A code) and the effective bandwidth of the tracking system.

In these circumstances, the reflected signal interferes with the direct one and is captured by the RO receiver. *Beyerle et al.* [2002] identified these interferences as signals reflected, which were used in [*Cardellach et al.*, 2004] for ice altimetry. In the frame of the GRAS and the ROM SAF, an effort was done to automatically identify when RO events present reflected signals [*Cardellach and Oliveras,* 2016], and the set of flagged data has been made available at http://www.romsaf.org/priv/demo/reflection_flag/.

The studies pursued by the ROM SAF have also identified geographic and seasonal patterns in the climatology of reflected signals, as seen in *Cardellach and Oliveras* [2016], *Aparicio et al.* [2016]. An interesting particularity is the high anti-correlation of ocean RO reflections with sea surface temperature, which leads to clear capture of the El Niño signatures in certain regions (see Figure 40). One of the conclusions of these studies is that reflections over the Oceans tend to be captured by RO, except when the atmospheric conditions above the surface are wet and unstable. On the contrary, the rugged terrain over land and the absorbing vegetation layer hinder the process in most conditions.

The potential use for NWP was first assessed in [*Cardellach et al.,* 2008] noticing that in the bottom 10 km of the atmosphere, those RO with presence of reflected signals better compare to ECMWF background than RO without reflected signals. This has been confirmed in *Cardellach and Oliveras* [2016] and *Healy* [2016], although its straight use for weighting the

RO data in the numerical assimilation has been finally rejected by the latter. *Boniface et al.,* [2011] suggested an inversion approach from reflected phase-delay to refractivity, while more recently *Cardellach et al.* [2015] and *Aparicio et al.* [2016] have suggested the use of the reflected impact-bending profile as observable for the surface atmospheric layer (see Figure 41). As explained in these references, the ROM SAF has also developed algorithms to extract such reflected impact-bending profiles and its forward operator. Preliminary assimilation exercises of this observable are being conducted at Environment Canada under the ROM SAF CDOP2 [*Cardellach et al.*, 2015].

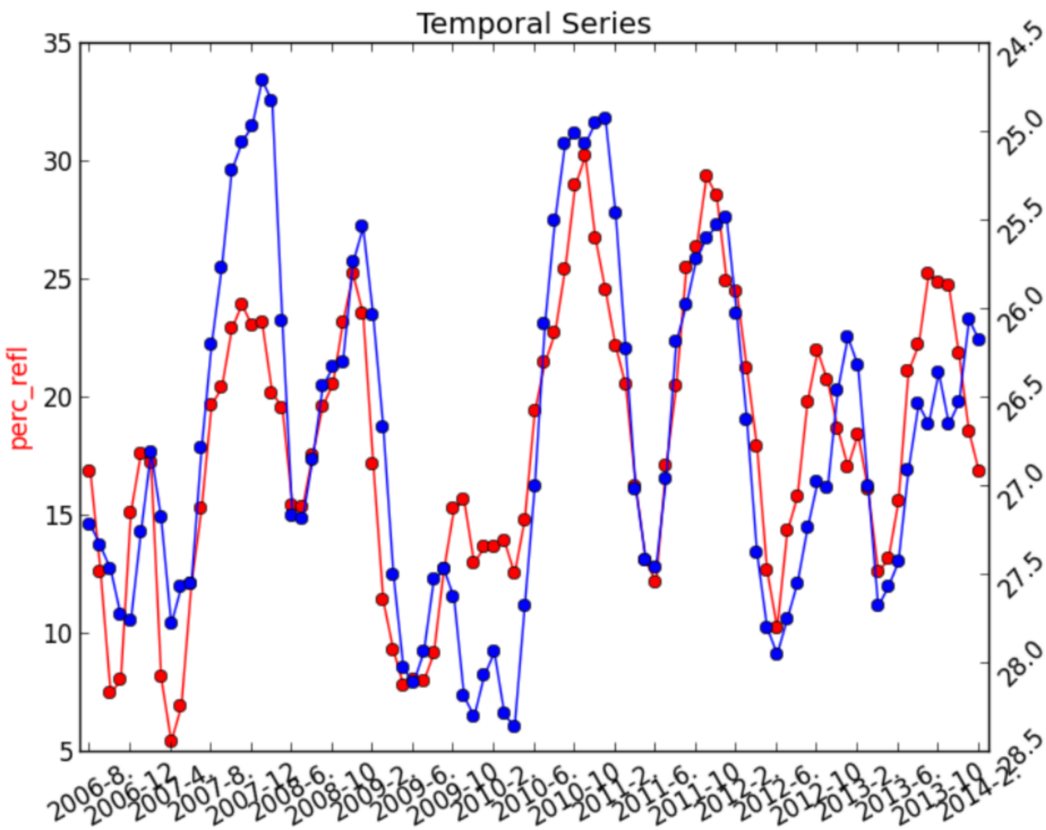


***Figure 40 Monthly time series of the percentage of reflected signals in El Niño 3.4 zone [5° North-5° South 170-120° West] (red) with 3 months smoothing filter and the ENSO 3.4 coefficient from [http://www.esrl.noaa.gov/psd/gcos_wgsp/Timeseries/Nino34/](http://www.esrl.noaa.gov/psd/gcos_wgsp/Timeseries/Nino34/) in reversed axis (blue). Unpublished figure by the ROM SAF.***

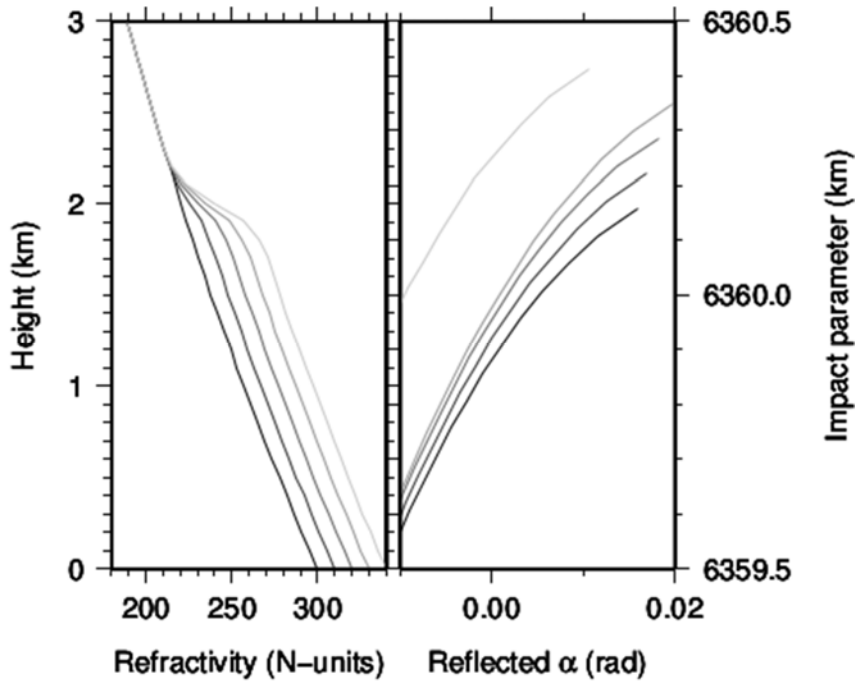


***Figure 41 The left panel shows a family of atmospheric refractivity profiles, generated as an exponential function, intended to represent a smooth profile, with a more refractive lower layer, modelled as an error-function. The right panel shows the corresponding series of reflected bending and impact parameters, as evaluated by the forward operator developed by the ROM SAF, and indicates that the profile of reflected bending is sensitive to the amplitude of the extra layer. Figure from [Aparicio et al., 2016].***

## 11.2 Extended Reflections: Mesoscale Ocean Altimetry

It would be relatively simple for a RO receiver to upgrade its capabilities for tracking reflecting signals using dedicated channels in open-loop mode, as far as these signals are still coherent not diffuse scattering). *Semmling et al.* [2014] reports, from airborne experiments at 3500 meter altitude, that reflections up to 30 degree elevation (elevation computed at the specular point) still present coherence and their phases can be tracked, even when using a RHCP antenna. From the LEO receiver point of view, this corresponds to elevation angles a few degrees below the Earth limb.

For example a signal reflecting at 20 degrees elevation at the specular point is acquired ~7-8 degrees below the Earth limb at the ISS [*GEROS ESA Team*, 2015]. These reflected signals, tracked through dedicated channels of the receiver, could be useful for altimetric applications, with expected sea surface height precisions of the order of 11 cm in a few km along-track resolution [*GARCA TEAM,* 2016]. An example of altimetric retrievals using synthetic data as if collected from the ISS is shown in Figure 42. This would be an efficient way to densify the mesoscale and sub-mesoscale altimetric observations, one of the current challenges of the global observational system [*Flechter et al*., 2015].

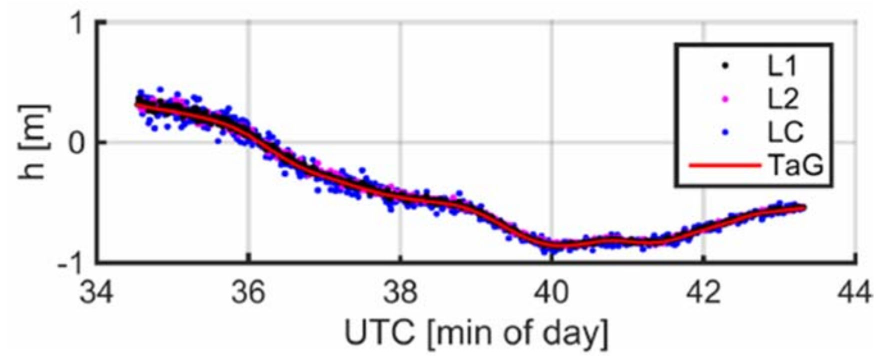


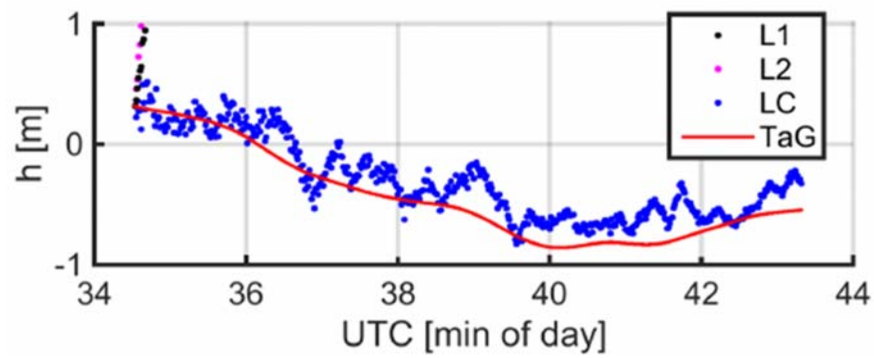


***Figure 42 Phase delay altimetry in grazing angles of elevation (up to ~30°), from synthetic data as collected from the ISS. On the top, assuming no systematic effects (only noise of the phase). On the bottom a scenario that includes most critical effects, the ionosphere (10% residual errors), the wet troposphere (0.5% error) and the 5 cm standard deviation in the radial receiver orbit, with 10 seconds correlation time. TaG for Topography above the Geoid. Figure generated by GFZ for the ESA GARCA study [GARCA Team, 2016].***

Indeed, *Saynisch et al.* [2015] have shown, by means of OSSE exercises, that these measurements would have a significant impact on Ocean models. Although the GNSS-R based SSH observations were only assimilated at 25% of the OSSE model domain's surface area, the RMS of all sub-surface properties improved substantially throughout the domain. In summary, the study provided a demonstration of the usefulness of slant GNSS-R observations to recover the true 3D ocean state and the connected oceanographic processes. ESA's GEROS-ISS mission plans to include these type of grazing reflected signals [*Wickert et al.,* 2016].

Therefore, a LEO equipped with RO payload including antennas with coverage down to several degrees below the Earth limb and dedicated channels in open-loop (with open-loop models tuned for reflected signals) could in principle extend the applications to mesoscale and sub-mesoscale ocean altimetry.

### 11.3 Near-Nadir Reflections: Ocean Altimetry & Scatterometry; Land & Cryosphere

This type of GNSS reflections have been investigated since late 1990s, for both sea surface roughness estimates—scatterometry, wind vectors and waves [e.g. *Garrison et al.,* 1998, *Zavorotny and Voronovich,* 2000] and mesoscale ocean altimetry (e.g. *Martín-Neira* [1993; 2011]; *Rius et al.* [2010]). Land applications such as soil moisture (e.g. *Masters et al.* [2004]; *Katzberg et al.* [2005]) and biomass determination (e.g. *Egido et al.* [2014]) as well as cryospheric applications (sea ice thickness and type (e.g. *Komjathy et al.* [2000], snow monitoring e.g. *Cardellach et al.* [2012]) have also been studied.

A list of space-borne missions currently implement or plan to implement some of these capabilities: UK-TDS1, launched July 2014 [*Foti et al.*, 2015]; UPC ³Cat-2 [*Carreno-Luengo et al.*, 2013] launched August 2016; NASA/CYGNSS [*Ruf et al.*, 2012] to be launched December 2016; ESA's GEROS-ISS [*Wickert et al.*, 2016], planned for 2020.

High elevation reflections are not coherent, the antenna pointing and pattern features, together with the receiver architecture are all notoriously different from a RO system, therefore this type of reflectometry is not considered here.

### 11.4 Polarimetry: Hydrometeors

The use of a 2-pol (linear H/V) RO receiving system was suggested for the Radio-Occultation and Heavy Precipitation aboard PAZ (ROHP-PAZ) experiment [*Cardellach et al.*, 2014]. The idea behind the concept is that under RO geometry the signals cross the lowest layers of the atmosphere, where precipitation occurs, tangentially to the main axis of asymmetry of the droplets of intense rain. Therefore, the phase delay suffered by the local horizontal component (long axis of the droplet) should be larger than the delay suffered by the local vertical component (short axis of the droplet). This rain-induced shift between both polarizations is the expected observable of the experiment. Given that the flattening of the droplets is larger as more intense is the precipitation, the asymmetry between both (and therefore the measurable observable) should also increase with heavier rain episodes.

The same reference presented a suit of simulation work, based on T-matrix scattering approach, to assess about the expected sensitivity of the concept to intense precipitation: rain-induced polarimetric phase-shift delays of several millimetres and up to the centimetre level were reported, above the noise threshold (Figure 43).

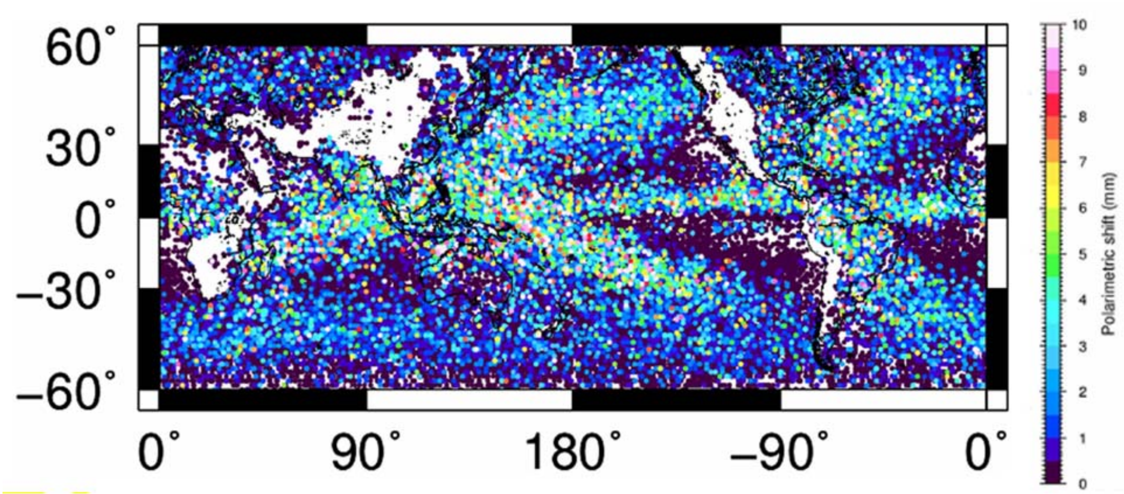


***Figure 43 Geolocated polarimetric phase-shift delay that rain events in COSMIC RO would have induced if they were polarimetric (rain information from collocations with the TRMM mission). The noise level of the measurement is expected at 1-1.5 mm in 1 second observation. Figure from [Cardellach et al., 2014].***

*Padullés et al.* [2016] shown the results of a ground-based campaign with grazing (near RO) 2-pol H/V GNSS observations, capturing 5 heavy rain events. Intense precipitation episodes were indeed linked to higher polarimetric features in the signals, which in turn were higher than predicted by the models (Figure 44). The theoretical study including other hydrometeors (ice crystals in clouds and melting particles) confirmed that the order of magnitude of the measured signals could be reproduced when these other hydrometeors were included in the analysis.

*Padullés et al.* [2016b] presented 2D tomographic techniques as a preliminary way to resolve the location, size and intensity of the precipitation cells along the RO ray path. The PAZ satellite is ready for launch, and its launch date to be confirmed. The current plans for GEROS-ISS [*Wickert et al.*, 2016] also include polarimetric RO, in the form of RHCP/LHCP interferometric (rather than H/V C/A code clean-replica processing).

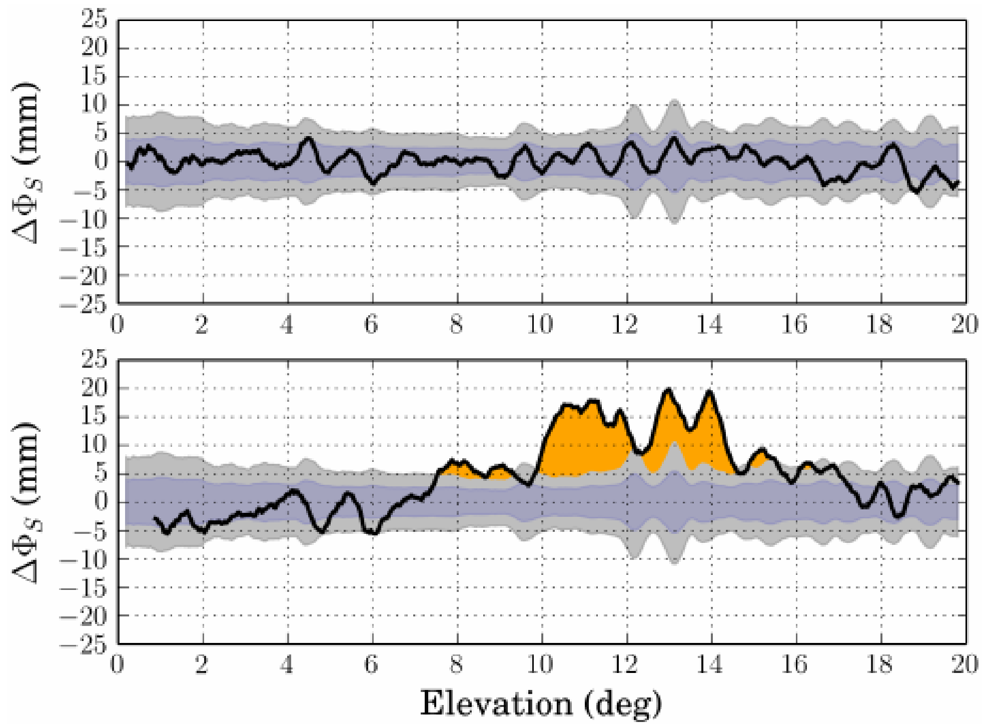


***Figure 44 Examples of polarimetric phase-shift delay (black line) measured during the PAZ experimental ground-campaign, together with the uncertainty given by ±σ (blue) and ±2σ (grey) computed with all events of the same PRN when there was no-rain. They correspond to PRN G22 on 26 May 2014 (top) and 14 June 2014 (bottom). The top measurement is well inside the 2σ contour, showing no polarimetric signatures. It corresponded to a day without rain. In the bottom panel, large positive values above the 2σ are observed, and it corresponded to an intense precipitation event. Figure from*** **[*Padullés et al.*, 2016].**

# 12 RO RESEARCH & DEVELOPMENT AND OUTREACH NEEDS

## 12.1 State of the Art

First RO observations of the Earth's atmosphere were made by the US GPS/Meteorology (GPS/Met) proof-of-concept mission. Measurements were provided for several periods within the years 1995 to 1997 [*Ware et al.*, 1996]. Continuous observations were provided by the German CHAMP (CHAllenging Minisatellite Payload for geoscientific research) satellite [*Wickert et al.*, 2001; 2004]. CHAMP data are available for mid-2001 to 4 October 2008 with only one data gap from 3 July to 8 August 2006.

The Argentine SAC-C (Satélite de Aplicaciones Científicas) [*Hajj et al*., 2004] and the German GRACE (Gravity Recovery and Climate Experiment) mission [*Wickert et al.*, 2005; *Beyerle et al*., 2005] were both launched in 2002 with GRACE being still active. SAC-C and GRACE data complement and continue CHAMP data and can be used to fill the CHAMP data gap.

The first constellation mission for providing near-real-time RO data to operational weather centres is the Taiwan/US Formosat-3/COSMIC (Formosa Satellite Mission 3/Constellation Observing System for Meteorology, Ionosphere, and Climate; F3C) [*Anthes et al*., 2000; *Rocken et al*., 2000; *Wu et al*., 2005; *Anthes et al*., 2008]. F3C was launched in 2006 and consists of six receiving satellites. Meanwhile, the F3C satellites are slowly degrading but RO data collection is continued in order to minimize data gaps until the proceeding Formosat-7/COSMIC-2 mission will be implemented.

The European MetOp/GRAS (Meteorological Operation/Global Navigation Satellite System (GNSS) Receiver for Atmospheric Sounding) mission started in 2006 [*Loiselet et al*., 2000]. It consists of a series of three satellites launched in sequence to operationally provide RO data until at least the year 2020 [*Luntama et al*., 2008]. Since recently, also the German TerraSAR-X and Tandem-X satellites provide RO data [*Wickert et al*., 2009; *Beyerle et al.*, 2011]. Further small satellites, such as the Communications/Navigation Outage Forecasting System (C/NOFS) contribute more RO data.

The quality of RO data has been confirmed by a broad range of studies including error analyses (e.g., *Steiner and Kirchengast* [2005]; *Scherllin-Pirscher et al.* [2011a;b]; Ho et al. [2012]) and comparison with other observations. Comparison with radiosonde data showed the high accuracy of RO data, which are even able to identify systematic temperature biases and quality issues in different types of radiosonde sensors (e.g., *Kuo et al*. [2005]; *Sun et al*. [2010]). Intercomparison with satellite data from MIPAS (Michelson Interferometer for Passive Atmospheric Sounding) and GOMOS (Global Ozone Monitoring for Occultation of Stars) demonstrated the high quality and unbiasedness of RO [*Gobiet et al*., 2007].

Validation with different atmospheric analyses showed the high vertical resolution and accuracy of RO [*Gobiet et al*., 2005; 2007; *Foelsche et al*., 2009a] and pointed out its value for, e.g., investigations of the tropopause region, but also for the improvement of atmospheric analyses themselves [*Schmidt et al*., 2004; 2005; *Gobiet et al*., 2005; *Borsche et al*., 2007].

Atmospheric studies demonstrated that the application of RO ranges from investigating the planetary boundary layer [*Sokolovskiy et al*., 2006] via addressing ENSO [*Steiner et al.*, 2009; *Scherllin-Pirscher et al.*, 2012] to atmospheric waves, such as diurnal tides [*Pirscher et al.*, 2010], the QBO [*Randel et al.*, 2003; *Schmidt et al.*, 2005], Kelvin waves [*Tsai et al.*, 2004; *Randel and Wu*, 2005], and stratospheric gravity waves (e.g., *Steiner and Kirchengast* [2000]; *Tsuda et al.* [2000]; *de la Torre and Alexander*, [2005]). The benefit of RO for improving Hurricane forecast has been shown (e.g., *Liu et al.*, [2012]).

The significant impact of RO on weather forecasting has been successfully proven (e.g., *Healy et al.* [2005]; *Healy and Thépaut* [2006]). RO has reduced stratospheric temperature biases and has anchored radiance bias correction in NWP because of its superior vertical resolution and assimilation without bias correction. RO was recently ranked within the top five most important observation types for its contribution to short-range forecast error reduction [*Cardinali*, 2009]. Meanwhile all main weather centres worldwide operationally assimilate RO observations into their NWP models. This also results in improved operational atmospheric analyses and reanalyses data (e.g., *Poli et al.* [2010]) which are frequently used in climate studies.

The capability of GPS RO for climate change monitoring and modelling was tested based on observing system simulation experiments [*Steiner et al.*, 2001; *Foelsche et al.*, 2008b] inferring that the combined information of key RO parameters for UTLS monitoring is of high value for climate studies. *Leroy et al.* [2008] investigated climate signal detection times and constraints on climate benchmark accuracy requirements. RO bending angle profiles based on climate model simulations were used to examine the effect of increasing greenhouse gases by *Ringer and Healy* [2008]. Their estimates of climate signal detection times in UTLS bending angle trends of 10 to 16 years are consistent with *Leroy et al.* [2008] and *Foelsche et al.* [2008b]. Based on real RO data, *Schmidt et al.* [2008] inferred tropopause height trends.

First trend detection studies were performed by *Steiner et al.* [2009b] and *Schmidt et al.* [2010]. An emerging climate change signal, reflecting warming of the troposphere and cooling of the lower stratosphere, was detected by *Lackner et al.* [2011] based on RO observations of the last decade. A comprehensive overview on the achievements of RO so far for exploring weather, climate, and space weather is provided by *Anthes* [2011].

The products retrieved from present RO missions and available from state-of-the-art on-line archives can be summarised as follows:

- Neutral atmosphere: bending angle and refractivity profiles, from which profiles of pressure, geopotential height, temperature, and humidity are subsequently retrieved.
- Ionised atmosphere: electron content (large-scale ionisation structures) and vertical electron density profiles, amplitude and phase scintillation (small-scale ionisation structures).
- Thermosphere: neutral density (from satellite drag)

The state-of-the-art type of measurements, their requirements and associated applications are summarised in the table below:

| Measured/ retrieved | Atmospheric region | Signal requirements | Further requirements | Applications |
|---|---|---|---|---|

| parameter | | | | |
|---|---|---|---|---|
| Bending angle, refractivity, pressure, geopotential height, temperature, humidity | Troposphere, Stratosphere | L1, L2 or L2C | 50 Hz sampling rate | Atmospheric physics,<br><br>weather forecasting, climate monitoring and trend analyses, climate modelling, evaluation/validation of atmospheric data sets and models |
| Electron density | Ionosphere | L1, L2 or L2C | 1 Hz sampling rate | Radio propagation nowcasting and forecasting, ionospheric physics, space weather monitoring |
| Amplitude scintillation | Ionosphere | L1 and/or L2C | 50 Hz sampling rate | Radio communication, radio propagation nowcasting and forecasting, ionospheric physics, space weather monitoring, satellite navigation |
| Phase scintillation | Ionosphere | L1 and/or L2C | 50 Hz sampling and low noise oscillator | |

Overall, the quality, consistency, and reproducibility of RO data was found favourable for use in climate monitoring and change detection, and for becoming a climate benchmark record, though current use for climate trend assessment is bound to 50°S to 50°N (see *Steiner et al.*, [2012]). There are still some issues in signal processing and ionospheric correction (as described in section 1.2.2) that have to be resolved in order to further improve RO data quality and to extend the application range.

## 12.2 New Developments and Novel Products

The ***new RO products*** to enhance Copernicus for climate change monitoring purposes can be characterised as follows:

- **A** – New signal processing to improve on existing product
- **B** – New product arising from mature understanding of scientific needs
- **C** – New product emerging from latest research

The new products based on GNSS RO measurements are summarised in the following table:

| Product | Novelty | Application | | |
|---|---|---|---|---|
| | | ***Numerical Weather Prediction*** | ***Climatology monitoring and Copernicus*** | ***Atmospheric modelling*** |
| Revised bending angle and retrieved parameters | A | ✓ | ✓ | |
| Multi-satellite climatologies | B | ✓ | ✓ | |

| | | | | |
|---|---|---|---|---|
| Tropopause parameters | B | | ✓ | ✓ |
| QBO/ENSO indices | B | | ✓ | |
| AMSU-type equivalent temperatures | C | ✓ | ✓ | |
| New water vapour profiles | C | ✓ | ✓ | |
| Precipitation profiles | C | ✓ | | ✓ |
| Ducting | C | ✓ | ✓ | ✓ |
| Gravity wave parameters | C | ✓ | ✓ | ✓ |
| Brunt-Väisälä frequency | C | ✓ | ✓ | |

The specific contribution beyond the state of the art with respect to each individual area of study and novel product to be devised is detailed in the following sub-sections.

### 12.2.1 De-noising algorithms

Noise in RO measurements can be divided into three main categories:

1. Thermal noise in the receiver affecting only the uppermost part of retrieved profiles (in a fractional sense).
2. Ionospheric noise and scintillations limiting the performance mostly in the stratosphere and mesosphere.
3. Scintillations and low SNR induced by atmospheric multipath and turbulence in the moist lower troposphere.

Thermal noise is usually small compared to ionospheric noise and scintillations, and is in state-of-the-art retrieval algorithms dealt with by low pass filtering strategies. These strategies also mitigate the effects of ionospheric noise and scintillations, but often, large oscillating residuals are left in the ionospheric corrected bending angles at high altitudes because of initial scintillations in the data that were not handled optimally. Although further processing to refractivity makes use of statistical optimization strategies (e.g., *Gorbunov et al.*, [2002]; *Kuo et al.* [2004]; *Gobiet and Kirchengast* [2004]; *Lohmann* [2005]; *Lauritsen et al.* [2011]), and thereby further smooth high altitude oscillations, errors are still present at high altitudes, and limits the usefulness of the refractivity to be below a certain altitude (on average about 40 km, but can in individual cases be significantly lower).

State-of-the-art algorithms (e.g., *Sokolovskiy et al.* [2009]; *Gorbunov et al.* [2011]) process RO data to bending angles at high altitudes using geometrical optics, i.e., algorithms assuming single ray propagation. However, ionospheric structures can result in multi-path propagation, i.e., the situation where multiple signal paths between the transmitter (GNSS) and the receiver (LEO) are possible at the same time. One especially malicious type of events are tilted sporadic ionospheric E-layers. Although sporadic E occurs at around 90-100 km altitude, they can have significant influence on retrievals at stratospheric altitudes when they are tilted [*Zeng and Sokolovskiy*, 2010].

More advanced processing algorithms, such as Full Spectrum Inversion, FSI [*Jensen et al.*, 2003], Canonical Transform, CT2 [*Gorbunov et al.*, 2006], or Phase Matching [*Jensen et al.*, 2004], are currently used in state-of-the-art processing at lower altitudes. These algorithms take into account the multi-path propagation under the assumption of spherical symmetry. In principle they could also be employed at the higher altitudes, but so far this is not done routinely in leading RO processing centres in either Europe or the US.

One practical reason for this is the generally poorer quality of the L2 signal compared to L1 (since L2 is encrypted, whereas the L1 CA signal is not), which easier results in tracking errors in the L2 phase in the presence of scintillations. Without a good quality L2 signal at high altitudes, it does not make much sense to employ the advanced algorithms. However, with the recently introduced GPS L2C signal, currently tracked by the COSMIC RO mission, and with Galileo signals (though not yet collected routinely for RO) that are not encrypted, such as E5a, the second L-band signal in RO measurements might be good enough to allow for the use of the advanced algorithms at all altitudes.

Thus, advanced algorithms could potentially reduce the noise at high altitudes due to ionospheric scintillations in RO measurements, and will most likely become the future state-of-the-art. Investigation toward this goal is timely and necessary.

As mentioned, advanced algorithms are already routinely used in the lower part of the atmosphere. These algorithms transform the complex signal in the form of phase and amplitude as a function of time into bending angle and transformed amplitude as a function of impact parameter. The transform inherently relies on the assumption of spherical symmetry. If this assumption is fulfilled, the transformed amplitude is in principle constant (numerical inaccuracies may result in minor deviations from a constant in multi-path zones). However, turbulence and other departures from the assumption of spherical symmetry may result in transformed amplitude with large deviations from a constant.

In the lower troposphere, in short intervals (a few meters in impact parameter) where the de-composed transformed amplitude is very small, the computed bending angle (unfiltered) can be wrong by several 100%. Standard, and advanced filtering approaches, reduces these errors to acceptable levels, but at the expense of vertical resolution, as well as possible introduction of biases [*Sokolovskiy et al.*, 2011]. Currently, in state-of-the-art processing algorithms, only the L1 signal is handled by the advanced algorithms since the L2 signal tracking is usually lost in the moist lower troposphere. Extrapolation of the difference between L1 and L2 bending angles below the altitude of L2 tracking is then performed. This allows profile retrievals to lower altitudes, but introduces additional errors.

However, with L2C and other soon-to-come signals, it should be possible to exploit the complementary information of different L-band signals to very low altitudes to significantly reduce the likelihood of large errors (spikes) in the unfiltered ionosphere-corrected bending angle. First steps toward such investigation have been initiated and presented by US scientists (see *Sokolovskiy et al.*, IROWG-2 Workshop, 2 April 2012, Estes Park, Colorado), but warrants further investigation to improve understanding and become a routine part of RO processing with L2C and other modernised GNSS signals.

### 12.2.2 Signal Processing

In order to produce accurate atmospheric profiles from Radio Occultation observations it is well known that dual frequency data from GNSS signals must be available. This is the only way to accurately remove the (small) ionospheric contribution to the overall Excess-phase experienced by the signal during its limb sounding propagation geometry, when neutral atmosphere products are extracted. Up to now, using GPS carrier phase signals, all the operative Radio Occultation payloads suffered of a premature loss of L2 lock during a setting event or a late L2 acquisition during a rising event, both because code-less tracking techniques were normally adopted and, moreover, because half power is used by the GPS signal transmitter to irradiate L2 signals.

Therefore, extrapolation/interpolation techniques which made available L2 signal where it is lost were operatively applied, given the possibility to adopt the standard dual-frequencies techniques to remove the ionospheric contribution. From another side, it is well known that such techniques work well if extrapolation (or interpolation) is necessary only for very small fractions of data. For example, when L2 is definitively lost below 25 km, the extrapolation downward does not work.

It is well known that, in particular for what concerns rising GPS occultation events, GPS L2 signal suffers of late acquisition/tracking issues with respect to L1 signal. Moreover, on setting event, L2 is lost before L1 (even if, in this case, the height at which this happens is nearer to the Earth's surface than the rising case). It may happen also that, for some reasons, missing L2 data create some data gap to the observed time series.

Ionospheric calibration procedures are usually performed applying a linear combination of the L1 and L2 bending angles taken at the same impact parameter [*Vorob'ev and Krasil'nikova*, 1994], even if other techniques has been defined (see for example *Syndergaard* [2000]). The problem is that both signals should be available. In case of data missing, we need to extrapolate/interpolate the signal in some way.

One of the accepted techniques, usually operatively adopted, foresees to correct L1 derived bending angle by the (L1-L2) bending angle extrapolated from above, when both measurement are available [*Kuo et al.*, 2004]. It is demonstrated that this technique well performs when L2 data to be "interpolated/extrapolated" are related to small data gaps, or when L2 rising data are available from 15-20 km Straight Line Tangent Height (SLTA) maximum (presentation given by *EUMETSAT* at the GRAS-SAG 27th meeting, July, 2012). From another side there are some occultation events that suffer of this issue, in particular considering rising observations. One of the RO payload actually flying, the Italian ROSA receiver, has a severe problem in this sense, probably due to the satellite platform on which it is embarked (Oceansat-2).

It was shown, thanks to a recent Visiting Scientist activity at DMI/EUMETSAT that only 10% of rising ROSA L2 observations are available below 20 km [*Notarpietro*, 2012]. Therefore, new strategies for the L2 data extrapolation should be found, in order to try to retrieve the maximum number of information from the actual Radio Occultation satellite missions. One of the possible new techniques was recently developed by I. Culverwell and S. Healy and presented at the IROWG-2 Workshop [*Culverwell and Healy*, 2012]. Another approach we intended to use is to consider some ionospheric models and ray tracing strategies.

A further important quantity for many atmospheric processes is the static stability or vertical temperature stratification of the atmosphere, which is often expressed by the Brunt-Väisälä (or buoyancy) frequency. GPS RO temperature measurements enable the investigation of its fine-scale structure in the tropopause region as the transition zone between low values in the troposphere and high values in the stratosphere and can therefore contribute to a better global observational data basis for the tropopause inversion layer on different temporal and spatial scales [*Schmidt et al.*, 2010a]).

On the other hand buoyancy is a dominant force for vertical atmospheric motions and important for the propagation of atmospheric waves. GWs play an important role in the atmospheric circulation due to the related transport of energy and momentum between different regions in the atmosphere. (e.g., *Steiner and Kirchengast* [2000]; *Tsuda et al*. [2000]; *Fritts and Alexander* [2003]; *de la Torre and Alexander* [2005]). GPS RO temperature data are an excellent data source to derive global GW parameters as temperature amplitude, specific potential energy, and vertical wavelengths (*Tsuda et al.* [2000]; *de la Torre et al.* [2006]; *Schmidt et al.* [2008b]).

Observations from RO offer new opportunities for the assessment of existing observational upper-air records from AMSU. Observations from MSU and AMSU instruments are often used for long-term climate monitoring and trend detection (e.g., *Christy et al*., [2007]; *Mears and Wentz*, [2009]; *Zou et al*., [2009]). Uncertainties in the data and in related upper air trends are large and an issue of continuous investigations.

Intercomparison of RO with AMSU data was performed by *Schrøder et al*. [2003], *Ho et al*. [2007], *Steiner et al*. [2007; 2009b], *Ladstädter et al.* [2011], showing a divergence of the data sets over time. Besides, RO data are useful for the calibration of microwave measurements in the lower stratosphere in order to identify inter-satellite offsets among measurements from different satellites. The RO record enables the computation of synthetic temperatures equivalent to AMSU channels in the UTLS for continuous comparisons and validations.

### 12.2.3 Mitigation of Ionospheric Residual Biases for Climate Purposes

Ionospheric residual biases in RO climatologies need to be mitigated for further improving their error characteristics. Ionospheric residual errors, in particular systematic ones, are important for RO based climate monitoring, since potential decadal scale variability of residual ionospheric systematic errors could pretend short-term trends in RO climatologies of the stratosphere [*Foelsche et al.*, 2008b]. Early results using bending angle data at high altitudes [*Rocken et al.*, 2008] indicated a potential approach to use information contained in the data to remove ionospheric residual errors.

*Danzer et al.* [2013] analysed bending angles from early 2002 until mid-2011 between 65 km and 80 km (impact) altitude. In this altitude range, the bending due to the neutral atmosphere is already small, and systematic differences can be largely explained by un-corrected ionospheric errors. Daytime bending angle values show a clear dependence on the solar cycle, while night time values remain surprisingly stable over the entire time period from high (early 2002) to very low solar activity (2006 to 2010). See also other relevant work in this area, such as *Danzer et al.* [2015], *Liu et al.* [2013; 2015] and *Qu et al.* [2015].

The difference between daytime and night time bending angles, which can therefore be regarded as a good indicator for uncorrected systematic ionospheric errors, reaches up to –0.4 µrad under high solar activity, but generally remains below –0.1 µrad under low solar activity. These results show a way to correct for residual ionospheric errors in the context of climate monitoring, where averages over large numbers of RO profiles are used, without relying on external information about the state of the ionosphere. Correcting daytime measurements by the offset between day and night should than remove the major part of ionospheric residuals with variations on decadal scale.

### 12.2.4 Provision and Evaluation of multi-satellite FCDRs

Thermodynamic atmospheric parameters can be generated by building on the heritage of product algorithms in a first step and by applying improved processing algorithms, i.e., ionospheric correction procedures, and the refinement of error specifications. These improvements are expected to further enhance the accuracy of RO products and to extend the regions and altitudes with RO data of climate quality (see section 1.2.1 for more details).

Data from all available RO missions can be combined for the generation of multi-year multi-satellite RO climatologies of thermodynamic atmospheric parameters including bending angle, refractivity (density), pressure, geopotential height, temperature, and (standard 1DVar) water vapour. These consistent and validated long-term records of RO atmospheric variables will represent FCDRs including ECVs such as air temperature. Error specification will be provided together with FCDRs. Global high vertically resolved FCDRs of atmospheric variables in the UTLS are expected to enhance the Copernicus services on atmosphere and climate monitoring.

Due to the fact that more than one processing centre provides RO products, the quantification of structural uncertainty in the record arising from different processing schemes is essential. Using basically the same raw measurements as input, different processing schemes provide different numbers and distributions of retrieved profiles that flow into climatological fields. Recent studies have shown that trends in RO data products from the CHAMP satellite are essentially independent of retrieval centre and qualify as climate benchmark. Regarding multi-satellite RO climatologies this has yet to be demonstrated and the systematic assessment of structural uncertainty of the provided multi-satellite climate records seems an important aspect.

### 12.2.5 Provision of new value-added Products including Tropopause and Gravity Wave Parameters, ENSO/QBO Indices, and AMSU-equivalent Temperatures

Novel RO products are needed for monitoring and modelling atmospheric variability and change, comprising tropopause parameters, gravity wave parameters, atmospheric indices for the Quasi-Biennial-Oscillation (QBO) and El Niño-Southern Oscillation (ENSO) as well as synthetic temperatures equivalent to channels of the Advanced Microwave Sounding Unit (AMSU). The added value of these products is expected to improve knowledge on atmospheric and climate variability in the UTLS, which is of importance for studies of atmospheric dynamics, climate trend analyses as well as climate modelling. In this respect the added value of RO observations is exploited representing a new information source for Copernicus services.

Tropopause parameters for individual RO profiles and for corresponding monthly-mean zonal-mean climatologies need to be routinely delivered, including error specifications from uneven sampling in space and time. Tropopause height, pressure, temperature, and sharpness will enable to gain valuable information on the structure of the tropopause region, e.g. the tropical tropopause layer and troposphere-stratosphere exchange.

Further important quantities for the investigation of the fine structure of the tropopause and inversion layers, of atmospheric processes, and wave propagation in the UTLS. RO observations will be exploited for routine estimation of the Brunt-Väisälä (or buoyancy) frequency and of global gravity wave (GW) parameters including temperature amplitude, specific potential energy, and vertical wavelengths are needed.

Novel atmospheric ENSO indices in the troposphere and QBO indices in the stratosphere are needed for improving information on the natural variability patterns in the UTLS, which is of high interest e.g., for atmospheric dynamics or climate trend detection. Due to the high vertical resolution of RO data the detailed vertical structure of these signals can be investigated and new information on the most significant modes of natural climate variability in the tropical UTLS can be derived from observations.

Observations from AMSU instruments are often used for long-term climate monitoring and trend detection. Uncertainties in the data and in related upper air trends are large and an issue of continuous investigations. The AMSU is a radiometer measuring the Earth's microwave emission in the oxygen absorption band in different channels. Due to the coarse vertical resolution layer average brightness temperatures are provided and different height regions are sampled by choosing different channels. Synthetic layer-average brightness temperatures from RO will be provided by applying a radiative transfer model.

Since RO data quality is best in the UTLS region, the focus will be on the lower stratospheric channels for the provision of AMSU-equivalent temperatures, i.e., Temperature Lower Stratosphere (TLS), and possibly neighbouring channels. The routine provision of AMSU-equivalent temperatures from RO will enable continuous comparison and validation of upper-air satellite records.

The continuous data stream from the CHAMP satellite provided the first opportunity to generate RO-based atmospheric fields [*Foelsche et al.*, 2008]. Monthly- and seasonal-mean zonal-mean climatologies for different RO missions are currently provided for refractivity, dry pressure, dry geopotential height, and dry temperature. Due care was given to the analysis and provision of corresponding error estimates [*Scherllin-Pirscher et al*., 2011b]. A range of studies analysed the climate monitoring utility of RO data (e.g., *Foelsche et al*., [2009a; b]; *Lackner et al*., [2011]; *Steiner et al*., [2009a; 2012]; *Schmidt et al*., [2005; 2008a; 2010]).

Beyond current available RO records, we will provide consistent and validated long-term multi-satellite RO FCDRs of high vertical resolution for atmosphere and climate monitoring services. Thermodynamic atmospheric parameters include ECVs such as air temperature and bending angle, and further standard RO variables refractivity, pressure, and geopotential height. Furthermore, new water vapour products will be developed and its climate quality will be evaluated.

Knowledge on atmospheric and climate variability is of importance for studies of atmospheric dynamics, climate trend analyses as well as climate modelling. The most significant modes of natural climate variability in the tropical troposphere are ENSO and the QBO. Due to the high vertical resolution of RO data the detailed vertical structure of these signals can be investigated (e.g., *Schmidt et al*., [2005]; *Steiner et al*. [2009]; *Schmidt et al*. [2010a]; *Scherllin-Pirscher et al.* [2012]).

Current QBO indices are available from 30/50 hPa winds. Current ENSO indices are available from surface measurements only. The RO records will be used for the provision of novel atmospheric ENSO indices in the troposphere and QBO indices in the stratosphere.

Furthermore, RO can be exploited to gain valuable information on the structure of tropopause regions (e.g., *Schmidt et al*., [2004]; *Gobiet et al*. [2005]; *Schmidt et al*. [2005]; *Borsche et al*. [2007]; *Schmidt et al*. [2008a]), especially on the tropical tropopause layer which is a topic of current active research. Tropopause parameters including information on multiple tropopauses [*Schmidt et al*., 2006] will be provided based on the RO record for individual profiles in terms of tropopause height, pressure, temperature, and sharpness. Corresponding monthly-mean zonal-mean climatologies will be generated, including error specifications from uneven sampling in space and time.

### 12.2.6 Provision and Algorithm Development for new Water Vapour Product

In the traditional 1Dvar approach to solve the inherent ambiguity between temperature and moisture in RO measurements, the observations (refractivity) and the background (e.g., ECMWF forecast fields) are weighted according to assumed observation and background error co-variances. This results in temperature, humidity, and pressure profiles that in principle can be considered an optimal solution given the observations and the best available a priori knowledge.

However, such profiles will generally be inconsistent with the observations in that the derived temperature, humidity, and pressure do not correspond to the observed refractivity via the equation connecting these variables (e.g., the Smith-Weintraub formula). An alternative approach, currently applied to COSMIC data at UCAR in the US, is to give much more weight to the observations than to the background. In this way the physical relation between the solution and the observed refractivity is preserved to a high degree. Such an approach still includes information from ECMWF fields to separate out the meteorological variables in the moist troposphere, but it seeks to minimize the influence from the ECMWF fields and it preserves most of the information coming from the observations.

Going a step further, it should be possible to develop the theory for an approach where the observations in principle have infinite weight, and where the NWP model in principle has zero weight. However, the model would still provide the information on the relative contributions of temperature and humidity to the refractivity (dry and wet terms), based on its representation of these variables and their error co-variances. Additional information would enter through the assumption of hydrostatic equilibrium and the equation of state. The solution based on such an approach would be fully consistent with the refractivity via the refractivity equation.

Since RO data in itself does not contain direct information on the temperature and humidity, it should be possible to use ECMWF analyses (where the specific RO profile presumably has already been assimilated) without including the information from the RO data twice (because the information about the dry and wet contributions to refractivity that the ECMWF analysis will have, cannot have come from assimilating the occultation). This can be verified theoretically, and it means that the method can use the best available information about the relative contributions of temperature and humidity to separate out these variables (this opposed to the traditional 1Dvar approach which is based on forecasts so that the RO information is not used twice).

The water vapour (and temperature) derived via such an approach would be extremely valuable for applications where it is important to preserve the high vertical resolution in the data (e.g., in atmospheric process studies, Biondi et al. [2012]) and where unnecessary information from an NWP model should be avoided (e.g. for climate monitoring using independent data sources).

### 12.2.7 Development of Precipitation Profile retrieval from non-polarimetric RO Data

As far as the retrieval of precipitation profiles from standard Radio Occultation observations is concerned, it has to be noted that this is a quite unexplored field. There is evidence in the recent literature of a possible sensitivity of SNR profiles derived by standard Radio Occultation observations and precipitation involving high rain rates. E. Cardellach et al. [2010] demonstrated that an extra attenuation due to rain (and not to simply clouds or water vapour) is visible, on average, on the amplitude of Radio Occultation signals when the ray path crosses high precipitation area.

Historical and standard Radio Occultation observations were performed using a right hand circularly polarized antenna, allowing only co-polar measurements. In order to carried out such research, we will use Radio Occultation observations collected mainly on board the METOP and the COSMIC satellite missions co-located with precipitation observations taken by the unique TRMM (Tropical Rainfall Measurement Mission) satellite radar meteorological system. This will hopefully allow to define a quite interesting dataset of co-located observations.

Second aspect of the proposed activity is to help in the validation of Radio Occultation derived precipitation products based on the challenging polarimetric observations provided by IEEC partner. In this case, we can perform a validation activity using both data from the mentioned TRMM mission, data from standard ground-based radar meteorological systems and data from rain gauges network, maybe available in the Radio Occultation ray perigee areas, for selected case studies. Such data will be provided for example by MeteoSwiss (see the Letter of Intent attached to the proposal), which are going to operate the new fourth generation radar-meteo network, made by four powerful C-Band polarized and Doppler radar systems.

Within this sub-task we wish to evaluate whether precipitation profiles can be retrieved considering standard Radio Occultation non-polarimetric observations or not. In order to carry out such research, we will use Radio Occultation observations collected mainly on board the METOP and the COSMIC satellite missions, co-located with precipitation profile observations taken by the unique TRMM (Tropical Rainfall Measurement Mission) satellite radar meteorological system. This will hopefully allow defining a quite interesting dataset of co-located precipitation profiles data. The analysis will be performed with the following scheme.

- a dataset of rainy observations (characterized by different rainfall rates and amounts) taken by satellite-based radar meteorological system on-board the TRMM mission will be downloaded
- co-located COSMIC and METOP RO SNRs (and phases) observations will be identified and analysed, in order to highlight some impact or sensitivity level of SNR to precipitation fields
- co-located, along the same line-of-sight ground-based radar meteorological observations will be considered if available (some links with radar-meteorological data providers will be defined)
- RO precipitation profiles will be tentatively evaluated considering SNRs data time series
- RO precipitation profiles will be compared with co-located TRMM data or with co-located ground-based radar-meteorological observations (if any)

### 12.2.8 Development of Precipitation Profile Retrieval from PAZ Satellite polarimetric-RO Data

L-band signals, such those of the GNSS, are weakly attenuated by precipitation, they do penetrate through heavy rain, and are thus called "all weather" signals. However, moderate and heavy precipitation also introduce features in the phase of the electromagnetic carrier, while GNSS are systems that measure phase delays with high precision. Preliminary studies shown that polarimetric phase-shifts (different phase delay) between H and V linear polarizations might present rain-induced signatures above the GNSS detectability threshold.

Once in orbit, PAZ pol-RO data will allow the investigation and exploitation of this concept. If successful, the simultaneous acquisition and perfect collocation of standard thermodynamic RO profiles together with moderate to heavy precipitation RO profiles might represent an unprecedented source of information to better understand these extreme events. In turn, this might improve their modelling and the assessment of heavy rain statistics in future climatic scenarios.

Recent theoretical studies about the sensitivity of the polarimetric GNSS RO signals to precipitation events show that moderate to heavy rain induce a linear-polarimetric phase shift (phase delay difference between the two linear polarizations) above the GNSS detectivity thresholds. The studies, performed by members of the consortium, presented in the *COSMIC User Workshop 2012* (Boulder, CO, USA, October 2012) but unpublished yet, also show weak polarimetric SNR signatures and large ambiguity between rain rate and optical length across the precipitation cell. The theoretical models implemented for such study will be used, together with the real PAZ pol-RO data, find the best algorithms to:

1. detect the presence of rain;
2. provide an overall equivalent rain rate and/or precipitation cell size; or a combined pseudo-parameter;
3. to break the ambiguity between rain rate and cell size using first other GNSS pol-RO observables (absolute SNR of one of the polarizations ratio between both linear pol-SNR), and finally using external data, and/or assimilation experiments. Precise knowledge of the PAZ RO antenna patterns will be acquired first, using both the anechoic chamber measurements conducted before the payload assembly, and the accumulated measurement of rain-free observations along the commissioning phase.
4. Finally, the retrieval of vertical structures will also be attempted, using the well-known vertical resolution of the RO observations

### 12.2.9 Further New Products

The results of the analysis performed on WP2 will be translated into the identification of the capability and effectiveness of a RO payloads to give information also on rainfall rate or precipitation profile considering standard and/or polarimetric RO observations. Issues, if any, will be addressed, and possible solutions at the level of signal processing/signal characterization will be suggested. Possible future use of such kind of observation will be also identified, in order to make this technique a new observation technique to be implemented in the new generation of RO satellite missions.

Additional products could be in the domains of space weather and ionised/neutral atmosphere coupling.

## 12.3 Outreach Needs

RO is an established observation technique in global NWP; specific additional outreach in this area is not required. The currently available information on several monitoring pages of NWP centres, and the collected NWP setups on the IROWG website "RO data use in operational NWP systems" [*IROWG-NWP*] should be maintained and include new NWP models making use of RO data.

The use of RO for climate monitoring purposes will need further outreach to relevant organisations and groups, such as e.g. the IPCC. The full use of this data in re-analysis and climate models needs to be pursued and presented to these groups and organisations.

Provision of data in formats more readily available to the climate community need to be pursued (e.g. by using the Obs4MIPS (Observations for Model Intercomparisons Project) data format).

The use of RO data in regional NWP models is limited and more outreach is needed here. Regarding EPS-SG, this community can use the established global mission products, but it also needs to be made aware of the additional regional mission products of EPS-SG, these come with a better timeliness (but are not available globally). Specific operators/tools that allow the assimilation of RO data into regional models will help here too (refractivity can already be assimilated into regional models, but bending angles generally need a model top that is higher than the one of current regional models).

The possibilities of the local mission of EPS-SG should also be further assessed with the scientific community. Although level 1b or 2 RO products are not produced, any local receiving station can receive the raw RO data directly from the satellite and potentially process it further locally. This local mission is available in real time, but for RO the observation is generally a few thousand km away from the local receiving station, while nadir sounders provide information above the station.

The extension of the EPS-SG RO data coverage to include the ionosphere will need to be conveyed to the relevant communities, the use of RO data for ionospheric research, monitoring, and assimilation is however already established.

Applicable to all areas identified above, effective outreach includes:

- presentations at conferences and workshops on latest results;
- development of improved NWP operators and tools to maximize the impact of RO;
- production of RO based new products;
- publication of articles, scientific reports;
- information exchange through visiting scientist programs;
- up to date websites with relevant information/links to further information/documents;
- up to date websites with operational processing results, including monitoring statistics;
- provision of visualization / reading / processing tools, allowing easy access for new-comers;
- invitation of “RO external” scientists to IROWG and other workshops.

# APPENDIX A REFERENCES

Aarons, J. (1982), Global morphology of ionospheric scintillations, Proc IEEE, 70(4), 360-378

Alexander, M. J., and K. H. Rosenlof (1996), Nonstationary gravity wave forcing of the stratospheric zonal mean wind, J. Geophys. Res., 101(D18), 23,465–23,474, doi:10.1029/96JD02197

Angerer, B., F. Ladstädter, B. Scherllin-Pirscher, M. Schwärz, A. K. Steiner, U. Foelsche, and G. Kirchengast (2017), Quality Aspects of the Wegener Center Multi-Satellite GPS Radio Occultation Record OPSv5.6, Atmos. Meas. Tech., 10, 4845–4863, doi:10.5194/amt-10-4845-2017

Angling, M. J. (2008), First assimilations of COSMIC radio occultation data into the Electron Density Assimilative Model (EDAM), Ann. Geophys., 26(2), 353–359

Angling, M. J., and N. K. Jackson-Booth (2011), A short note on the assimilation of collocated and concurrent GPS and ionosonde data into the Electron Density Assimilative Model, Radio Sci., 46(4)

Anthes, R. A. (2011), Exploring Earth's atmosphere with radio occultation: contributions to weather, climate and space weather, Atmos. Meas. Tech., 4(6), 1077–1103, doi:10.5194/amt-4-1077-2011

Aparicio, J. and G. Deblonde (2008), Impact of the assimilation of CHAMP refractivity profiles in Environment Canada global forecasts, Mon. Wea. Rev., 136, 257–275

Aparicio J.M., E. Cardellach, and H. Rodríguez (2016), Information content in reflected signals during GPS Radio Occultation observations, submitted to JGR-Atmospheres, May

Ao C.O., D.E Waliser., S.K. Chan, J-L. Li, B. Tian, F. Xie and A.J. Mannucci (2012), Planetary boundary layer heights from GPS radio occultation refractivity and humidity profiles, Journal Geophys Res, 117, D16117

Ao, C.O. et al. (2015), Evaluation of CMIP5 upper troposphere and lower stratosphere geopotential height with GPS radio occultation observations, J. Geophys. Res. Atmos., 120, doi:10.1002/2014JD022239.

Aragon-Angel, A., Y.A. Liou, C.C. Lee, B.W. Reinisch, M. Hernandez-Pajares, M. Juan and J. Sanz (2011), Improvement of retrieved FORMOSAT3/COSMIC electron densities validated by ionospheric sounder measurements at Jicamarca. Radio Science, 46(5)

Basu, S., E. MacKenzie, and S. Basu (1988), Ionospheric constraints on VHF/UHF communications links during solar maximum and minimum periods, Radio Sci, 23(3), 363-378

Bates, J. J., and J. L. Privette (2012), A maturity model for assessing the completeness of climate data records, Eos Trans. AGU, 93(44), 441–441, doi:10.1029/2012EO440006

Bauer P., G. Radnóti, S. Healy, and C. Cardinali (2013), GNSS radio occultation constellation observing system experiments, Mon. Wea. Rev., e-View doi: http://dx.doi.org/10.1175/MWR-D-13-00130.1

Beutler, G., M. Rothacher, S. Schaer, T. A. Springer, J. Kouba, and R. E. Neilan (1999), The International GPS Service (IGS): An Interdisciplinary Service in Support of Earth Sciences, Adv. Space. Res., 23(4), 631–635

Beyerle G., K. Hocke, J. Wickert et al. (2002), GPS radio occultation with CHAMP: A radio holographic analysis of GPS signal propagation in the troposphere and surface reflections, J. Geophys. Res., 107(D24), 4802, doi:10.1029/2001JD001402

Biondi, R., T. Neubert, S. Syndengaard and J. Nielsen (2011), Measurements of the Upper Troposphere and Lower Stratosphere during Tropical Cyclones using the GPS Radio Occultation Technique, Adv. Space Res., 47, 348-355, doi:10.1016/j.asr.2010.05.031

Biondi, R., W. Randel, S.-P. Ho, T. Neubert and S. Syndergaard (2012), Thermal structure of intense convective clouds derived from GPS radio occultations, Atmos. Chem. Phys., 12, 5309-5318, doi:10.5194/acp-12-5309-2012

Biondi, R., S.-P. Ho, W. Randel, T. Neubert and S. Syndergaard (2013), Tropical cyclone cloud-top height and vertical temperature structure detection using GPS radio occultation measurements, J. Geophys. Res., 118, 1-13, doi: 10.1002/jgrd.50448

Biondi, R., A.K. Steiner, G. Kirchengast and T. Rieckh (2015), Characterization of thermal structure and conditions for overshooting of tropical and extratropical cyclones with GPS radio occultation, Atm. Chem. Phys., 15, 5181-5193, doi:10.5194/acp-15-5181-2015

Biondi, R., A.K. Steiner, G. Kirchengast, H. Brenot, and T. Rieckh (2017): Supporting the detection and monitoring of volcanic clouds: a promising new application of Global Navigation Satellite System radio occultation, Adv. Space Res., 60(12), 2707–2722, doi:10.1016/j.asr.2017.06.039

Bodas-Salcedo, A., M. Webb, S. Bony, H. Chepfer, J. Dufresne, S. Klein, Y. Zhang, R. Marchand, J. Haynes, R. Pincus and V. John, (2011), COSP: Satellite simulation software for model assessment. Bull. Amer. Meteor. Soc., 92, 1023–1043, doi: 10.1175/2011BAMS2856.1

Bojinski, S., M. Verstraete, T.C. Peterson, C. Richter, A. Simmons and M. Zemp (2014), The concept of Essential Climate Variables in support of climate research, applications, and policy, Bull. Amer. Meteor. Soc., doi:10.1175/BAMS-D-13-00047.1.

Boniface, K., J.M. Aparicio, and E. Cardellach (2011), Meteorological information in GPS-RO reflected signals, Atmos. Meas. Tech., 4, 1397-1407, doi:10.5194/amt-4-1397-2011

Borsche, M., G. Kirchengast, and U. Foelsche (2007), Tropical tropopause climatology as observed with radio occultation measurements from CHAMP compared to ECMWF and NCEP analyses, Geophys. Res. Lett., 34, L03702, doi:10.1029/2006GL027918

Bock H., Jäggi A., Meyer U., Dach R., Beutler G. (2011); Impact of GPS antenna phase center variations on precise orbits of the GOCE satellite, Adv Space Res 47(11):1885-1893

Borsche, M., G. Kirchengast, and U. Foelsche (2007), Tropical tropopause climatology as observed with radio occultation measurements from CHAMP compared to ECMWF and NCEP analyses, Geophys. Res. Lett., 34, L03702, doi:10.1029/2006GL027918.

Brunner, L., A.K. Steiner, B. Scherllin-Pirscher, and M.W. Jury (2016), Exploring atmospheric blocking with GPS radio occultation observations, Atmos. Chem. Phys., 16(7), 4593–4604, doi:10.5194/acp-16-4593-2016

Brunner, L., and A.K. Steiner (2017), A global perspective on atmospheric blocking using GPS radio occultation – one decade of observations, Atmos. Meas. Tech., 10, 4727-4745, doi:amt-10-4727-2017

Buresova, D., V. Krasnov, Ya. Drobzheva, J. Lastovicka, J. Chum, et al. (2007), Assessing the quality of ionogram interpretation using the HF Doppler technique, Annales Geophysicae, European Geosciences Union, 25 (4), pp.895-904

Bust, G.S. (2006), Global 3D imaging of the August 19-20 2006 storm using COSMIC data, in COSMIC data users workshop, Boulder, CO

Bust, G.S., and C.N. Mitchell (2008), History, current state, and future directions of ionospheric imaging, Rev. Geophys., 46(RG1003), 1–23, doi:10.1029/2006RG000212

Bust, G.S., T.W. Garner, and T.L. Gaussirian (2004), Ionospheric Data Assimilation Three-Dimensional (IDA3D): A global, multisensor, electron density specification algorithm, J Geophys Res, 109(A11312), doi:doi:10.1029/2003JA010234

Cardellach E., C.O. Ao, M. de la Torre Juárez, G.A. Hajj (2004), Carrier phase delay altimetry with GPS reflection/occultation interferometry from low Earth orbiters, Geophysical Research Letters, 31, pp. 10402-+, May, doi:10.1029/2004GL019775

Cardellach E., Oliveras, S., Rius, A. (2008), Applications of the reflected signals found in GNSS radio occultation events, ECMWF Proceedings: GRAS SAF Workshop on Applications of GPSRO Measurements, ECMWF, Shinfield Park, Reading, Berks RG2 9AX, England, June, ECMWF

Cardellach E., Fabra, F., Rius, A., S. Pettinato, S. D'Addio (2012), Characterization of Dry-snow Sub-structure using GNSS Reflected Signals, Remote Sensing Environment, 124, pp. 122-134, 2012, 10.1016/j.rse.2012.05.012

Cardellach E., Tomas, S., Oliveras, S., Padullés, R., Rius, A., De la Torre-Juárez, M., Turk, F.J., Ao, C.O., Kursinski, E.R., Schreiner, B., et al, (2014), Sensitivity of PAZ LEO Polarimetric GNSS Radio-Occultation Experiment to Precipitation Events, IEEE Transactions on Geoscience and Remote Sensing, 53, 1, pp. 190 - 206, 2014, 10.1109/TGRS.2014.2320309

Cardellach E., J.M. Aparicio, H. Rodríguez (2015), ROM-043: Preliminary assessment report on potential atmospheric products based on RO reflection inversion, Feb. 2015, Ref. SAF/ROM/IEEC/OPR/ROM-043

Cardellach E. and S. Oliveras (2016), Assessment of a potential reflection flag product, ROM SAF Report N.23, Ref. SAF/ROM/METO/REP/RSR/023. http://www.romsaf.org/general-documents/rsr/rsr_23.pdf

Carreno-Luengo H., A. Camps, I. Perez-Ramos, G. Forte, R. Onrubia and R. Díez (2013), ³Cat-2: A P(Y) and C/A GNSS-R experimental nano-satellite mission, 2013 IEEE International Geoscience and Remote Sensing Symposium - IGARSS, Melbourne, VIC, 2013, pp. 843-846. doi: 10.1109/IGARSS.2013.6721290

Chang, F. L., P. Minnis, J.K. Ayers, M.J. McGill, R. Palikonda, D.A. Spangenberg, W.L. Smith Jr. and C.R. Yost (2010), Evaluation of satellite-based upper troposphere cloud top height retrievals in multilayer cloud conditions during TC4, J. Geophys. Res., 115, D00J05, doi:10.1029/2009JD013305

Chatre, E. (2016), Galileo Program Status, ION GNSS+ 2016 conference, Portland, Oregon

Coleman C. J. (2016), Analysis and Modeling of Radio Wave Propagation, Cambridge University Press

Convention (1991), EUMETSAT Convention, EUM/C/Res./XXXVI, Date: 5 June 1991

Cucurull, L. (2010), Improvement in the use of an operational constellation of GPS radio occultation receivers in weather forecasting, Weather and Forecasting, 25. 749–767

Cucurull, L., and J.C. Derber (2008), Operational implementation of COSMIC observations into NCEP's global data assimilation system, Wea. Forecasting, 23, 702-711, doi:10.1175/2008WAF2007070.1

Danzer, J., B. Scherllin-Pirscher, and U. Foelsche (2013), Systematic residual ionospheric errors in radio occultation data and a potential way to minimize them, Atmos. Meas. Tech., 6, 2169-2179, doi:10.5194/amt-6-2169-2013

Danzer, J., S.B. Healy, and I.D. Culverwell (2015), A simulation study with a new residual ionospheric error model for GPS radio occultation climatologies, Atmos. Meas. Tech., 8, 3395-3404, doi:105194/amt-8-3395-2015

Le Dimet, F.-X., and O. Talagrand (1986), Variational algorithms for analysis and assimilation of meteorological observations: theoretical aspects, Tellus, 38A, 97–110

Eddy, A. (1967), The Statistical Objective Analysis of Scalar Data Fields, J. Appl. Meteorol., 6, 597–609

EPS-SP (1998), Report of the GRAS SAG: The GRAS Instrument on Metop, VR/3021/PI; EPS/MIS/TN/97805, 4. May

EURD (2016), EPS-SG End User Requirements Document [EURD], EUM/PEPS/REQ/09/0151, v4

Egido A., S. Paloscia, E. Motte, L. Guerriero, N. Pierdicca, M. Caparrini, E. Santi, G. Fontanelli, and N. Floury (2014), Airborne GNSS-r polarimetric measurements for soil moisture and above-ground biomass estimation, Selected Topics in Applied Earth Observations and Remote Sensing, vol. 7, no. 5, pp. 15221532

Falcone, M. (2016), Galileo System Status, Proc. ION GNSS+ 2016 conference, Portland, Oregon, September

FedRadNavPlan (2014), Federal Radionavigation Plan Section 3.2.8, http://ntl.bts.gov/lib/55000/55100/55108/20150526_Final_Signed_2014_FRP.pdf

Flechter K., M. Rast and M. Kern, Eds. (2015), ESA's Living Planet Programme: Scientific Achievements and Future Challenges, ESA, SP1329/2, ISBN 978-92-9221-427-2 (2 volumes). http://esamultimedia.esa.int/multimedia/publications/SP-1329_2/

Foelsche, U., M. Borsche, A. K. Steiner, A. Gobiet, B. Pirscher, G. Kirchengast, J. Wickert, and T. Schmidt (2008a), Observing upper troposphere–lower stratosphere climate with radio occultation data from the CHAMP satellite, Clim. Dyn., 31, 49–65, doi:10.1007/s00382-007-0337-7

Foelsche, U., G. Kirchengast, A.K. Steiner, L. Kornblueh, E. Manzini, and L. Bengtsson (2008b), An observing system simulation experiment for climate monitoring with GNSS radio occultation data: Setup and testbed study, J. Geophys. Res., 113, D11108, doi:10.1029/2007JD009231

Foelsche, U., B. Pirscher, M. Borsche, G. Kirchengast, and J. Wickert (2009), Assessing the climate monitoring utility of radio occultation data: From CHAMP to FORMOSAT-3/COSMIC, Terr. Atmos. Oceanic Sci., 20, doi: 10.3319/TAO.2008.01.14.01(F3C)

Foelsche, U., B. Scherllin-Pirscher, F. Ladstädter, A. K. Steiner, and G. Kirchengast (2011), Refractivity and temperature climate records from multiple radio occultation satellites consistent within 0.05%, Atmos. Meas. Tech., 4(9), 2007–2018, doi:10.5194/amt-4-2007-2011

Forte, B., C. Coleman, S. Skone, I. Häggström, C. Mitchell, F. Da Dalt, T. Panicciari, J. Kinrade, and G. Bust (2016), Identification of scintillation signatures on GPS signals originating from plasma structures detected with EISCAT incoherent scatter radar along the same line of sight, J. Geophys. Res. Space Physics, 122, doi:10.1002/2016JA023271

Foti G., C. Gommenginger, P. Jales, M. Unwin, A. Shaw, C. Robertson, and J. Roselló (2015), Spaceborne GNSS reflectometry for ocean winds: First results from the UK TechDemoSat-1 mission, Geophys. Res. Lett., 42, 54355441, doi:10.1002/2015GL064204

Fridman, S. V, L.J. Nickisch, and M. Hausman (2009), Personal-computer-based system for real-time reconstruction of the three-dimensional ionosphere using data from diverse sources, Radio Sci., 44(RS3008), doi:10.1029/2008RS004040

Fritts, D. C., and M. J. Alexander (2003), Gravity wave dynamics and effects in the middle atmosphere, Rev. Geophys., 41(1), 1003, doi:10.1029/2001RG000106

Gandin, L. (1963), Objective analysis of meteorological fields (Leningrad: Gridromet). English translation (Jerusalem: Israel Program for Scientific Translation), 1965.

Garcia, R. R., and B.A. Boville (1994), "Downward control" of the mean meridional circulation and temperature distribution of the polar winter stratosphere, J. Atmos. Sci., 51, 2238–2245

Garcia-Fernandez, M., M. Hernandez-Pajares, J.M. Juan, J. Sanz (2003), Improvement of ionospheric electron density estimation with GPSMET occultations using Abel inversion and VTEC information, Journal of Geophysical Research: Space Physics 108.A9

Garcia-Fernandez, A., M. Hernandez-Pajares (2016), Ionospheric data set description document, Tech. report of ROPE project of EUMETSAT, (reference WP1 D3 dataset description document)

Garner, T. W., T.L. Gaussiran II, B.W. Tolman, R.B. Harris, R.S. Calfas and H. Gallagher (2008), Total electron content measurements in ionospheric physics, Adv. Space. Res., 42(4), 720–726

Garratt J.R. (1993), Sensitivity of climate simulations to land-surface and atmospheric boundary layer treatments — a review, Journal Clim., 6, 419–448

Garrison J.L., S.J. Katzberg and M.I. Hill (1998), Effect of sea roughness on bistatically scattered range coded signals from the Global Positioning System, Geophysical Research Letters, Vol. 25, No.13, Pages 2257-2260, July 1

Gaussiran, T., D. Rainwater, R. S. Calfas and M. S. Pierce (2011), Ensemble background modeling for TRIPL-DA, in AGU Fall Meeting Abstracts, vol. 1, p. 1897

GARCA Team (2016): Cardellach E., C. Gommenginger, G. Foti, H. Park, A. Sousa, M. Semmling and J. Wickert, GARCA WP30 TN4 Data Acquisition and Analysis Report, TN4 of ESA tender AO1-7850-14, Ref. GARCA-TN4, version 1, 22 April 2016

GCOS (2006), Systematic observation requirements for satellite-based products for climate, GCOS-107, WMO/TD No. 1338

GCOS (2010a), Guidelines for the generation of datasets and products meeting GCOS requirements, GCOS-143, WMO/TD No. 1530

GCOS (2010b), Implementation plan for the global observing system for climate in support of the UNFCC, GCOS-138, WMO/TD No. 1523

GCOS (2011), Systematic observation requirements for satellite-based data products for climate, GCOS-154

Geller M.A. et al., (2013), A comparison between gravity wave momentum fluxes in observations and climate models, J. Clim., 26, 6383–6405, doi:10.1175/JCLI-D-12-00545.1

GEROS ESA Team (2015), GNSS Reflectometry, Radio Occultation and Scatterometry onboard ISS (GEROS-ISS) SYSTEM REQUIREMENTS DOCUMENT, Ref.TEC-ETP/2013.202/MMN, Issue 2, Revision 4, 10/09/2015

Gleisner H. (2010), Latitudinal binning and area-weighted averaging of irregularly distributed radio occultation data, GRAS SAF Report 10 (2010); available from http://www.romsaf.org

Gleisner, H., P. Thejll, B. Christiansen and J.K. Nielsen (2015), Recent global warming hiatus dominated by low-latitude temperature trends in surface and troposphere data, Geophys. Res. Lett., 2014GL062596, doi:10.1002/2014GL062596

Gobiet, A., U. Foelsche, A.K. Steiner, M. Borsche, G. Kirchengast and J. Wickert (2005), Climatological validation of stratospheric temperatures in ECMWF operational analyses with CHAMP radio occultation data, Geophys. Res. Lett., 32, L12806, doi:10.1029/2005GL022617

Gobiet A. and G. Kirchengast (2004), Advancements of Global Navigation Satellite System radio occultation retrieval in the upper stratosphere for optimal climate monitoring utility, J. Geophys. Res., 109, D24110, doi:10.1029/2004JD005117

Gorbunov M. E. (2000), Canonical transform method for processing radio occultation data in the lower troposphere, Radio Science, 37(5), pp. 9-19-10, doi: 10.1029/2000RS002592

Gorbunov M. E. (2002), Ionospheric correction and statistical optimization of radio occultation data, Radio Science, 37(5), 1084, doi:10.1029/2000RS002370

Gorbunov M.E. and K.B. Lauritsen (2004), Analysis of wave fields by Fourier integral operators and their application for radio occultations. Radio Science, 39, RS4010, doi:10.1029/2003RS002971

GPSW2014-GLOK2 (2014), GPS World First Launch of GLONASS-K2 Satellite Planned for 2018, http://gpsworld.com/first-launch-of-glonass-k2-satellite-planned-for-2018/

GPSW2015-BDS3 (2015), GPS World China Launches First of Next-Gen BeiDou Satellites, http://gpsworld.com/secretive-beidou-launch-unconfirmed/

GPSW2015-GLOK1 (2015), GPS World GLONASS-K1 to Replace an Existing GLONASS-M in Six Months http://gpsworld.com/glonass-k1-to-replace-an-existing-glonass-m-in-six-months/

GPSW2015-GPS, GPS World Upcoming satellite launches (last accessed 2015/06/04), http://gpsworld.com/resources/upcoming-gnss-satellite-launches/

GPSW2016-Budget (2016), September budgeting surprises: Scarcity or surplus?, http://gpsworld.com/september-budgeting-surprises-scarcity-or-surplus/

Guo P., Y-H. Kuo , S.V. Sokolovskiy and D.H. Lenschow (2000), Estimating Atmospheric Boundary Layer Depth using COSMIC Radio Occultation Data, Terrestrial, Atmospheric and Oceanic Sciences, 11, 1, 53–114

Gulyaeva, T. and D. Bilitza (2012), Towards ISO standard earth ionosphere and plasmasphere model. In: Larsen, Ryan J. (Ed.), New Developments in the Standard Model. Nova Science Publishers Inc., pp. 1 48, ISBN: 978-1-61209-989-7

Haralambous, H. and C. Oikonomou (2013), Study of topside electron density profiles obtained by COSMIC satellites and an ionosonde over Cyprus during a four year period, IEEE Geoscience and Remote Sensing Symposium (IGARSS), 21-26 July 2013, Melbourne, Australia

Harnisch, F., S.B. Healy, P. Bauer and S.J. English, (2013), Scaling of GNSS Radio Occultation Impact with Observation Number Using an Ensemble of Data Assimilations. Mon. Wea. Rev., 141, 4395–4413. doi: http://dx.doi.org/10.1175/MWR-D-13-00098.1

Hauschild A., O. Montenbruck and P. Steigenberger (2013); Short-term analysis of GNSS clocks. GPS Solutions, 17(3):295307, http://link.springer.com/article/10.1007%2Fs10291-012-0278-4

He, W., S. Ho, H. Chen, X. Zhou, D. Hunt and Y.-H. Kuo (2009), Assessment of radiosonde temperature measurements in the upper troposphere and lower stratosphere using COSMIC radio occultation data, Geophys. Res. Lett., 36(17), L17807, doi:10.1029/2009GL038712

Healy S. and J.R. Eyre (2000), Retrieving temperature, water vapor and surface pressure information from refractiveindex profiles derived by radio occultation: A simulation study, Quart. J. Roy. Meteorol. Soc., 126, 16611683

Healy, S.B. and J.-N. Thépaut (2006), Assimilation experiments with CHAMP GPS radio occultation measurements, Quart. J. Roy. Meteorol. Soc., 132, 605–623

Healy, S.B., J.R. Eyre, M. Hamrud and J.-N. Thepaut (2007), Assimilating GPS radio occultation measurements with two-dimensional bending angle observation operators, Q.J.R. Meteorol. Soc., 133(October), 1213–1227, doi:10.1002/qj.63

Healy, S. (2015), The use of the GPS radio occultation reflection flag for NWP applications, ROM-SAF Report N.22, Ref. SAF/ROM/METO/REP/RSR/022. http://www.romsaf.org/general-documents/rsr/rsr_22.pdf

Healy, S.B. and I.D. Culverwell (2015), A modification to the standard ionospheric correction method used in GPS radio occultation, Atmos. Meas. Tech., 8(8), 3385–3393, doi:10.5194/amt-8-3385-2015

Hernández-Pajares, M., J.M. Juan and J. Sanz (1999), New approaches in global ionospheric determination using ground GPS data, J. Atmos. Solar-Terr. Phys., 61, 1237–1247

Ho, S.-P., Y.-H. Kuo, Z. Zeng and T.C. Peterson (2007), A comparison of lower stratosphere temperature from microwave measurements with CHAMP GPS RO data, Geophys. Res. Lett., 34, L15701, doi:10.1029/2007GL030202

Ho, S.-P., M. Goldberg, Y.-H. Kuo, C.-Z. Zou and W. Schreiner (2009), Calibration of temperature in the lower stratosphere from microwave measurements using COSMIC radio occultation data: Preliminary results., Terr. Atmos. Oceanic Sci., 20(1), 87–100, doi:10.3319/TAO.2007.12.06.01(F3C)

Ho, S.-P., et al. (2009b), Estimating the uncertainty of using GPS radio occultation data for climate monitoring: Intercomparison of CHAMP refractivity climate records from 2002 to 2006 from different data centers, J. Geophys. Res, 114(D23), doi:10.1029/2009JD011969.

Ho S.-P., D. Hunt, A.K. Steiner, A.J. Mannucci, G. Kirchengast, H. Gleisner, S. Heise, A. von Engeln, C. Marquardt, S. Sokolovskiy, W. Schreiner, B. Scherllin-Pirscher, C. Ao, J. Wickert, S. Syndergaard, K.B. Lauritsen, S. Leroy, E.R. Kursinski, Y.-H. Kuo, U. Foelsche, T. Schmidt and M. Gorbunov (2012), Reproducibility of GPS radio occultation data for climate monitoring: Profile-to-profile inter-comparison of CHAMP climate records 2002 to 2008 from six data centers, J. Geophys. Res., 117, D18111, doi:10.1029/2012JD017665

Hoque M. and N. Jakowski (2008); Estimate of higher order ionospheric errors in GNSS positioning, Radio Science 43:RS5008 (2008). DOI 10.1029/2007RS003817

Houtekamer, P. L. and H. L. Mitchell (2005), Ensemble Kalman Filtering, Q. J. R. Meteorol. Soc., 131, 3269–3289, doi:10.1256/qj.05.135

Huang, C.-Y., Kuo, Y.-H., Chen, S.-Y., Terng, C.-T., and Chien, F.-C., Lin, P.-L., Kueh, M.-T., Chen, S.-H., Yang, M.-J., Wang, C.-J., and Prasad Rao, A. S. K. A. V.: Impact of GPS radio occultation data assimilation on regional weather predictions, GPS Solut., 14, 35-49, doi:10.1007/s10291-009-0144-1, 2010

InsideGNSS (2014), Inside GNSS Russia Launches CDMA Payload on GLONASS-M, http://www.insidegnss.com/node/4066

IROWG (2012), Climate related processing and potential of radio occultation data, CGMS-40 EUM-WP-03, available at: http://irowg.org/wpcms/wp-content/uploads/2013/12/

Climate_related_Processing_and_Potential_of_Radio_Occultation_Data.pdf

IROWG-GOS (2013), IROWG document Status of the Global Observing System for Radio Occultation (Update 2013), IROWG/DOC/2013/02, http://irowg.org/wpcms/wp-content/uploads/2013/12/Status_Global_Observing_System_for_RO.pdf

IROWG-NWP, RO data use in operational NWP systems, http://irowg.org/projects/ro-data-use-in-operational-nwp-systems/

IROWG (2015), Outcome and recommendations from the IROWG-4, CGMS-43 IROWG-WP-13, available at: http://irowg.org/wpcms/wp-content/uploads/2014/05/Outcome_and_Recommendations_from_the_IROWG-4.pdf

Ishimaru, A. (1978). Wave propagation and scattering in random media (Vol. 2, pp. 349-351). New York: Academic press

Jäggi A., R. Dach, O. Montenbruck, U. Hugentobler, H. Bock and G. Beutler (2009), Phase center modeling for LEO GPS receiver antennas and its impact on precise orbit determination, J Geod, 83, 1145-1162, doi:10.1007/s00190-00900333-02

Jensen A.S., M. S. Lohmann, H.-H. Benzon, and A.S. Nielsen (2003), Full Spectrum Inversion of radio occultation signals, Radio Science, 38, 1040, doi:10.1029/2002RS002763, 3

Kalman, R. E. (1960), A New Approach to Linear Filtering and Prediction Problems, Trans. ASME-Journal Basic Eng., 82, 34–45

Karutin S. (2016); GLONASS PROGRAMME UPDATE; Proceedings of ION GNSS+ 2016, https://www.ion.org/gnss/pdf.cfm?fid=16328

Katzberg S., O. Torres, M. Grant and D. Masters (2005), Utilizing calibrated GPS reflected signals to estimate soil reflectivity and dielectric constant: Results from SMEX02, Remote Sens. Environ., 100, 1728, doi:10.1026/j.rse.2005.09.015

Kelley M. C. (2009), The Earth's Ionosphere: Plasma Physics and Electrodynamics, Academic Press

Khaykin, S.M., A. Hauchecorne, N. Mzé and P. Keckhut (2015), Seasonal variation of gravity wave activity at midlatitudes from 7 years of COSMIC GPS and Rayleigh lidar temperature observations, Geophys. Res. Lett., 42, doi:10.1002/2014GL062891

Khaykin, S., Visiting Scientist Report 29: Retrieval of gravity waves from RO measurements: Capacities and limitations, SAF/ROM/DMI/REP/VS/29/, Version 1.1, 2016

Kim, J. and S.-W. Son (2012), Tropical cold-point tropopause: Climatology, seasonal cycle, and intraseasonal variability derived from COSMIC GPS radio occultation measurements, J. Climate, 25, 5343–5360, doi:10.1175/JCLI-D-11-00554.1

Kintner, P.M., B.M. Ledvina and E.R. de Paula (2007), GPS and ionospheric scintillations, Space Weather, 5(9):S09003, doi:10.1029/2006SW000260

Kirchengast, G. (2016), The reference occultation processing system approach to interpret GNSS radio occultation as SI-traceable planetary system refractometer, presentation at OPAC-IROWG 2016, 8-14 September 2016, Schloss Seggau, Leibnitz, Austria, http://wegcwww.uni-graz.at/opacirowg2016/data/public/files/opacirowg2016_Gottfried_Kirchengast_abstract_261.pdf

Kishore, P., G. Basha, M. Venkat Ratnam, I. Velicogna, T.B.M.J. Ouarda and D. Narayana Rao (2016), Evaluating CMIP5 models using GPS radio occultation COSMIC temperature in UTLS region during 2006–2013: twenty-first century projection and trends, Clim. Dyn., 1–18, doi:10.1007/s00382-016-3024-8

Klingler, R. (2014), Observing Sudden Stratospheric Warmings with Radio Occultation Data, with Focus on the Event 2009, MSc thesis, Wegener Center, University of Graz, June 2014

Knibbe, W.J.J., J.F. de Haan, J.W. Hovenier, D.M. Stam, R.B.A. Koelemeijer and P. Stammes (2000), Deriving terrestrial cloud top pressure from photopolarimetry of reflected light, J. Quant. Spectrosc. Ra., 64, 173–199, doi:10.1016/S0022-4073(98)00135-6

Koelemeijer, R.B.A., P. Stammes, J.W. Hovenier and J.F. de Haan (2002), Global distributions of effective cloud fraction and cloud top pressure derived from oxygen A band spectra measured by the global ozone monitoring experiment: Comparison to ISCCP data, J. Geophys. Res., 107, AAC 5-1–AAC 5-9, doi:10.1029/2001JD000840

Kogure, S. (2017), QZSS Update, Proc. ION GNSS+ 2017, Portland, Oregon, September

Komjathy A., J. Maslanik, V. U. Zavorotny, P. Axelrad and S. J. Katzberg (2000), Sea ice remote sensing using surface reflected GPS signals, in Proceedings of IEEE 2000 International Geoscience and Remote Sensing Symposium, IGARSS 2000, pp. 28552857, IEEE Press, Piscataway, N. J.

Komjathy, A., B. Wilson, X. Pi, V. Akopian, M. Dumett, B. Iijima, O. Verkhoglyadova and A. J. Mannucci (2010), JPL/USC GAIM: On the impact of using COSMIC and ground-based GPS measurements to estimate ionospheric parameters, J. Geophys. Res. Sp. Phys., 115(2), 1–10, doi:10.1029/2009JA014420

Kuo, Y.-H., T.-K. Wee, S. Sokolovskiy, C. Rocken, W. Schreiner, D. Hunt and R.A. Anthes (2004), Inversion and error estimation of GPS radio occultation data, J. Meteorol. Soc. Japan, 82, 507–531.

Kursinski, E.R., G.A. Hajj, K.R. Hardy, J.T. Schofield and R. Linfield (1997), Observing the Earth's atmosphere with radio occultation measurements using the Global Positioning System, J. Geophys. Res., 102, 23429–23465

Kursinski, E.R., A. Kursinski, T. Gebhardt and C. Ao (2016), GPS RO water vapor, presentation at OPAC-IROWG 2016, 8-14 September 2016, Schloss Seggau, Leibnitz, Austria, http://wegcwww.uni-graz.at/opacirowg2016/data/public/files/ opacirowg2016_rob_kursinski_abstract_255.pdf

Lackner, B.C., A.K. Steiner and G. Kirchengast (2011a), Where to see climate change best in radio occultation variables – study using GCMs and ECMWF reanalyses, Ann. Geophys. 29(11), 2147-2167, doi:10.5194/angeo-29-2147-2011

Lackner, B.C., A.K. Steiner, G. Kirchengast and G.C. Hegerl (2011b), Atmospheric Climate Change Detection by Radio Occultation Data Using a Fingerprinting Method, J. Climate, 24(20), 5275–5291, doi:10.1175/2011JCLI3966.1

Ladstädter, F., A.K. Steiner, U. Foelsche, L. Haimberger, C. Tavolato and G. Kirchengast (2011), An assessment of differences in lower stratospheric temperature records from (A)MSU, radiosondes, and GPS RO, Atmos. Meas. Tech., 4(9), 1965–1977, doi:10.5194/amt-4-1965-2011

Ladstädter, F., A.K. Steiner, M. Schwärz and G. Kirchengast (2015), Climate intercomparison of GPS radio occultation, RS90/92 radiosondes and GRUAN from 2002 to 2013, Atmos. Meas. Tech., 8, 1819–1834, doi:10.5194/amt-8-1819-2015

Lee, I.T., T. Matsuo, A.D. Richmond, J. Y. Liu, W. Wang, C. H. Lin, J. L. Anderson and M. Q. Chen (2012), Assimilation of FORMOSAT-3/COSMIC electron density profiles into a coupled thermosphere/ionosphere model using ensemble Kalman filtering, J. Geophys. Res., 117(A10318), doi:10.1029/2012JA017700

Le Marshall, J., Xiao, Y., Norman, R., Zhang, K., Rea, A., Cucurull, L., Seecamp, R., Steinle, P., Puri, K., and Le, T.: The beneficial impact of radio occultation observations on Australian region forecasts, Australian Meteorol. Oceanogr. J., 60, 121-125, 2010

Leroy, S.S. (1997), The measurement of geopotential heights by GPS radio occultation, J. Geophys. Res., 102, 6971–6986

Leroy, S.S. and G. North (2000), The application of COSMIC data to global change research, Terr. Atmos. Oceanic Sci., 11(1), 187–210

Leroy, S.S., J.A. Dykema and J.G. Anderson (2006a), Climate benchmarking using GNSS occultation, in Atmosphere and Climate: Studies by Occultation Methods, edited by U. Foelsche, G. Kirchengast and A. Steiner, pp. 287–301, Springer-Verlag Berlin Heidelberg

Leroy, S.S., J. G. Anderson and J. A. Dykema (2006b), Testing climate models using GPS radio occultation: A sensitivity analysis, J. Geophys. Res., 111, D17105, doi:10.1029/2005JD006145

Leroy, S., J. Anderson, J. Dykema and R. Goody (2008), Climate signal detection times and constraints on climate benchmark accuracy requirements, J. Clim., 21, 841–846

Lewis, H.W. (2009), A robust method for tropopause altitude identification using GPS radio occultation data, Geophys. Res. Lett., 36, L12808, doi:10.1029/2009GL039231

Lin, C.Y., T. Matsuo, J.Y. Liu, C.H. Lin, H.F. Tsai and E.A. Araujo-Pradere (2015), Ionospheric assimilation of radio occultation and ground-based GPS data using non-stationary background model error covariance, Atmos. Meas. Tech., 8(1), 171–182, doi:10.5194/amt-8-171-2015

Lindzen, R.S. and J.R. Holton (1968), A theory of the Quasi-Biennial Oscillation, J. Atmos. Sci., 25, 1095–1107

Liu, L., M. He, W. Wan and M.-L. Zhang (2008), Topside ionospheric scale heights retrieved from Constellation Observing System for Meteorology, Ionosphere, and Climate radio occultation measurements, J. Geophys. Res., 113, A10304, doi:10.1029/2008JA013490

Liu, C.L. et al. (2013), Characterization of residual ionospheric errors in bending angles using GNSS RO end-to-end simulations, Adv. Space. Res., 52, 821-836

Liu, C.L. et al. (2015), Quantifying residual ionospheric errors in GNSS radio occultation bending angles based on ensembles of profiles from end-to-end simulations, Atmos. Meas. Tech., 8, 2999-3019, doi:10.5194/amt-8-2999-2015

Luntama, J.-P., G. Kirchengast, M. Borsche, U. Foelsche, A. Steiner, S. Healy, A. von Engeln, E. O'Clerigh and C. Marquardt (2008), Prospects of the EPS GRAS mission for operational atmospheric applications, Bull. Am. Meteorol. Soc., 89(12), 18631875.

Lutcke S., N. Zelensky, D. Rowlands and F. Lemoine (2003), Williams T.; The 1-centimeter orbit: Jason-1 precision orbit determination using GPS, SLR, DORIS and altimeter data. Mar Geod 26(3-4):339-421

Ma J. (2017), Development of BeiDou Navigation Satellite System (BDS) – A System Update Report (2016-2017), Proc. ION GNSS+ 2017, Portland, Oregon, September

Mandrake, L., B. Wilson, C. Wang, G. A. Hajj, A. J. Mannucci and X. Pi (2005), A performance evaluation of the operational Jet Propulsion Laboratory/University of Southern California Global Assimilation Ionospheric Model (JPL/USC GAIM), J. Geophys. Res., 110(A12306), doi:doi:10.1029/2005JA011170

McNamara, L.F. (2008), Accuracy of models of hmF2 used for long-term trend analyses, Radio Science, 43, RS2002

Marinov, P., I. Kutiev, A. Belehaki and I. Tsagouri (2015). Modeling the plasma- sphere to topside ionosphere scale height ratio. Journal of Space Weather and Space Climate, 5, A27

Martín-Neira M. (1993), A Passive Reflectometry and Interferometry System (PARIS): Application to ocean altimetry, ESA J., 17, 331355

Martin-Neira M., S. D'Addio, C. Buck, N. Floury and R. Prieto-Cerdeira (2011), The PARIS Ocean Altimeter In-Orbit Demonstrator, IEEE Transactions on Geoscience and Remote Sensing, vol. 49, no. 6, pp. 22092237, June 2011

Masters D., P. Axelrad and S. Katzberg (2004), Initial results of land-reflected GPS bistatic radar measurements in SMEX02, Remote Sens. Environ., 92, 507520, doi:10.1016/j.rse.2004.05.016, 2004

Melbourne, W.G., E.S. Davis, C.B. Duncan, G.A. Hajj, K.R. Hardy, E.R. Kursinski, T.K. Meehan, L.E. Young and T.P. Yunck (1994), The application of spaceborne GPS to atmospheric limb sounding and global change monitoring, JPL Publication 94-18, 147 pp., Jet Propulsion Lab, Pasadena, CA

Mehta, S.K., M. Fujiwara, T. Tsuda and J.-P. Vernier (2015), Effect of recent minor volcanic eruptions on temperatures in the upper troposphere and lower stratosphere, J. Atmos. Solar-Terr. Phys., 129, 99-110, doi: 10.1016/j.jastp.2015.04.009

Minkwitz, D., K.G. van den Boogaart, T. Gerzen, M. Hoque and M. Hernández-Pajares (2016), Ionospheric tomography by gradient-enhanced kriging with STEC measurements and ionosonde characteristics, Ann. Geophys., 34, 999-1010, doi:10.5194/angeo-34-999-2016

Minnis, P., C.R. Yost, S. Sun-Mack and Y, Chen (2008), Estimating the top of the cloud of optically thick ice clouds from thermal infrared satellite observations using CALIPSO data, Geophys. Res. Lett., 35, L12801, doi:10.1029/2008GL033947

Mitchell, C.N. and P.S.J. Spencer (2003), A three-dimensional time-dependent algorithm for ionospheric imaging using GPS, Ann. Geophys., 46(4), 687–696

Montenbruck O., Y. Andres, H. Bock., T. van Helleputte, J. van den IJssel, M. Loiselet, C. Marquardt, P. Silvestrin, P. Visser and Y. Yoon (2008); Tracking and Orbit Determination Performance of the GRAS Instrument on MetOp-A; GPS Solutions, 12(4):289-299 (2008). DOI 10.1007/s10291-008-0091-2, http://link.springer.com/article/10.1007%2Fs10291-008-0091-2

Montenbruck O., U. Hugentobler, R. Dach, P. Steigenberger and A. Hauschild (2012); Apparent clock variations of the Block IIF-1 (SVN62) GPS satellite. GPS Solut. 16:303313, http://link.springer.com/article/10.1007%2Fs10291-011-0232-x

Morton J.Y.Y.T., S. Taylor, W. Pelgrum (2013). Characterization of high-latitude ionospheric scintillation of GPS signals. Radio Science, 48(6), 698-708

MRD (2011), Post-EPS Mission Requirements Document, EUM/PEPS/REQ/06/0043

Nava, B., P. Coïsson and S.M. Radicella (2008), A new version of the NeQuick ionosphere electron density model. Journal of Atmospheric and Solar-Terrestrial Physics. http://dx.doi.org/10.1016/j.jastp.2008.01.015

Nicolls, M.J., F.S. Rodrigues, G.S. Bust and J.L. Chau (2009), Estimating E region density profiles from radio occultation measurements assisted by IDA4D, J. Geophys. Res. Sp. Phys., 114(10), 1–12, doi:10.1029/2009JA014399

Notarpietro R. (2012), Implementation of ROSA radio occultation data handling into EUMETSAT and GRAS SAF processing, CDOP Visiting Scientist Report 16, 3 March 2012, http://www.romsaf.org/Publications/reports/grassaf_vs16_rep_v1.2.pdf

Okazaki, I. and K. Heki (2012), Atmospheric temperature changes by volcanic eruptions: GPS radio occultation observations in the 2010 icelandic and 2011 chilean cases, J. Volcanol. Geoth. Res., 245-246, 123-127, doi: 10.1016/j.jvolgeores.2012.08.018

Ohring, G. (Ed.) (2007), Achieving Satellite Instrument Calibration for Climate Change, National Oceanic and Atmospheric Administration, Washington, DC

Ohring, G., B. Wielicki, R. Spencer, B. Emery and R. Datla (2005), Satellite Instrument Calibration for Measuring Global Climate Change: Report of a Workshop, Bull. Amer. Meteor. Soc., 86(9), 1303–1313, doi:10.1175/BAMS-86-9-1303

Olivares-Pulido, G., M. Hernández- Pajares, A. Aragón-Angel and A. Garcia-Rigo (2016), A linear scale height Chapman model supported by GNSS occultation measurements, J. Geophys. Res. Space Physics, 121, 79327940, doi:10.1002/ 2016JA022337

Padullés R., E. Cardellach, M. de la Torre Juárez, S. Tomas, F.J. Turk, S. Oliveras, C.O. Ao and A. Rius (2016), Atmospheric polarimetric effects on GNSS Radio Occultations: the ROHP-PAZ field campaign, Atmospheric Chemistry and Physics, 16, pp. 635-649, 2016, Jan, 10.5194/acp-16-635-2016

Padullés R., E. Cardellach and A. Rius (2016b), Untangling rain structure from polarimetric GNSS Radio Occultation observables: a 2D tomographic approach, European Journal of Remote Sensing, Volume: 49, Year: 2016, Pages: 571 – 585, doi:10.5721/EuJRS20164930

Petrie, E. J., M. Hernandez-Pajares, P. Spalla, P. Moore and M.A. King (2011). A review of higher order ionospheric refraction effects on dual frequency GPS. Surveys in geophysics, 32(3), 197-253

Plackett, R.L. (1950), Some theorems in least squares, Biometrika, 37(12), 14957

Pirscher, B., U. Foelsche, B.C. Lackner and G. Kirchengast (2007), Local time influence in single-satellite radio occultation climatologies from sun-synchronous and non sun-synchronous satellites, J. Geophys. Res., 112, D11119, doi:10.1029/2006JD007934

Pirscher, B., U. Foelsche, M. Borsche, G. Kirchengast and Y.-H. Kuo (2010), Analysis of migrating diurnal tides detected in FORMOSAT-3/COSMIC temperature data, J. Geophys. Res., 115, D14108, doi:10.1029/2009JD013008

Platnick, S., M.D. King, S.A. Ackerman, W.P. Menzel, B.A. Baum and J.C. Riedi (2003) and Frey, R. A.: The MODIS cloud products: Algorithms and examples from Terra, IEEE

Trans. Geosci. Remote Sens., 41, 459–473, doi:10.1109/TGRS.2002.808301

Poli, P., S.B. Healy, F. Rabier, and J. Pailleux (2008), Preliminary assessment of the scalability of GPS radio occultations impact in numerical weather prediction, Geophys. Res. Lett., 35, 10.1029/2008GL035873

Poole, L.R., D.M. Winker, J.R. Pelon and M.P. McCormick. (2002), CALIPSO: GLOBAL aerosol and cloud observations from lidar and passive instruments, Proc. SPIE, 481, 419–426, doi:10.1117/12.462519

Qu, X., Z. J. Li, J. An, and W. Ding (2015), Characteristics of second-order residual ionospheric error in GNSS radio occultation and its impact on inversion of neutral atmospheric parameter, J. Atmos. Solar-Terr. Phys., 130-131, 159-171

Quiles, A. (2017), GALILEO System Status Update, Proc. ION GNSS+ 2017, Portland, Oregon, September

Randel, W.J., F. Wu and W. Rivera Ríos (2003), Thermal variability of the tropical tropopause region derived from GPS/MET observations, J. Geophys. Res., 108(D1), 4024, doi:10.1029/2002JD002595

Randel, W.J. and F. Wu (2005), Kelvin wave variability near the equatorial tropopause observed in GPS radio occultation measurements, J. Geophys. Res., 110, D03102, doi:10.1029/2004JD005006

Randel, W.J., et al. (2009), An update of observed stratospheric temperature trends, J. Geophys. Res., 112, D02107, doi:10.1029/2008JD010421

Randel, W.J., and F. Wu (2015), Variability of zonal mean tropical temperatures derived from a decade of GPS radio occultation data, J. Atmos. Sci., 72(3), 1261–1275, doi:10.1175/JAS-D-14-0216.1

Ratnam M.V. and S.G. Basha (2010), A robust method to determine global distribution of atmospheric boundary layer top from COSMIC GPS RO measurements, Atmos Sci Lett, 11, 216–222

Rennie, M. (2010), The impact of GPS radio occultation assimilation at the Met Office Q. J. R. Meteorol. Soc. 136(646) 116, 131

Rieckh, T., B. Scherllin-Pirscher, F. Ladstädter and U. Foelsche (2014), Characteristics of tropopause parameters as observed with GPS radio occultation, Atmos. Meas. Tech., 7(11), 3947–3958, doi:10.5194/amt-7-3947-2014

Rieckh, T., R. Anthes, W. Randel, S.-P. Ho and U. Foelsche (2016), Tropospheric dry layers in the TropicalWestern Pacific: Comparisons of GPS radio occultation with multiple data sets, Atmo. Meas. Techn. Discuss., 1–22, doi:10.5194/amt-2016-258

Ringer, M.A. and S.B. Healy (2008), Monitoring twenty-first century climate using GPS radio occultation bending angles, Geophys. Res. Lett, 35(5), doi:10.1029/2007GL032462

Rius A., E. Cardellach and M. Martín-Neira (2010), Altimetric analysis of the sea surface GPS reflected signals, IEEE Trans. Geosci. Remote Sens., 48(4), 21192127, doi:10.1109/TGRS.2009.2036721

ROPP1DV, ROM SAF ATBD: 1DVAR algorithms, SAF/ROM/DMI/ALG/1DV/002

ROPPL3G, ROM SAF ATBD: Level 3 Gridded Climate data, SAF/ROM/DMI/ALG/GRD/001; available from: http://www.romsaf.org

ROPPUG, ROPP User Guide; available from http://www.romsaf.org

Ruf C., Z. Gleason, S. Jelenak, S. Katzberg, A. Ridley, R. Rose, J. Scherrer and V. Zavorotny (2012), The CYGNSS nanosatellite constellation hurricane mission, Proc. 2012 International Geoscience and Remote Sensing Symposium, Munich, July 20-27, pp. 214216

Šácha, P., U. Foelsche and P. Pišoft (2014): Analysis of internal gravity waves with GPS RO density profiles, Atmos. Meas. Tech., 7, 4123-4132, doi:10.5194/amt-7-4123-2014

Saynisch J., M. Semmling, J. Wickert and M. Thomas (2015), Potential of space-borne GNSS reflectometry to constrain simulations of the ocean circulation, Ocean Dynamics, vol. 65, no. 11, pp. 14411460

Scherliess, L., D.C. Thompson and R.W. Schunk (2011), Data assimilation models: A new tool for ionospheric science and applications, in The Dynamics Magnetosphere, edited by W. Liu and M. Fujimoto, pp. 329–339, Springer, Berlin

Scherllin-Pirscher, B., A.K. Steiner, G. Kirchengast, Y.-H. Kuo and U. Foelsche (2011a), Empirical analysis and modeling of errors of atmospheric profiles from GPS radio occultation, Atmos. Meas. Tech., 4(9), 1875–1890, doi:10.5194/amt-4-1875-2011

Scherllin-Pirscher, B., G. Kirchengast, A.K. Steiner, Y.-H. Kuo and U. Foelsche (2011b), Quantifying uncertainty in climatological fields from GPS radio occultation: an empirical-analytical error model, Atmos. Meas. Tech, 4(9), 2019–2034, doi:10.5194/amt-4-2019-2011

Scherllin-Pirscher, B., C. Deser, S.-P. Ho, C. Chou, W. Randel and Y.-H. Kuo (2012), The vertical and spatial structure of ENSO in the upper troposphere and lower stratosphere from GPS radio occultation measurements, Geophys. Res. Lett., 39(20), L20801, doi:10.1029/2012GL053071

Scherllin-Pirscher, B., A.K. Steiner, G. Kirchengast, M. Schwärz and S. Leroy (2016a), The power of vertical geolocation of atmospheric profiles from GNSS radio occultation, J. Geophys. Res., 122(3), Pages 1595–1616, doi:10.1002/2016JD025902

Scherllin-Pirscher, B., W.J. Randel and J. Kim (2016b), Tropical temperature variability and

Kelvin wave activity in the UTLS from GPS RO measurements, Atmos. Chem. Phys. Discuss., doi:10.5194/acp-2016-576, revised

Schmidt, T., J. Wickert, G. Beyerle and C. Reigber (2004), Tropical tropopause parameters derived from GPS radio occultation measurements with CHAMP, J. Geophys. Res., 109, D13105, doi:10.1029/2004JD004566

Schmidt, T., S. Heise, J. Wickert, G. Beyerle and C. Reigber (2005), GPS radio occultation with CHAMP and SAC-C: global monitoring of thermal tropopause parameters, Atmos. Chem. Phys., 5, 1473–1488

Schmidt, T., J. Wickert, G. Beyerle and S. Heise (2008), Global tropopause height trends estimated from GPS radio occultation data, Geophys. Res. Lett., 35, L11806, doi:10.1029/2008GL034012

Schmidt, T., J. Wickert and A. Haser (2010), Variability of the upper troposphere and lower stratosphere observed with GPS radio occultation bending angles and temperatures, Adv. Space Res., 46, 150–161, doi:10.1016/j.asr.2010.01.021

Schmidt, T. (2013), Visiting Scientist Report 22: Beta testing of ROPP 7.0, SAF/ROM/DMI/REP/VS22/001, Version 1.0

Schrøder, T., S. Leroy, M. Stendel and E. Kaas (2003), Validating the microwave sounding unit stratospheric record using GPS occultation, Geophys. Res. Lett., 30, doi:10.1029/2003GL017588

Seidel, D.J. and W.J. Randel (2006), Variability and trends in the global tropopause estimated from radiosonde data, J. Geophys. Res., 111, D21101, doi:10.1029/2006JD007363

Semmling M., J. Beckheinrich, J. Wickert, G. Beyerle, S. Schön, F. Fabra, H. Pflug, K. He, J. Schwabe and M. Scheinert (2014), Sea surface topography retrieved from GNSS reflectometry phase data of the GEOHALO flight mission, Geophysical Research Letters, V.41, pp 954-960

Shaikh, M.M.; B. Nava and A., Kashcheyev (2017), A model-assisted radio occultation data inversion method based on data ingestion into NeQuick. Adv. Space Res. 59 (1), 326-336, http://dx.doi.org/10.1016/j.asr.2016.09.006

Sherwood, S.C., P. Minnis, M. McGill and J.C. Chae (2004), Underestimation of deep convective cloud tops by thermal imagery, Geophys. Res. Lett., 31, L11102, doi:10.1029/2004GL019699

Shi, Y. and Y. Gao (2014), A comparison of three PPP integer ambiguity resolution methods, GPS Solut, 18, 519-528, doi:10.1007/s10291-013-0348-2

Skone, S., K. Knudsen and M. de Jong (2001), Limitations in GPS receiver tracking performance under ionospheric scintillation conditions, Phys. Chem. Earth A, 26, 613-621, doi:10.1016/S1464-1895(01)00110-7

Skone, S. and M. de Jong (2000). The impact of geomagnetic substorms on GPS receiver performance. Earth, Planets and Space, 52(11), 1067-1071

Spencer, P.S.J. and C.N. Mitchell (2007), Imaging of fast moving electron-density structures in the polar cap, Ann. Geophys., 50(3), 427–434

Spichtinger, P., K. Gierens and A. Dörnbrack (2005), Formation of ice supersaturation by mesoscale gravity waves, Atmos. Chem. Phys., 5, 1243–1255

Steiner, A.K. and G. Kirchengast (2000): Gravity Wave Spectra from GPS/MET Occultation Observations, J. Atmos. Ocean. Tech., 17, 495–503, doi:10.1175/1520-0426(2000)017<0495:GWSFGM>2.0.CO;2

Steiner, A.K. and G. Kirchengast (2005), Error analysis for GNSS radio occultation data based on ensembles of profiles from end-to-end simulations, J. Geophys. Res., 110, doi:10.1029/2004JD005251

Steiner, A.K., A. Löscher and G. Kirchengast (2006), Error characteristics of refractivity profiles retrieved from CHAMP radio occultation data, in Atmosphere and Climate – Studies by Occultation Methods, U. Foelsche, G. Kirchengast, and A. K. Steiner (Eds.), Springer, Berlin-Heidelberg, 27–36, doi:10.1007/3-540-34121-8_3

Steiner, A.K., G. Kirchengast, U. Foelsche, L. Kornblueh, E. Manzini and L. Bengtsson (2001), GNSS occultation sounding for climate monitoring, Phys. Chem. Earth (A), 26, 113–124

Steiner, A.K., G. Kirchengast, M. Borsche, U. Foelsche and T. Schoengassner (2007), A multi-year comparison of lower stratospheric temperatures from CHAMP radio occultation data with MSU/AMSU records, J. Geophys. Res, 112(D22), D22110, doi:10.1029/2006JD008283

Steiner, A.K., et al. (2009a), Atmospheric temperature change detection with GPS radio occultation 1995 to 2008, Geophys. Res. Lett, 36(18), doi:10.1029/2009GL039777

Steiner, A.K., G. Kirchengast, M. Borsche and U. Foelsche (2009b), Lower stratospheric temperatures from CHAMP RO compared to MSU/AMSU records: An analysis of error sources, in New Horizons in Occultation Research: Studies in Atmosphere and Climate, A. K. Steiner, B. Pirscher, U. Foelsche, and G. Kirchengast (Eds.), Springer, Berlin, Heidelberg, 219–234, doi:10.1007/978-3-642-00321-9_18

Steiner, A.K., et al. (2011), GPS radio occultation for climate monitoring and change detection, Radio Sci, 46, RS0D24, doi:10.1029/2010RS004614

Steiner, A.K., et al. (2013a), Quantification of structural uncertainty in climate data records from GPS radio occultation, Atmos. Chem. Phys., 13(3), 1469–1484, doi:10.5194/acp-13-1469-2013

Steiner, A.K., J. Schwarz, and M.A. Ringer (2013b), Evaluation of climate models with radio occultation observations, presented at: OPAC-IROWG 2013, 5-11 September 2013, Schloss Seggau, Leibnitz, Austria, http://irowg.org/wpcms/wp-content/uploads/2013/11/IROWG-3_Minutes_Summary.pdf

Steiner, A.K., et al. (2016a), Consistency of multi-satellite RO records from different data centers: First results, presented at OPAC-IROWG 2016, 8-14 September 2016, Schloss Seggau, Leibnitz, http://wegcwww.uni-graz.at/opacirowg2016/data/public/files/opacirowg2016_Andrea_Steiner_abstract_174.pdf

Steiner, A.K., B. Scherllin-Pirscher, F. Ladstädter, H. Wilhelmsen and B. Angerer (2016b), Vertically resolved atmospheric trends from the RO record 2001 to 2016, presented at OPAC-IROWG 2016, 8-14 September 2016, Schloss Seggau, Leibnitz, http://wegcwww.uni-graz.at/opacirowg2016/data/public/files/pacirowg2016_Andrea_Steiner_abstract_211.pdf

Stendel, M. (2006), Monitoring climate variability and change by means of GNSS data, in Atmosphere and Climate: Studies by Occultation Methods, U. Foelsche, G. Kirchengast, A. K. Steiner (Eds.), pp. 275–285, Springer, Berlin-Heidelberg-New York

Strategy (2006), EUMETSAT Strategy: 2030, EUM/C/59/06/DOC/28

Syndergaard, S. (2002), A new algorithm for retrieving GPS radio occultation total electron content, Geophys. Res. Lett., 29(16), 3–6, doi:10.1029/2001GL014478

Tian, B., C.O. Ao, D.E. Waliser, E.J. Fetzer, A.J. Mannucci and J. Teixeira (2012), Intraseasonal temperature variability in the upper troposphere and lower stratosphere from the GPS radio occultation measurements, J. Geophys. Res., 117(D15), D15110, doi:10.1029/2012JD017715

Tsai, H.-F., T. Tsuda, G. Hajj, J. Wickert and Y. Aoyama (2004), Equatorial Kelvin waves observed with GPS occultation measurements (CHAMP and SAC-C), J. Meteorol. Soc. Jpn., 82, 397–406

Tsuda, T., M. Nishida, C. Rocken and R.H. Ware (2000), A global morphology of gravity wave activity in the stratosphere revealed by the GPS occultation data (GPS/MET), J. Geophys. Res., 105, 7257–7273, doi:10.1029/1999JD901005

Trenberth, K., et al. (2013), Challenges of a Sustained Climate Observing System, in Climate Science for Serving Society, edited by G. R. Asrar and J. W. Hurrell, pp. 13–50, Springer Netherlands

Tupper, A., S. Carn, J. Davey, Y. Kamada, R. Potts, F. Prata and M. Tokuno (2004), An evaluation of volcanic cloud detection techniques during recent significant eruptions in the western “Ring of Fire”, Remote Sens. Environ., 91, 27-46, doi: 10.1016/j.rse.2004.02.004

Van den IJssel, J., J. Encarnaçao, E. Doornbos and P. Visser (2015), Precise science orbits for the Swarm satellite constellation, Adv Space Res, 56(6), 1042-1055, doi:10.1016/j.asr.2015.06.002

Van den IJssel, J., B. Forte and O. Montenbruck (2016), Impact of Swarm GPS receiver updates on POD performance, Earth, Planets and Space, 68(85), doi:10.1186/s40623-016-0459-4

Van Dierendock, A.J. (1996) GPS receivers, In: Parkinson B.W., Spilker J.J. (eds) Global positioning system: theory and applications, vol 1, AIAA, Washington, 329-407, doi:10.2514/4.866388

Vedel, H. and M. Stendel (2003), On the direct use of GNSS refractivity measurements for climate monitoring, Proc. from the 4th Oerstedt International Science Team Conference (OIST-4), P. Stauning (Ed.), pp. 275–278, Danish Meteorological Institute, Copenhagen, DK

Vorob'ev, V.V. and T.G. Krasil'nikova (1994), Estimation of the accuracy of the atmospheric refractive index recovery from the NAVSTAR system, USSR Phys. Atmos. Ocean (Eng. Trans.), 29(5), 602–609

Wang, K.-Y., S.-C. Lin and L.-C. Lee (2009), Immediate impact of the Mt Chaiten eruption on atmosphere from FORMOSAT-3/COSMIC constellation, Geophys. Res. Lett., 36, L03808, doi:10.1029/2008GL036802

Wang, W., K. Matthes, T. Schmidt and L. Neef (2013), Recent variability of the tropical tropopause inversion layer, Geophys. Res. Lett., 40, 6308–6313, doi:10.1002/2013GL058350

Wang, W., K. Matthes and T. Schmidt (2015), Quantifying contributions to the recent temperature variability in the tropical tropopause layer, Atmos. Chem. and Phys., 15(10), 5815–5826, doi:10.5194/acp-15-5815-2015

Ware, R., et al. (1996), GPS Sounding of the Atmosphere from Low Earth Orbit: Preliminary Results, Bull. Amer. Meteor. Soc., 77, 19–40, doi:10.1175/1520-0477(1996)077<0019:GSOTAF>2.0.CO;2

Whitney, S., (2017), GPS Status & Modernization Progress: Service, Satellites, Control Segment, and Military GPS User Equipment, Proc. ION GNSS+ 2017, Portland, Oregon, September

Wickert J., E. Cardellach, J. Bandeiras, L. Bertino, O. Andersen, A. Camps, N. Catarino, B. Chapron, F. Fabra, N. Floury, G. Foti, C. Gommenginger, J. Hatton, P. Høeg, A. Jäggi, M. Kern, T. Lee, Z. Li, M. Martin-Neira, H. Park, N. Pierdicca, F. Ressler, A. Rius, J. Rosselló, J. Saynisch, F. Soulat, C.K. Shum, M. Semmling, A. Sousa, J. Xie and C. Zuffada (2016), GEROS-ISS: GNSS REflectometry, Radio Occultation and Scatterometry onboard the International Space Station, IEEE Journal of Selected Topics in Applied Earth Observations and Remote Sensing (JSTARS), Vol.9, Issue 10, pp 4552 – 4581, DOI: 10.1109/JSTARS.2016.2614428

Yeh, K.C. and C.H. Liu (1982). Radio wave scintillations in the ionosphere. Proceedings of the IEEE, 70(4), 324-360

Yuan, L.L., R.A. Anthes, R.H. Ware, C. Rocken, W.D. Bonner, M.G. Bevis and S. Businger (1993), Sensing climate change using the global positioning system, J. Geophys. Res., 98, 14925–14937

Zavorotny V.U. and A.G. Voronovich (2000), Scattering of GPS signals from the ocean with wind remote sensing application, IEEE Trans. Geosci. Remote Sens., 38, 951964

Zehner, C. (Ed.) (2010), Monitoring volcanic ash from space, Proceedings of the ESA-EUMETSAT workshop on the 14 April to 23 May 2010 eruption at the Eyjafjöll volcano, South Iceland. Frascati, Italy, 26–27 May 2010, ESA-Publication STM-280, doi:10.5270/atmch-10-01

Zeng, Z., S. Sokolovskiy, W. Schreiner, D. Hunt , J. Lin and Y.-H. Kuo (2016): Ionospheric correction of GPS radio occultation data in the troposphere, Atmos. Meas. Tech., 9, 335-346, doi:10.5194/amt-9-335-2016

Zhang, M.-L., L. Liu, W. Wan and B. Ning (2016), Comparison of the observed topside ionospheric and plasmaspheric electron content derived from the COSMIC podTEC measurements with the IRI_Plas model results. Adv. Space Res., http://dx.doi.org/10.1016/j.asr.2016.10.025

Zhao Q., Wang C., Guo J., Wang B., Liu J. (2018) Precise orbit and clock determination for BeiDou-3 experimental satellites with yaw attitude analysis. GPS Solutions 22:4. DOI 10.1007/s10291-017-0673-y

Zhizhin, M., E. Kihn, R. Redmon, D. Medvedev and D. Mishin (2008), Space Physics Interactive Data Resource SPIDR, Earth Science Informatics, v. 1(2), 79-91

# APPENDIX B ACRONYMS

| Acronym | Resolution |
|---|---|
| 3MI | Multi-view Multi-channel Multi-polarization Imager |
| AFS | Atomic Frequency Standard |
| CCSDS | Consultative Committee for Space Data Systems |
| CGMS | Coordination Group for Meteorological Satellites |
| DLL | Delay Locked Loop |
| EPS (-SG) | EUMETSAT Polar System (-Second Generation) |
| EUMETSAT | European Organisation for the Exploitation of Meteorological Satellites |
| EURD | End-User Requirements Document |
| GCOS | Global Climate Observing System |
| GLONASS | Global Navigation Satellite System |
| GMES | Global Monitoring for Environment and Security initiative |
| GNSS | Global Navigation Satellite System |
| GPS | Global Positioning System |
| GRAS | GNSS Receiver for Atmospheric Sounding |
| GRM | GNSS Receiver Module |
| IAS | Infra-red Atmospheric Sounding (also called IASI-NG) |
| IASI-NG | Infrared Atmospheric Sounder Interferometer-Next Generation |
| ICI | Ice Cloud Imager |
| IMT | Instrument Measurement Time |
| IR | Infra-Red |
| IRNSS | Indian Regional Navigation Satellite System |
| IROWG | International RO Working Group (under CGMS) |
| LEO | Low-Earth Orbit |
| MRD | Mission Requirements Document |
| MW | Micro-Wave |
| MWI | Microwave Imaging Radiometer |
| NCO | Numerically Controlled Oscillator |
| NRT | Near Real Time |
| NWP | Numerical Weather Prediction |
| OBT | On-board Time |
| PMET | Post-EPS (now EPS-SG) Mission Experts Team |
| POD | Precise Orbit Determination |
| QZSS | Quasi-Zenith Satellite System |
| RO | Radio Occultation (used generically and for EPS-SG RO(-SG) instrument) |
| ROM SAF | Radio Occultation Meteorology Satellite Application Facility |
| SBAS | Satellite Based Augmentation System |
| SCA | Scatterometer |
| SLTA | Straight Line Tangent Altitude |
| SV | Space Vehicle |
| UVNS | Ultraviolet, Visible, Near-infra-red, Short-wave-infra-red sounding mission |
| USO | Ultra Stable Oscillator |
| UTC | Coordinated Universal Time |
| VII | Visible/Infra-red Imaging mission |
| WMO | World Meteorological Organisation |

## APPENDIX C RO SAG / SCIENCE PLAN CONTRIBUTORS

This report is based on contributions from the following members of the Radio Occultation Science Advisory Group, ESA and EUMETSAT staff and other experts:

RO SAG Members ESA invited:

- B. Forte, University of Bath, UK
- G. Kirchengast, University of Graz, Austria
- J. van den Ijssel, Technical University of Delft, The Netherlands

RO SAG Members EUMETSAT invited:

- A. Hauschild, German Aerospace Center (DLR), Wessling, Germany
- S. Healy, ECMWF, Reading, United Kingdom
- M. Ringer, Met Office Hadley Centre, Exeter, United Kingdom

RO SAG Co-Chairs:

- M. Kern, ESA/ESTEC, Noordwijk, The Netherlands
- A. von Engeln, EUMETSAT, Darmstadt, Germany

Other experts:

- M. J. Angling, University of Birmingham, UK
- R. Biondi, University of Padua, Italy
- E. Cardellach, ROM SAF / IEEC, Barcelona, Spain
- M. Garcia, Rokubun, Barcelona, Spain
- A. Garcia, ESA, ESTEC, Noordwijk, The Netherlands
- H. Gleisner, ROM SAF / DMI, Copenhagen, Denmark
- M. Hernandez-Pajares, UPC, Barcelona, Spain
- K.B. Lauritsen, ROM SAF / DMI, Copenhagen, Denmark
- B. Nava, The Abdus Salam International Centre for Theoretical Physics, Trieste, Italy
- J.K. Nielsen, ROM SAF / DMI, Copenhagen, Denmark
- R. Notarpietro, EUMETSAT, Darmstadt, Germany
- S. Remus, ESA, ESTEC, Noordwijk, The Netherlands
- A.K. Steiner, University of Graz, Austria
- S. Syndergaard, ROM SAF / DMI, Copenhagen, Denmark